Aerodynamics of Wing-Integrated Ram-Air Duct for Propeller Aircraft

A Numerical Investigation into Wing-Integrated Duct Performance and Wing-Body Junction Flow

H. Maho

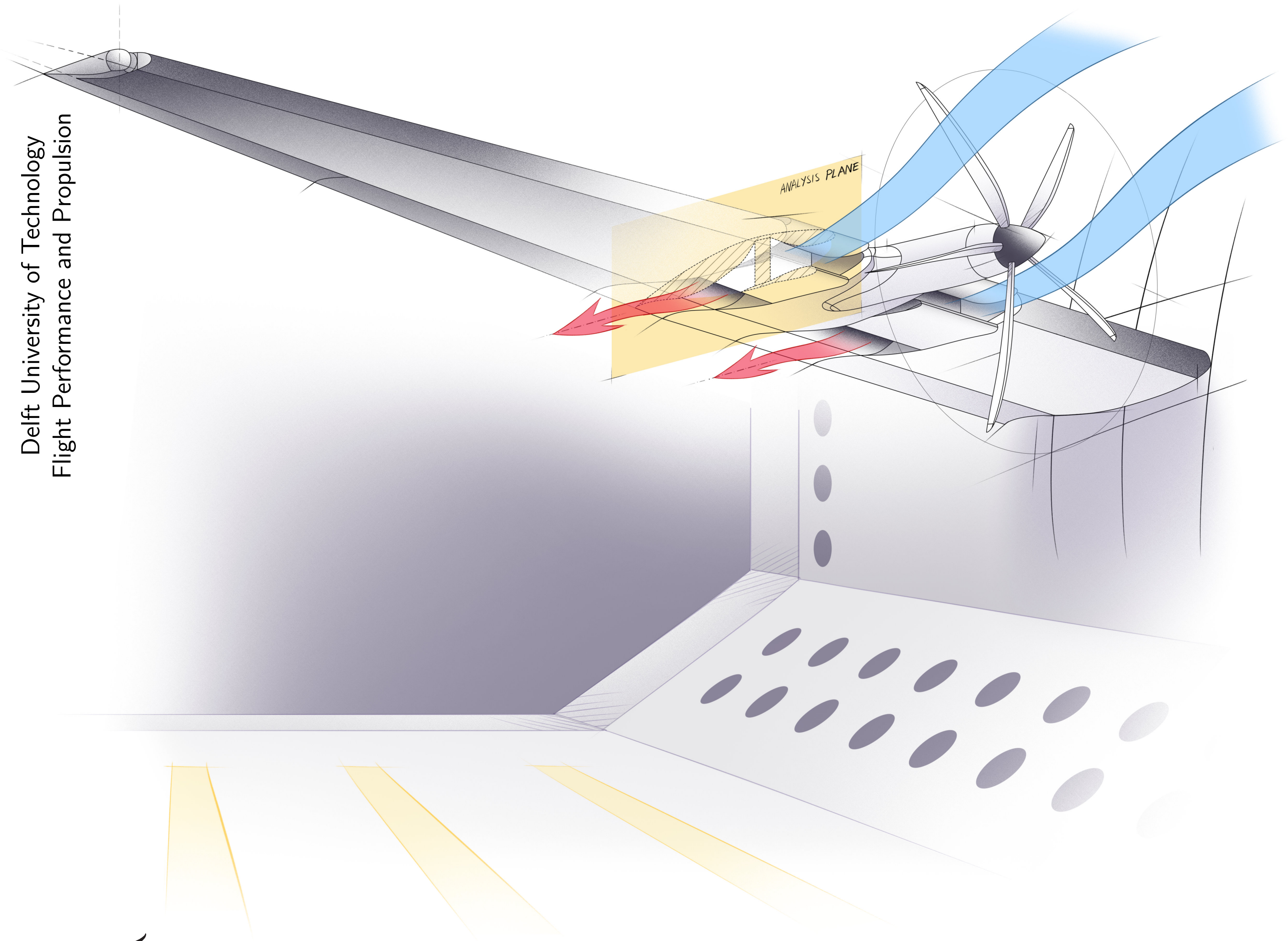

Delft University of Technology
Flight Performance and Propulsion

Delft University of Technology

Aerodynamics of Wing-Integrated Ram-Air Duct for Propeller Aircraft

A NUMERICAL INVESTIGATION INTO WING-INTEGRATED DUCT PERFORMANCE AND WING-BODY JUNCTION FLOW

by

H. Maho

for the purpose of obtaining the degree of

Master of Science in Aerospace Engineering

at Delft University of Technology,

to be defended publicly on Thursday March 27, 2025 at 13:30 o'clock.

Student number:	4983726	
Thesis committee:	Prof. dr. ir. L. L. M. Veldhuis,	TU Delft, Supervisor
	Dr. ir. W. J. Baars,	TU Delft, Chairman
	Dr. ir. A.H van Zuijlen,	TU Delft, Examiner
	Ir. F. Beltrame,	TU Delft, Examiner

ACKNOWLEDGEMENTS

This thesis marks the closing step of my studies at the Delft University of Technology. Over the past few years, this journey has been both challenging and rewarding, and I have dedicated everything I could to this research, pushing myself through challenges that required resilience and problem-solving. It has been a demanding yet deeply rewarding experience–one that has strengthened my abilities as both an engineer and a researcher. Of course, I owe my deepest gratitude to those without whom I could not have completed this thesis.

First and foremost, I would like to express my deepest gratitude to my thesis supervisor, Professor Leo, for his continuous support, guidance, and positive attitude throughout the past year. His expertise, enthusiasm, and critical remarks have been invaluable–every time I left his office, I felt more motivated and inspired. Without his help, this thesis would not be where it is today. The insights I have gained from him, both personally and academically, will stay with me throughout my career and beyond. A special thanks to Fabio for his expertise, enthusiasm, and willingness to offer guidance throughout this journey. The many meetings and discussions we had on the thermohydraulic aspect of this research were invaluable, and I truly appreciate his support, as well as his insightful contributions.

Beyond the academic world, I am deeply grateful to my parents for their unconditional support throughout this journey. Their constant encouragement, phone calls, and positive energy have been a source of strength, even during times when I was too busy to stay in touch as often as I should have. Their belief in me never wavered, and for that, I am truly thankful.

To my dearest wife Rewas, I am incredibly proud of you for recently being accepted as a specialist in plastic surgery–a remarkable achievement that reflects your dedication and hard work in becoming a surgeon. Over these past years, we have spent many days apart as I pursued my studies, and I am deeply grateful for the sacrifices we have made together. Thank you for your unconditional support, patience, and love, even when distance made things difficult. I cannot wait to see what the future holds for us and to embark on this next chapter together.

H. Maho
Delft, March 2025

Abstract

Steady Reynolds-Averaged Navier-Stokes (RANS) simulations utilizing the k-ω SST turbulence model are conducted to investigate the aerodynamic performance of a wing-integrated ram-air duct housing a heat exchanger for propeller-driven aircraft, including its impact on wing-body junction flow. The research is conducted in two stages: first, a 2D aerodynamic analysis employing a Design of Experiment (DoE) methodology to assess the sensitivity of key geometrical parameters–including stagger angle, leading-edge droop, duct gap, and heat exchanger characteristics–on lift, drag, and duct mass flow rate; and second, a 3D investigation of the junction flow behavior in the nacelle/ducted-wing configuration. The heat exchanger pressure drop is modeled as a porous media zone using the Darcy-Forchheimer quadratic drag law. Heat transfer is incorporated through a variable energy source term applied via a user-defined function (UDF) based on the ε-NTU correlation. Findings from the 2D aerodynamic analysis indicate that heat exchanger characteristics, particularly porosity and thickness, have a more pronounced impact on aerodynamic performance than external duct geometry. However, intake stagger angle and leading-edge droop play critical roles in mitigating flow separation and optimizing the wing pressure distribution. In addition, the redistribution of pressure due to flow restriction alters the stagnation point location, inlet-velocity ratio, and static pressure distributions, all of which influence the aerodynamic loading of the ducted wing. The optimal ducted airfoil configuration, featuring a lower-surface outlet aft of the maximum thickness and a thin heat exchanger, minimizes aerodynamic penalties while maximizing duct mass flow rate. However, thermal feasibility assessments reveal that meeting the cooling demands of fuel-cell systems necessitates a thicker heat exchanger to accommodate sufficient heat transfer area within the constrained wing volume. This increase in thickness impairs aerodynamic performance through increased pressure drop and resultant drag. Although higher porosity mitigates flow resistance, the required thickness offsets this advantage, reinforcing the inherent trade-off between aero-thermal performance. In 3D, the presence of the heat exchanger inside the duct fundamentally alters the local aerodynamics by modifying boundary layer interactions at the wing-body junction. The flow resistance imposed by the heat exchanger directly affects the strength and topology of secondary flow structures, particularly the horseshoe vortex (HSV), which governs junction flow behavior and whose strength scales with the Reynolds number based on the momentum thickness of the incoming boundary layer. At low porosity levels, the stronger HSV, with an increased vertical extent above the wing, entrains high-momentum freestream flow into the chordwise and spanwise boundary layers, mitigating corner flow separation. Conversely, at high porosity levels, lower flow resistance alters HSV topology, reducing its vertical extent and allowing part of the vortex to enter the duct, inducing a secondary vortex at the lower lip. This weakens the HSV's ability to stabilize the boundary layer, leading to earlier separation, increased pressure losses, and higher drag. A moderate porosity level provides an optimal balance between HSV strength, vertical positioning, and junction flow stability, reducing corner flow separation and associated pressure losses. Collectively, these findings yield critical insights into integrating ram-air cooling ducts within the wings of propeller-driven aircraft, offering a compelling approach to achieving efficient thermal management systems with minimal aerodynamic penalty. This investigation provides unprecedented detail in visualizing and understanding the intricate coupling between ducted wing aerodynamics and heat exchanger-induced flow interactions, while emphasizing the need for further research to validate and expand upon these findings.

CONTENTS

NOMENCLATURE

ABBREVIATIONS

2D	Two-dimensional
3D	Three-dimensional
AF	Airfoil
BC	Boundary condition
BF	Bluntness factor
BL	Boundary layer
CAD	Computer aided design
CFD	Computational fluid dynamics
DNS	Direct numerical simulation
DOE	Design of experiment
ERAST	Environmental research aircraft and sensor technology
EVM	Eddy viscosity model
FCS	Fuel cell system
GCI	Grid convergence index
HPC	High performance computing
HSV	Horseshoe vortex
HX	Heat exchanger
ID	Inner domain
LDR	Leading-edge droop ratio
LES	Large eddy simulation
LTPEM	Low temperature proton exchange membrane
MDF	Momentum deficit factor
MDO	Multidisciplinary design optimization
MS	Medium speed
NACA	National advisory committee for aeronautics
NS	Navier-Stokes
NTU	Number of transfer unit
NW	Nacelle-wing
OD	Outer domain
PM	Porous medium
RANS	Reynolds-averaged Navier-Stokes
RPA	Remotely piloted aircraft
RSM	Reynolds stress model
SA	Spalart-Allmaras
SST	Shear stress transport
TMS	Thermal management system
TREX	Tetrahedral extrusion
UAV	Unmanned aerial vehicle

UDF	User-defined function
URANS	Unsteady Reynolds-averaged Navier-Stokes
VC	Volume condition

SYMBOLS

A	Area, m
a	Speed of sound, $\mathrm{m\,s^{-1}}$
b	Span, m
C	Heat capacity rate, $\mathrm{W\,K^{-1}}$
C_d	$F_d/(q_\infty c)$ drag coefficient
C_D	$F_D/(q_\infty S)$ drag coefficient
C_f	τ_w/q_∞ skin friction coefficient
C_l	$F_l/(q_\infty c)$ lift coefficient
C_L	$F_L/(q_\infty S)$ lift coefficient
C_p	$(p-p_\infty)/q_\infty$ pressure coefficient
C_{p_t}	$(p_t-p_{t_\infty})/q_\infty$ total pressure coefficient
c	Chord, m
c_p	Specific heat capacity, $\mathrm{J\,kg^{-1}\,K^{-1}}$
d	Inlet entrance height, m
ΔM	Maximum difference between all available grid solutions
Δp	Change in static pressure, Pa
δ_{RE}	Difference between the selected grid solution and the estimated exact solution
F_d	Drag force, N
F_l	Lift force, N
g	Gravity, $\mathrm{m\,s^{-2}}$
h	Vertical displacement, m
h_i	Average cell size of grid i, m
i	Inlet entrance plane
k	Turbulent kinetic energy $\mathrm{m^2\,s^{-2}}$
M	Mach number
p	Static pressure, Pa; observed order of convergence
p_t	Total pressure, Pa
q	Dynamic pressure, Pa
ρ	Density, $\mathrm{kg\,m^{-3}}$
R	Specific gas constant, $\mathrm{J\,kg^{-1}\,K^{-1}}$
S	Surface arc length, m; Source term; Sutherland temperature, K
t	Thickness, m; time, s
T	Static temperature, K
T_t	Total temperature, K
τ_w	Wall shear stress, Pa
U	Heat transfer coefficient, $\mathrm{W\,m^{-2}\,K^{-1}}$
U_s	Standard deviation of the fit derived from the observed rate of convergence
U_ϕ	Estimated discretization uncertainty
u	x-velocity component, $\mathrm{m\,s^{-1}}$

u^+	Dimensionless velocity
u_τ	Friction velocity
v	y-velocity component, $\mathrm{m\,s^{-1}}$
V	Velocity, $\mathrm{m\,s^{-1}}$; Volume, $\mathrm{m^3}$
x	Axial coordinate, m
y	Lateral coordinate, m
y^+	Dimensionless wall distance
z	Vertical coordinate, m
α	Angle of attack, deg
β	Compactness, $\mathrm{m^2\,m^{-3}}$
γ	Specific heat ratio
μ	Dynamic viscosity, $\mathrm{kg\,m^{-3}}$
ν	Kinematic viscosity, $\mathrm{m^2\,s^{-1}}$
ω	Vorticity, $\mathrm{s^{-1}}$
Ω	Rotational speed of the propeller, $\mathrm{rad\,s^{-1}}$
ϕ_i	Numerical solution for grid i, Pa
ε	Effectiveness; porosity
φ	Stagger angle, deg; scalar quantity

SYMBOL SUBSCRIPTS

a	Axial
b	Heat exchanger inlet plane
c	Chord; Cold
e	Duct exit plane
h	Hot
i	Duct inlet plane
LE	Leading edge
max	Maximum
min	Minimum
o	Freestream
op	Operating
p	Propeller
s	Static
t	Tangential; Total
TE	Trailing edge
x	x-direction
y	y-direction
z	z-direction
∞	Freestream
θ	Momentum thickness

SYMBOL SUPERSCRIPTS

$*$	Theoretical order of convergence
$\overline{}$	Time-averaged component
$'$	Fluctuating component

Part I

Background

1

INTRODUCTION

The quest for sustainable aviation emerges as a critical challenge in the 21st century, with the aerospace industry actively seeking innovative approaches to reduce the environmental footprint of aviation globally. A key aspect of this endeavor involves ambitious emission reduction targets. These have been articulated by initiatives such as Destination 2050[1] from the European aviation sector, and complemented by global efforts like Waypoint 2050[2]. Together, they strive for near-complete decarbonization in aviation operations globally in 2050. Hydrogen-powered aircraft are showing promising potential as an alternative to traditional kerosene-powered aircraft, demonstrating minimal impact on the climate. The electrification of aircraft propulsion systems using hydrogen fuel-cells as the primary power source is emerging as a key strategy to significantly reduce the aviation industry's carbon footprint [1]. As the demand for regional, short-haul flights rises, the development of turboprop aircraft powered by fuel-cells is gaining traction as a highly efficient, environmentally friendly, and economically viable solution [2]. It is estimated that fuel-cell propulsion systems in aircraft have the potential to reduce the climate impact of aviation by approximately 75 to 90 percent [2]. Although fuel-cell propulsion aircraft are favorable for their lower environmental impact, they also present technological challenges, particularly regarding their thermal management system (TMS). These TMSs require advanced cooling techniques and highly efficient heat exchangers to meet the cooling demands of fuel-cell technology in aviation, such as the low-temperature proton exchange membrane (LTPEM) fuel-cell systems (FCS) [3]. LTPEM-FCS are considered the most suitable for the aviation industry due to their high power density when compared to other fuel cell technologies [4].

A recent development includes the introduction of powertrain conversion kits by Universal Hydrogen and ZeroAvia [5, 6], designed to retrofit existing regional aircraft such as the ATR 72 and De Havilland Canada Dash-8 for hydrogen fuel-cell technology, while minimizing structural changes. A key challenge associated with LTPEM-FCS, as highlighted by Sain *et al.* [3], is their weight and overall volume, with the latter driving the need for larger air intakes and heat exchangers to facilitate system cooling. As depicted in Figure 1.1, the starboard wing features large ram-air ducts integrated on both sides of the nacelle housing the turboprop engine. A ram-air intake system relies on the aircraft's forward motion, where the associated dynamic pressure forces the ambient air into the duct at a higher pressure. These powertrain conversion kits feature significantly larger air intakes than conventional turboprop engines [7], as evident

[1] See `https://www.destination2050.eu`

[2] See `https://aviationbenefits.org/downloads/waypoint-2050/`

in Universal Hydrogen's design. A more refined four-duct ram-air configuration surrounding the nacelle, as depicted in Figure 1.2, efficiently directs airflow to multiple components for cooling, further highlighting the significant cooling demands of fuel-cell technology.

Figure 1.1: Universal Hydrogen's De Havilland Canada Dash-8, retrofitted with hydrogen fuel-cell technology. The turboprop engine on the starboard wing integrates prominent ram-air cooling ducts housing heat exchangers on both sides of the nacelle to manage the thermal demands of the FCS. *Image credit: Universal Hydrogen.*

Figure 1.2: ZeroAvia's ATR-72, retrofitted with a hydrogen-electric powertrain. The nacelle features a four-duct ram-air configuration, each duct channeling airflow to different components to meet the cooling demands of the FCS. *Image credit: ZeroAvia and KLM Royal Dutch Airlines.*

However, while necessary for cooling, the drag associated with large ram-air ducts around the nacelle can have detrimental effects on aerodynamic performance. In particular, air intakes located in the vicinity of a propeller slipstream experience a highly non-uniform flow field with high dynamic pressures due to the added axial momentum. This flow field non-uniformity, caused by the angular momentum imparted into the flowfield–often referred to as a loss term in propeller efficiency–alters the local angle of attack and can potentially lead to localized flow separation. The increased drag is primarily attributed to form drag, caused by the large size and shape of the duct disrupting local airflow, leading to local pressure imbalances. Furthermore, the increased surface area of the duct introduces more skin friction, contributing to parasitic drag and further reducing the overall aerodynamic efficiency. The junction between the wing and the unconventional nacelle can lead to interference drag, as the airflow interaction between these components generates additional turbulence and pressure variations. Given these potential adverse effects on aircraft performance, developing an innovative wing-integrated ram-air-based TMS is essential to mitigating the added drag and interference introduced by the external ducts. One such concept is the shoulder-inlet design for TMS, originally conceptualized by Professor L.L.M. Veldhuis, which derives its name from the bilateral wing inlets resembling shoulders and the propeller hub representing the head, as shown in Figure 1.3. It is crucial to understand the key flow physics involved, as they encompass a range of phenomena, including juncture flow such as nacelle/ducted-wing interaction, propeller-inlet interaction, unsteady heat transfer, stall characteristics, and wake filling, among others. Achieving this integration within the wing presents unique challenges, particularly due to the restricted internal structural space and its impact on aerodynamic performance, the latter being the key focus of this research.

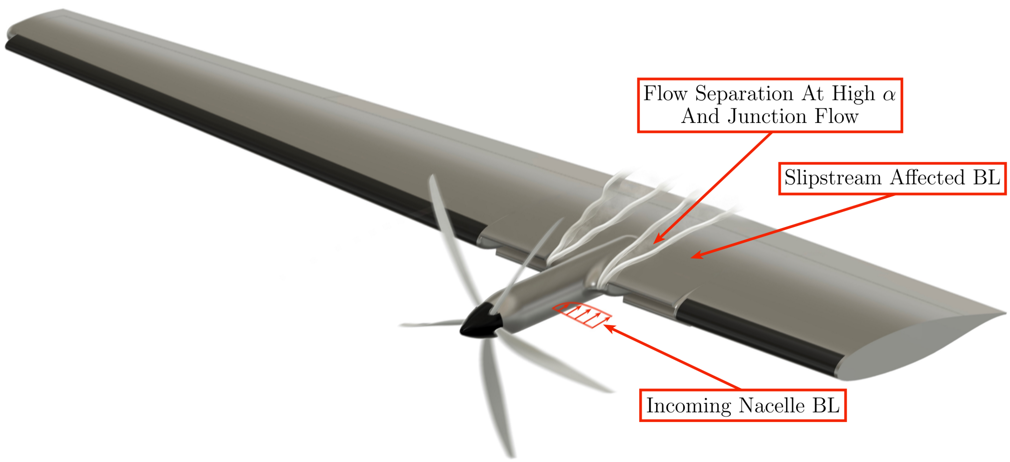

Figure 1.3: 3D representation of the shoulder-inlet design for TMS, illustrating the interaction between the nacelle boundary layer and the ducted wing, which leads to secondary flow structures in the junction region, with the incoming boundary layer being exaggerated for perspicuity.

1.1. HISTORICAL CONTEXT

The initial concept of wing-integrated ram-air ducts dates back to the Second World War, when the National Advisory Committee for Aeronautics (NACA) conducted extensive research to improve the cooling efficiency of military aircraft. As combat aircraft engines–both radial and in-line–became more powerful to meet wartime demands for high speed, maneuverability, and payload capacity, thermal management challenges emerged. These challenges were particularly pronounced during operations involving steep climbs and high power settings, which significantly increased the engine heat that needed to be dissipated quickly and efficiently. Conventional air cooling, by guiding the airflow through the engine cowling, was often insufficient, leading to the development of wing-integrated cooling installations. This streamlined solution efficiently guides airflow to engine components such as oil coolers and radiators, avoiding the need for external scoops that would otherwise increase drag. A notable example is the Grumman XF7F-1 Tigercat fighter aircraft, depicted in Figure 1.4. The investigation by Chapman [8] aimed to analyze the internal and external flow characteristics of the wing-integrated ducting system, both with and without the influence of the propeller slipstream. It became apparent that, without the presence of the propeller slipstream, premature flow separation would occur at the lower lips of the leading-edge intake at higher angles of attack, leading to pressure recovery losses within the duct. The pressure recovery within the duct is directly related to the efficiency of the cooling installation. However, when the ducts are submerged in the propeller slipstream, the rotational direction of the propeller blades is of critical importance. The intake in the vicinity of the down-going blade benefits from slipstream effects, reducing flow separation due to a lower local effective angle of attack. In contrast, the intake near the up-going blade requires geometry optimization to prevent premature separation and sustain pressure recovery at high angles of attack. It is evident that, during wartime, the use of wing-integrated ducts within a propeller slipstream could be beneficial, as optimizing the duct and inlet geometry and positioning not only controlled boundary layer separation but also minimized external aerodynamic drag [8], often referred to in the literature as cooling installation drag.

Figure 1.4: Grumman XF7F-1 Tigercat fighter aircraft, mounted in the Ames 40-by 80-foot wind tunnel to investigate wing-integrated duct performance under propeller slipstream effects [8]. *Image credit: NASA Ames Research Center.*

Figure 1.5: Convair B-36J-III "Peacemaker" military aircraft featuring multiple ram-air intakes located at the wing leading-edge for aerodynamic and cooling efficiency purposes.
Image credit: U.S. Air Force.

Figure 1.6: De Havilland Mosquito DH-98 military aircraft featuring two engine cooling ram-air ducts positioned in the inboard section of the wing.
Image credit: Royal Canadian Air Force.

The Convair B-36J-III "Peacemaker" military aircraft, shown in Figure 1.5, provides another example. The propulsion system features six radial engines in a pusher configuration, each driving a propeller. Each engine featured dual leading-edge intakes, designed to provide the substantial airflow required for cooling the large radial engines while also offering redundancy in case of intake obstruction. Moreover, it is likely that the smaller lower intake was intended to supply airflow to a smaller heat exchanger, supporting supplementary cooling needs. In a pusher configuration, the propeller-inlet interaction is minimized; therefore, the airflow entering the intakes remains less disturbed by the propeller wash. This leads to smoother and more stable intake flow, enhancing engine performance and cooling efficiency by mitigating pressure fluctuations and flow instabilities.

The De Havilland Mosquito DH-98 military aircraft, shown in Figure 1.6, features engine cooling ducts housing small radiators, with the outlet positioned ahead of the wing box to minimize structural modifications while effectively managing engine temperatures through ram-air cooling. The propulsion system operates in a puller configuration, where propeller-inlet interaction influences the duct flow, affecting pressure distribution and altering local aerodynamic characteristics, potentially altering cooling performance due to unsteady heat transfer. Additionally, the design lacks a leading-edge fillet between the fuselage and the ducted wing, which promote secondary flow structures such as horseshoe vortices and corner flow separation at the junction region. These effects may introduce local flow disturbances, increasing aerodynamic losses.

Furthermore, a peculiar example of inlet design is the triangular wing root-integrated duct concept investigated by Keith and Schiff [9], depicted in Figure 1.7. Although this inlet design was developed for transonic applications, its unique shape, seamlessly integrating the wing duct with the fuselage, remains noteworthy and highlights NASA's innovation during this era. The total-pressure recovery remained near unity across a range of flight conditions, while minimizing interference with the fuselage boundary layer [9]. While the main focus of this research is subsonic aerodynamics, transonic aircraft design principles may not directly apply to modern turboprop applications due to higher compressibility effects. Nevertheless, the conceptual aspects of this triangular inlet still provide valuable insights. This concept, if reimagined with the fuselage body serving as a turboprop nacelle, could potentially be adapted for turboprop applications. The peculiarities of this inlet design offer promising aerodynamic advantages, such as effective boundary layer control and reduced drag [9], inspiring novel configurations for wing-integrated ram-air systems designed to reduce aerodynamic penalties.

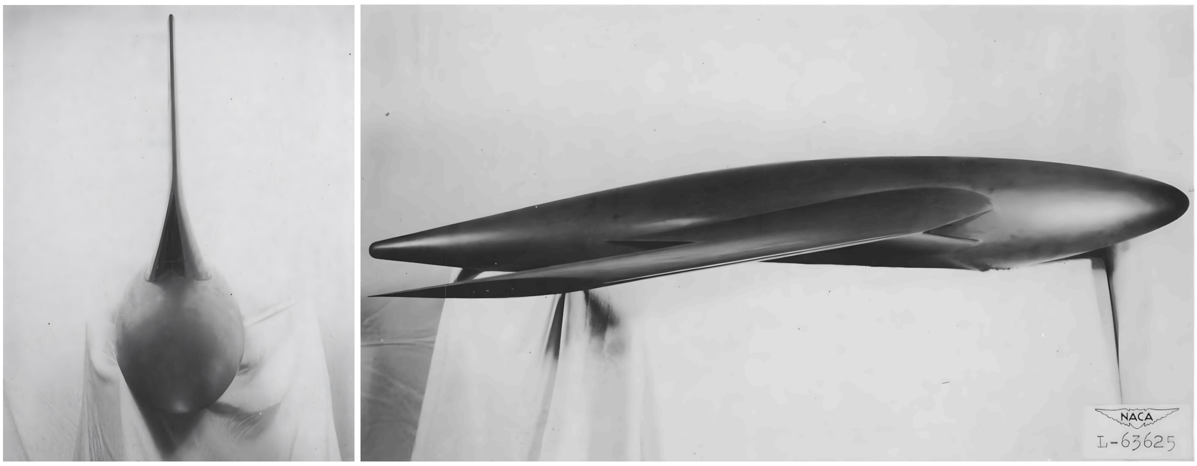

Figure 1.7: A triangular wing root-integrated duct concept for a highly swept wing designed for transonic aircraft [9]. *Image credit: NASA Langley Aeronautical Laboratory.*

By revisiting historical NASA innovations, such as the examples discussed earlier, researchers can adapt their principles to address cooling challenges in hydrogen-propulsion TMSs, offering insights into improving aerodynamic efficiency and integration in contemporary systems. The absence of these design principles in projects such as Universal Hydrogen and ZeroAvia reflects deliberate trade-offs [5, 6]. For instance, Universal Hydrogen's large ram-air cooling duct design prioritizes higher mass flow rates and heat dissipation requirements over streamlined integration, driven by the high operational cooling requirements of fuel-cell propulsion systems. In a recent study by Sain *et al.* [3], the cooling power requirement for LTPEM-FCs was reported to be approximately 560 kW. This explains the adoption of less aerodynamically optimized solutions. In contrast, ZeroAvia's TMS adopts a more refined approach with smaller individual ducts, which may reduce localized aerodynamic penalties. However, this configuration is expected to increase drag and diminish overall aerodynamic efficiency due to the unconventional nacelle shape and the lack of streamlined integration. These findings underscore need for further aerodynamic research to address the thermal management challenges of hydrogen-powered turboprop aircraft, which is the primary focus of this research.

1.2. RESEARCH OBJECTIVE

The research topic was motivated by the design challenge of efficient ram-air TMSs for hydrogen-powered turboprop aircraft, which require substantial heat dissipation while maintaining aerodynamic efficiency. This research delves into the aerodynamic analysis of wing-integrated ram-air ducts housing heat exchangers. One potential solution is the integration of heat exchangers within the wing rather than the nacelle, as in the shoulder-inlet design for TMSs, effectively reducing both form and interference drag [10]. Design solutions like those from Universal Hydrogen and ZeroAvia meet thermal requirements; however, their large external ram-air ducts protrude significantly from the airframe, increasing the aerodynamic wetted area and disrupting the streamlined shape, often resulting in drag penalties.

A critical review of the existing literature on wing-integrated ducts for fuel-cell-powered turboprop aircraft highlights a research gap. Many studies, particularly from NASA wartime research, focus on ducted airfoil aerodynamics, often considering the influence of propeller slipstream. However, detailed studies of flow physics within wing-integrated ducts, specifically for turboprop aircraft, are scarce. Most prior research has concentrated on cooling installations for high-altitude UAVs and RPAs operating under low Reynolds number conditions [11–14]. Although valuable, these studies primarily focus on external aerodynamics and do not address the challenges of TMSs for hydrogen-powered turboprop aircraft. Furthermore, there is limited use of high-fidelity RANS simulations to analyze the aerodynamic performance of wing-integrated ducts. Additionally, the interaction between internal flow blockage within the duct and external aerodynamics, and thus the synergy between internal and external aerodynamics, has not been previously investigated using RANS simulations. While the ultimate goal of this research is to develop a complete wing-integrated duct design, the primary focus is on understanding how various duct geometries and heat exchanger flow blockage affect key aerodynamic parameters, such as lift, drag, mass flow rate, and wing-body junction flow phenomena. Motivated by these considerations, the following research objective was established for this thesis:

> *The research objective is to get a fundamental understanding of the aerodynamic performance, specifically lift and drag, of a wing-integrated duct housing heat exchangers, as well as the wing-body junction flow phenomena, through high-fidelity RANS simulations.*

To assess the aerodynamic viability of a wing-integrated duct design for modern turboprop aircraft, several key questions must be addressed. First, the aerodynamic effects of key geometric parameters remain not well understood, leading to the following question:

1. What are the 2D aerodynamic implications of key geometric parameters in a wing-integrated duct under climb and cruise angles of attack?

(a) What are the effects of intake lip radii?
(b) What are the effects of intake lip staggering?
(c) What are the effects of changing the intake gap?
(d) What are the effects of varying the duct outlet position?
(e) What are the effects of vertical displacement (droop) of the intake?

Secondly, existing literature lacks studies on how flow restriction within the duct–caused by a heat exchanger modeled as a porous medium in CFD–affects aerodynamic performance. This gap leads to the following research question:

2. How does a wing-integrated duct with restricted flow due to the heat exchanger compare to a clean wing in terms of 2D aerodynamic performance under climb and cruise angles of attack?

(a) What are the effects of the chordwise position, thickness, and porosity of the heat exchanger?
(b) How does the heat exchanger flow resistance affect the stagnation point location at the intake?
(c) What impact does flow restriction have on lift and drag coefficients?

Lastly, the lack of existing studies on complex secondary flow structures between the nacelle and the wing-integrated duct raises the following question:

3. How does the aerodynamic interaction between the wing-integrated duct and a flat plate affect the 3D wing-body junction flow phenomena under climb and cruise angles of attack?

(a) How does flow restriction within the duct affect the strength of the horseshoe vortex compared to a clean wing?
(b) How does flow restriction within the duct affect the lift and drag coefficients of the wing-body model?

1.3. RESEARCH OUTLINE

This thesis is structured into seven chapters. After this introduction, Chapter 2 analyzes the aerodynamic principles underlying the design of wing-duct systems, focusing on the aerodynamic function of each component within the ram-air cooling duct. The complex flow phenomena at the wing-body junction and their contribution to interference drag are also discussed.

In Chapter 3, the numerical methodology is outlined, detailing the aerodynamic and thermal analysis approach, including the governing equations for RANS simulations, turbulence modeling, computational domains, and boundary conditions. The computational setup is validated to assess its accuracy in predicting aerodynamic performance, focusing on a baseline airfoil case. Additionally, a thermal and pressure drop analysis of the heat exchanger is conducted to evaluate its influence on duct performance and overall aerodynamic behavior.

Chapter 4 presents results on the two-dimensional aerodynamic performance of the wing-integrated duct, providing insights into the effects of key geometric variations and heat exchanger-induced flow resistance compared to a clean wing, as discussed in Section 4.1 and Section 4.2. Additional simulations in Section 4.3 analyze the most aerodynamically favorable configuration, assessing the impact of heat dissipation on aerodynamic performance and the feasibility of integrating the heat exchanger within the available wing volume. The influence of the propeller slipstream on duct mass flow rate and its interaction with the ducted airfoil is briefly discussed in Section 4.4. Finally, the first and second research questions are addressed in Section 4.5.

The three-dimensional aerodynamic performance of the nacelle/wing-integrated duct configuration is presented in Chapter 5, focusing on junction flow phenomena and their interaction with heat exchanger-induced flow resistance. In Section 5.1, the aerodynamic performance of the nacelle/wing-integrated duct is compared to both the clean wing and the 2D results, providing insight into three-dimensional flow effects. Subsequently, the impact of heat exchanger porosity on secondary flow structures in the junction region is qualitatively analyzed in Sections 5.2 and 5.3. Finally, the third research question is addressed in Section 5.4.

The final chapters, Chapter 6 and Chapter 7, revisit the research questions, summarize the main findings, and provide recommendations for future research.

2

FUNDAMENTALS OF WING-DUCT AERODYNAMICS

This chapter provides an overview of the aerodynamic principles behind the design of wing-duct systems, which is essential for developing a ram-air thermal management system (TMS) with low-drag profiles and enhanced aero-thermal performance. The components of ram-air cooling ducts in TMSs and their respective aerodynamic functions are discussed in Section 2.1, followed by key design considerations for the basic geometry of ducted heat exchangers in Section 2.2, with a focus on their aerodynamic properties and cooling flow management. Finally, the complex flow phenomena at wing-body junctions are discussed, highlighting how the interaction and mixing of boundary layers cause secondary vortical structures, such as horseshoe vortices (HSVs), which contribute to interference drag, as detailed in Section 2.3.

2.1. COMPONENTS OF RAM-AIR COOLING DUCTS IN TMS

This section describes the components of the ram-air cooling duct within the TMS of an aircraft wing-integrated LTPEM-FCS. As shown in Figure 2.1, the air intake captures and guides the ram air into the duct system. Immediately following the intake is the diffuser, which decelerates the fast-moving air and convert some of its dynamic pressure into static pressure, a process known as pressure recovery. This deceleration happens just before the air enters the heat exchanger. Pressure recovery is critical because increased static pressure can improve the efficiency of the heat exchanger by promoting more interaction between the air and the heat transfer surfaces. Furthermore, the diffuser must be carefully designed to minimize boundary layer growth to prevent flow separation (i.e., stall), as this reduces pressure recovery, thereby decreasing heat exchanger efficiency. Often, due to limited internal space and the need to increase heat transfer area, the heat exchanger is positioned at an angle, which results in airflow entering and exiting at oblique angles relative to the core matrix of the heat exchanger [3, 15]. A larger heat transfer area is necessary to meet cooling requirements while maintaining efficient thermal performance. The detailed design of the heat exchanger core, including the arrangement of fins, plates, and other internal structures, falls outside the scope of this research.

Furthermore, the nozzle serves two primary functions, as described by Miley [15]: first, to accelerate and expel the heated air to the local freestream pressure, thereby reducing drag. Second, the nozzle regulates the mass flow rate through the ducted wing via an adjustable exit flap, adapting to different phases of flight. During take-off, as the aircraft transitions from near stationary to acceleration, cooling demand increases significantly. In some cases, as described by van Heerden *et al.* [16], an additional compressor is installed to increase the air mass flow rate to satisfy these cooling demands. According to Coutinho *et al.* [1], the ram-air cooling system performs sub-optimally during ground operations, take-off, go-around, and other instances of high power combined with low airspeed operation. In contrast, during cruise conditions, the cooler ambient air lowers the required mass flow rate for adequate cooling. To accommodate varying cooling requirements across different flight phases, the nozzle features a variable exit area, typically controlled by means of using a hinged flap [17]. Furthermore, the fuel-cell stack and auxiliary components of the TMS as shown in Figure 2.1, are integrated into the propeller nacelle. The subsequent section explores the aerodynamic principles underlying the basic geometry of the complete wing-duct system.

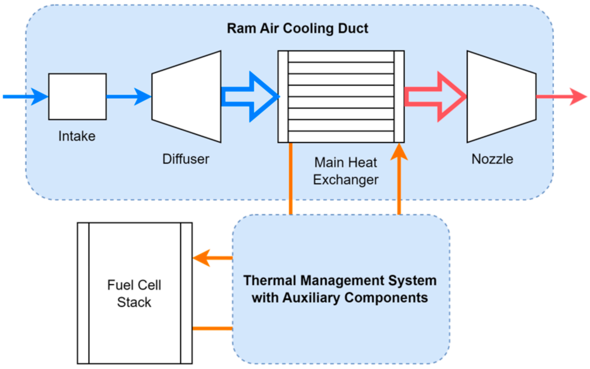

Figure 2.1: Schematic of a ram-air based TMS in fuel-cell powered aircraft. This diagram illustrates the airflow through the intake, diffuser, main heat exchanger, and nozzle, as well as the integration with the fuel-cell stack and auxiliary components of the TMS [7].

2.2. GEOMETRY OF COOLING INSTALLATIONS

The initial step involves understanding the design choices that shape the basic geometry of a simple ducted heat exchanger system, often referred to in the literature as a cooling installation. As shown in Figure 2.2, the geometry of the cooling installation includes a fairing encasing the heat exchanger core, which serves the dual purpose of streamlining the aerodynamic profile against the external airflow and indirectly regulating the incoming cooling mass flow rate by optimizing pressure recovery and guiding the airflow [11, 12, 18]. The components forming the ram-air management unit, including the inlet, diffuser, heat exchanger, and nozzle, each pose unique design challenges that must be addressed to ensure efficient operation [15].

Integrating intakes for the cooling installation into the leading-edge of the wing inherently leads to increased drag. Adler *et al.* [19] discovered that the direct cooling installation contributed around 2-3% to the total drag at cruise conditions, even with the benefit of the Meredith effect, which partially offsets the cooling drag by generating forward thrust. According to Harris and Recant [10], energy losses in such systems include external drag due to modifications to the basic airfoil shape at the duct inlet and outlet, internal losses from duct wall friction, losses from the duct diffuser expansion rate, and heat exchanger core resistance, in addition to the weight-related losses of the system as a whole. The design of the cooling installation should aim for properties such as low drag, minimal impact on wing's stall characteristics, consistent high-pressure air availability at the heat exchanger entrance, low internal energy losses, and stable performance across various flight conditions, as highlighted by Biermann and McLellan [20].

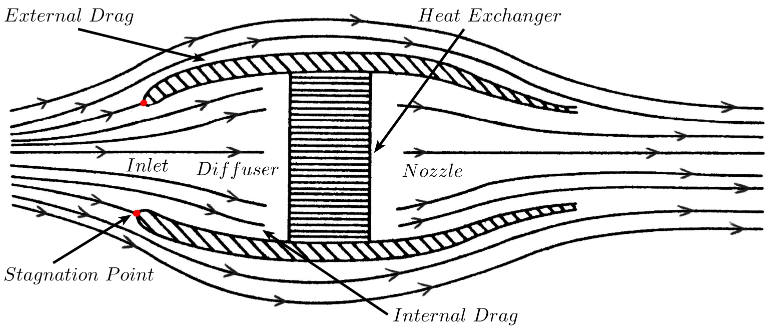

Figure 2.2: Simple ducted heat exchanger system (adapted from [15]).

At higher altitudes, the cooling installation requires a higher volumetric flow rate to sustain the same mass flow rate through the heat exchanger due to the reduced air density [17, 21]. It is therefore crucial to design a ducted wing that can adapt to this variation, to ensure adequate cooling performance across different flight conditions. In particular, a ducted wing designed for low-altitude performance loses efficiency at higher altitudes, where increased pressure losses result in an effective altitude loss of over 3,000 feet, as described by Katzoff [21]. This means the system behaves as if the aircraft were flying 3,000 feet lower in terms of available cooling performance. The degradation is primarily caused by two factors. First, as altitude increases, the required volumetric flow rate leads to higher velocities, increasing the risk of inlet flow separation, particularly if the duct geometry is not optimized for pressure recovery. This separation leads to additional pressure losses, further reducing cooling efficiency. Second, while pressure losses scale with dynamic pressure and decrease with air density [21], the higher flow velocities required at altitude result in increased frictional and viscous losses throughout the duct system, further contributing to total pressure losses. Additionally, the available pressure differential driving airflow through the duct is lower at altitude, making it more difficult to sustain the required cooling mass flow rate. To mitigate these challenges, ducted wing designs must minimize inlet separation and control internal velocities through a streamlined intake, an optimized diffuser, and a properly designed nozzle to reduce pressure losses. However, increasing duct size to counteract these losses is constrained by the limited internal volume within the wing, presenting a key design tradeoff.

The following sections explore the main design considerations of the components forming the ram-air management unit, focusing on their aerodynamic characteristics and cooling flow management.

2.2.1. INLET AND DIFFUSER

The design of the inlet must satisfy the cooling requirements of the heat exchanger without compromising the aerodynamic performance of the ducted airfoil [12]. The aerodynamic behavior of the ducted airfoil, which essentially serves as a fairing housing heat exchangers, resembles that of a clean airfoil in terms of stagnation point distribution when subjected to a uniform flow field. At a high positive angle of attack, the location of the stagnation point moves toward the lower surface near the leading-edge, as depicted in Figure 2.3a. The stagnation point on an airfoil is characterized by zero velocity and maximum stagnation pressure, occurring just before the airflow begins to move over the airfoil. The airfoil experience super-velocities on the upper surface causing a sharp suction peak at the leading-edge followed by a steep adverse pressure gradient, potentially leading to flow separation. The same principle holds for a high negative angle of attack, where the stagnation point shifts towards the upper surface, as depicted in Figure 2.3b. In this case, the airfoil experience super-velocities on the lower surface, which may cause flow separation [15].

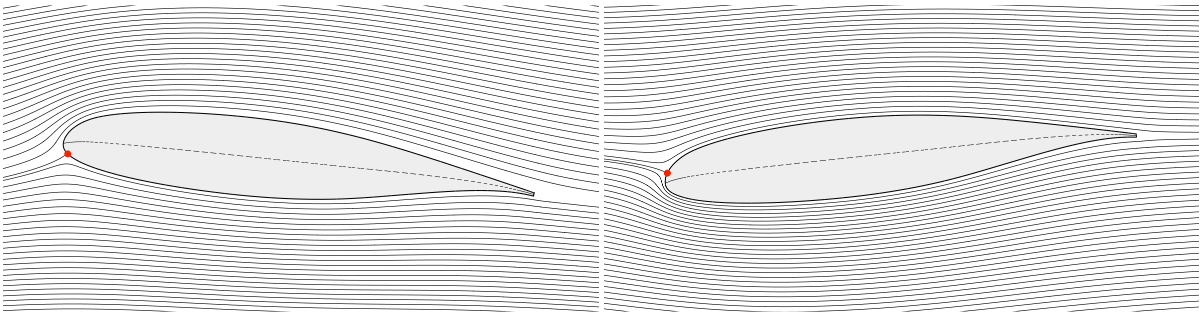

(a) Positive angle of attack

(b) Negative angle of attack

Figure 2.3: Shift in the stagnation point location due to changes in the angle of attack of the airfoil.

The same phenomenon occurs along the lip contours of the inlet of the fairing housing heat exchangers, where the stagnation point location dictates whether the flow remains attached or separates, as observed for a general case in Figure 2.4. The stagnation point location depends on the inlet-velocity ratio, which is defined as the velocity at the duct inlet relative to the freestream velocity. This ratio quantifies the degree to which the incoming air decelerates or accelerates relative to the external airflow. At low velocity ratios, as shown in Figure 2.4a, the stagnation point shifts inward at the inlet. This shift leads to a high suction peak on the external contour, resulting in super-velocities and possible flow separation, a consequence of a steep adverse pressure gradient. This is analogous to the previously discussed scenario for clean airfoils. Conversely, at high velocity ratios, as shown in Figure 2.4b, the stagnation point shifts outward at the inlet, causing flow separation on the inner surface [15]. According to Dannenberg [22], an increase in inlet-velocity ratio results in a proportional increase in velocity over the inlet's outer surface. This relationship holds independently of the angle of attack throughout the linear portion of the lift curve slope [22]. However, aft the point of maximum airfoil thickness, changes in the inlet-velocity ratio no longer influence the pressure distribution.

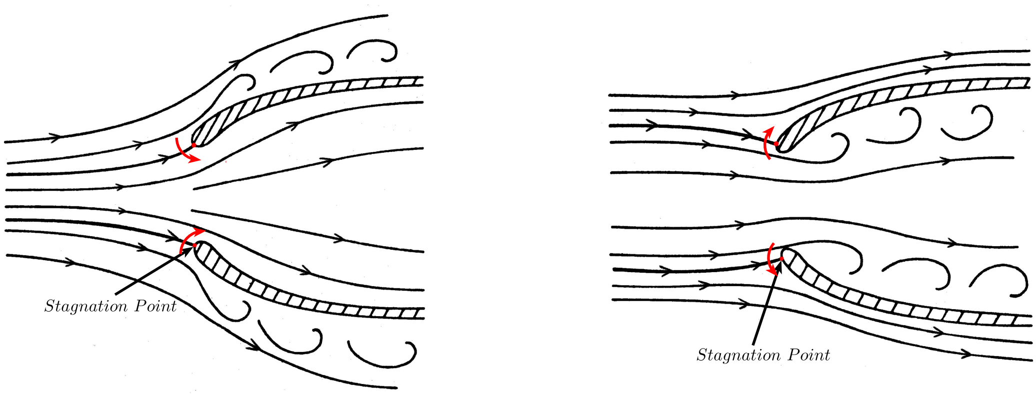

(a) Low velocity ratio

(b) High velocity ratio

Figure 2.4: Effect of velocity ratio on stagnation point location. The red arrows indicate its shift with changing velocity ratio, influencing inlet flow behavior [15].

As highlighted by Martin *et al.* [23], issues related to drag and cooling efficiency are often linked to the inlet design in cooling installations. Therefore, as indicated by Miley [15], airfoils with a thicker profile offer a greater range of operation for the stagnation point, in contrast to thinner airfoils. However, a thicker profile increases the frontal area, resulting in higher drag. The positioning of the duct-inlet is a crucial design aspect, as it plays an important role in attaining maximum efficiency [10]. The ducted airfoil is derived from a reference airfoil, which defines its outer contour and aerodynamic footprint. When incorporating the duct and heat exchangers, this outer contour functions as a fairing, maintaining the aerodynamic characteristics of the original clean airfoil. Harris and Recant [10] states that placing the duct inlet at the stagnation point of this reference airfoil ensures efficient funneling of airflow into the duct with minimal losses. The high-pressure differential at this point is most effective for pushing air through the duct system for a given inlet size, since the airflow enters the duct at a perpendicular angle, enhancing cooling efficiency. An angled air entry may cause turbulence and flow separation inside the duct. Effective use of duct-inlet opening sections can lead to cooling installations having practically no additional external drag in the range of lift coefficients for high-speed and cruising flight [24]. It should also be noted that airflow upstream of the duct-inlet is minimally affected by the downstream duct design [18].

Furthermore, in the research conducted by Martin *et al.* [23], the focus was on developing an inlet-airfoil design method for the heat exchangers of high-altitude remotely piloted aircraft (RPA), in collaboration with NASA and Environmental Research Aircraft and Sensor Technology (ERAST). The study introduces velocity ratios between various stations, as illustrated in Figure 2.5. Station (o) represents the free-stream velocity, station (i) corresponds to the inlet plane velocity at the narrowest point around the leading-edge [18], station (b) is the heat exchanger inlet velocity, and station (e) is the duct exit plane velocity. The velocity ratio between station (o) and station (b) is the product of external and internal diffusion [23], as represented in Equation 2.1.

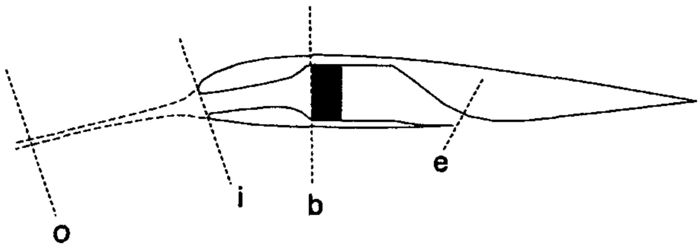

Figure 2.5: Control volume annotation of ducted heat exchanger system [23].

$$\frac{V_b}{V_o} = \left(\frac{V_i}{V_o}\right)\left(\frac{V_b}{V_i}\right) \tag{2.1}$$

External diffusion, represented by V_i/V_o, describes airflow deceleration from the free-stream velocity at station (o) to the inlet plane velocity at station (i). In contrast, internal diffusion, represented by V_b/V_i, refers to the velocity decrease from the inlet plane at station (i) to the heat exchanger core at station (b).

According to Martin [12] and Elsaadawy and Britcher [11], the shape of the duct inlet lips is determined by both internal and external diffusion factors. Internal diffusion is primarily a result of changes in the area of the internal duct, while the degree of external diffusion is linked to factors such as the inlet opening area, the critical Mach number, and the frontal area of the cooling installation [12]. A formula for external diffusion, derived under the assumptions of constant pressure surfaces and incompressible flow, is presented in Equation 2.2.

The inequality in the external diffusion equation indicates that a minimum threshold must be met to ensure the airflow decelerates sufficiently, allowing for pressure recovery and preventing flow separation at the inlet. Flow separation can occur both on the external surface of the fairing and along the inner surface of the inlet lips, and preventing this is essential for maintaining smooth airflow into the heat exchanger. Proper diffusion helps maintain overall aerodynamic efficiency and contributes to effective cooling performance. This formula is derived from theoretical concepts detailed in Küchemann and Weber [18], and is applicable to intakes of all shapes, including circular and three-dimensional intakes. Additionally, a corresponding formula applicable to compressible flows can be found in the same reference.

$$\frac{V_i}{V_o} \geq 1 - \sqrt{\left(\frac{A_{\text{max}}}{A_i} - 1\right)\left[\left(\frac{V_{\text{max}}}{V_o}\right)^2 - 1\right]} \tag{2.2}$$

In this equation, V_{max} denotes the maximum velocity on the outer surface of the fairing, A_{max} represents the maximum frontal area of the cooling installation, and A_i denotes the duct inlet area. The design of the outer surface of the fairing determines the ratio V_{max}/V_o and the critical Mach number [12]. When maintaining a constant ratio of V_{max}/V_o for a fixed design, an appropriate area ratio A_{max}/A_i must be selected to achieve optimal external diffusion [12]. This implies that the area ratio is directly proportional to the external diffusion, which is subsequently defined as the minimum velocity ratio, as indicated in Equation 2.3. Maximizing the area ratio is preferred for accommodating the cooling installation, as a larger frontal area can meet the required cooling demands for FCs.

$$\left(\frac{V_i}{V_o}\right)_{\text{min}} \propto \left(\frac{A_{\text{max}}}{A_i}\right)_{\text{max}} \tag{2.3}$$

Maximizing external diffusion, thereby lowering the velocity ratio, enables pressure recovery to occur in the stream ahead of the duct inlet rather than along its inner surface. This reduces the required distance for flow deceleration inside the duct, resulting in lower losses compared to cases where pressure recovery occurs entirely in contact with the surface [23, 25]. The losses associated with the pressure recovery occurring in contact with the inner surface are due to flow separation. According to Küchemann and Weber [18], the velocity is typically decreased significantly before it flows through the heat exchanger, as a measure to minimize drag.

Martin *et al.* [23] state that in low Reynolds number scenarios, the amount of internal diffusion is constrained by adverse pressure gradients on the duct walls causing flow separation. This could result in a stalled region ahead of the heat exchanger core, reducing its cooling efficiency. This aspect is crucial because, while the external flow may reach the transonic regime during cruise conditions, the internal flow is essentially incompressible and primarily governed by low Reynolds number effects [11, 12]. Furthermore, Miley [15] suggests that a practical range for velocity ratios is within $0.3 < V_i/V_o < 0.7$. For values beyond this range, particular focus should be given to the design of the inlet lip contour. Additionally, the same author suggests that the inlet area should constitute approximately 20 to 30% of the cooling installation's frontal area. Duct-inlet designs must consider variations in relative flow velocities due to changes in flight conditions and altitude [21]. The study conducted by Katzoff

[21] concludes that maintaining a low inlet-velocity ratio in ducts is preferable for minimizing pressure losses. However, these lower velocities must also comply with other design requirements. Furthermore, at high speeds and altitudes, a higher inlet-velocity ratio may be required to mitigate compressibility effects along the outer fairing contour.

During wartime cooling installations, short streamlined diffusers were commonly used to prevent internal flow separation and maintain efficient cooling performance by mitigating adverse pressure gradients, thereby reducing boundary layer separation [12]. As noted in Section 2.1, the purpose of the diffuser is to recover much of the full dynamic pressure into static pressure just before the air enters the heat exchanger. This pressure recovery can be optimized by lowering the inlet-velocity ratio, allowing it to take place upstream, leading to more efficient designs such as shorter diffusers. However, the diffuser's expansion rate must still be compatible with the boundary layer thickness to avoid flow separation [21]. An illustration of this can be seen in Figure 2.6, demonstrating flow separation in a conventional diffuser, which results in lower heat exchanger efficiencies. Additionally, the author highlights that the separation of the retarded boundary layer along the duct walls, causing a momentum deficit relative to the main flow, can be mitigated through streamlined duct designs and suitable inlet-velocity ratios. The effectiveness of the diffusers is generally indicated by lower pressure losses [20].

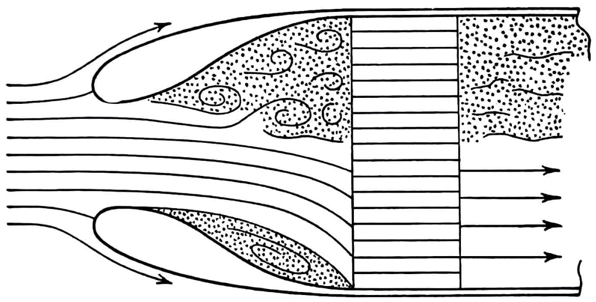

Figure 2.6: flow pattern in conventional diffuser showing flow separation on the inner upper lip [18].

AIRFOIL STAGGER

In this section, the aerodynamic benefits of staggering the entry lips of the fairing enclosing the heat exchanger are discussed. Airfoil stagger refers to the relative chordwise positioning of airfoils and is quantified by the stagger angle ϕ, which measures the horizontal displacement of the lower airfoil relative to the upper airfoil, as shown in Figure 2.7. Proper airfoil staggering can contribute to optimizing the aerodynamic efficiency of the ducted wing. For instance, positive staggering modifies flow distribution, potentially improving the lift-to-drag ratio by minimizing interference effects and improving flow alignment with the duct entry.

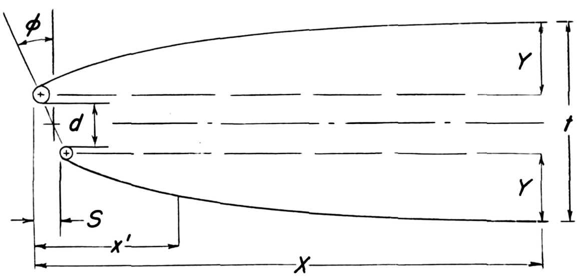

Figure 2.7: Geometrical parameters of a staggered inlet-profile based on a symmetric airfoil [22].

As explained by Küchemann and Weber [18], staggering the entry lips, with one behind the other, reduces the suction on the forward lip, thereby lowering its velocity, while conversely increasing suction on the rearward lip. Figure 2.8 illustrates the effect of staggered entry lips on the pressure distribution of a two-dimensional intake, particularly at a zero angle of attack. As discussed previously, variations in the angle of attack cause a shift in the stagnation point location, which in turn alters the inlet lip pressure distribution. In a staggered configuration, a higher angle of attack causes the stagnation point to move inward on the upper lip and outward on the lower lips, increasing the pressure peaks and the likelihood of flow separation [15], particularly over the upper surface. Therefore, meticulous design considerations are important when staggering entry lips, as any suboptimal design may have detrimental effects on the aerodynamic performance of the wing.

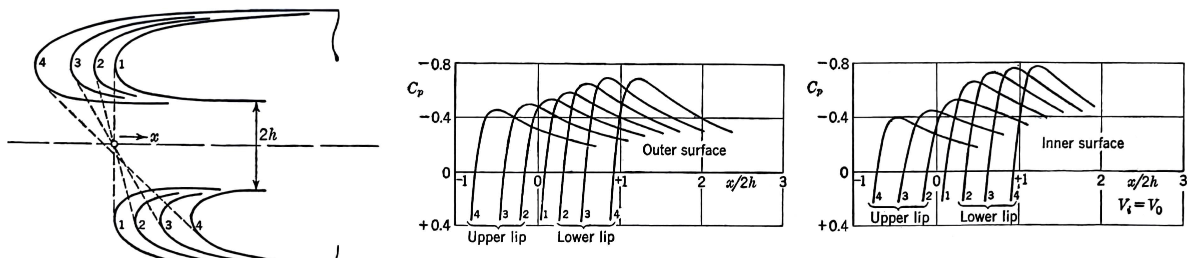

Figure 2.8: The pressure distribution over a staggered two-dimensional intakes [18].

Based on the findings of Dannenberg [22], observations showed that increasing the intake height or reducing the leading-edge radius of the upper lip adversely impacted the maximum lift coefficient. This reduction is attributed to the high-pressure peak at the upper lip, followed by a steep adverse pressure gradient, resulting in flow separation over the upper outer surface. Furthermore, a higher maximum lift coefficient can be achieved by increasing the inlet-velocity ratio until it matches the value of the plain wing [22], thereby minimizing external diffusion. However, this could lead to internal losses, even at smaller angles of attack, thus lower lift coefficients as indicated by Racisz [26].

As discussed earlier, maximizing external diffusion is preferred as it has the benefit of allowing pressure recovery to take place in the stream ahead of the inlet rather than along the inner surface. Hence, it is essential to find an optimal balance between staggering the entry lips and the design of the diffuser to improve the pressure recovery. As highlighted by Racisz [26], to offset the expected increase in internal losses at both high and low lift coefficients, it is necessary to increase the internal thickness of the upper and lower lips, forming a gradually expanding diffuser. This design ensures that the flow is effectively channeled by the thicker upper lip at high lift coefficients, while at low lift coefficients, the flow is similarly controlled by the thicker lower lip, leading to a reduction in internal losses [26], due to improved pressure recovery. To further improve the maximum lift coefficient and pressure recovery, leading-edge droop is essential to maintain a constant gap (d/t) ratio [22], as illustrated in Figure 2.7. This modification effectively guides airflow into the inlet at high angles of attack [26]. The impact of leading-edge droop on the maximum lift coefficient as a function of inlet-velocity ratio is evident in Figure 2.9, which shows improvements compared to a non-staggered, non-drooped configuration.

Furthermore, the research conducted by Biermann and McLellan [20] focused on determining the ideal location of the duct intake in a staggered configuration. The results showed that positioning the intake lips near the vertical plane of the leading-edge was the most effective, with negligible impact on the wing's overall performance. Additionally, it was observed that relocating the intake lips rearward from the vertical plane of the leading-edge had an adverse effect on the wing characteristics in terms of drag, lift, and stall [20]. Thus, the optimal positioning for the intake lips was found to be in close proximity to the leading-edge to achieve optimal pressure distribution and minimize drag. Bierman and Corson [27] observed that positioning the intake lips beyond the forward contour of the wing led to improvements, allowing full dynamic pressure recovery over most of the useful flight range.

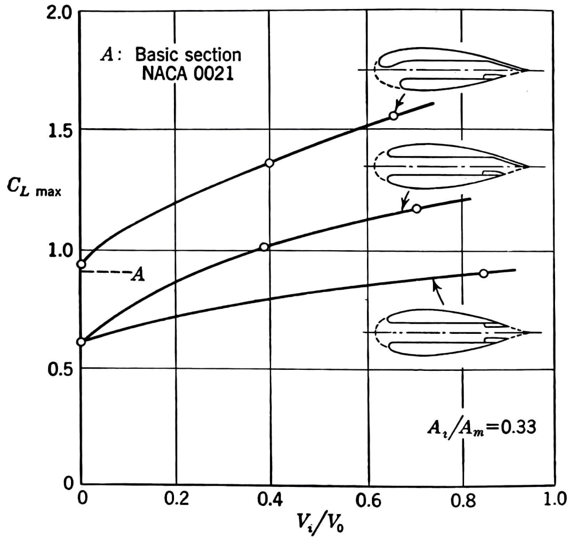

Figure 2.9: Maximum lift coefficients of three wings with leading-edge intakes and ducts for a constant area ratio, computed at a Reynolds number of 1×10^6 [18].

2.2.2. HEAT EXCHANGER

Ducted heat exchangers act as an orifice, inducing a pressure drop that correlates with the velocity of the airflow passing through the core matrix. The pressure drop can be attributed to various factors, one being the flow restriction caused by the matrix core, which includes components such as tubes, fins, or plates intended for heat transfer between two fluids. These components physically restrict the flow passing through the heat exchanger. As the flow passes through these components, its velocity increases, resulting in a proportional pressure drop. While heat transfer itself does not directly induce a pressure drop, variations in air density due to temperature changes may influence pressure characteristics, making the pressure drop dependent on air density and altitude [15]. The characteristics of the pressure drop can typically be expressed by Equation 2.4, as described by Miley [15], Küchemann and Weber [18].

$$w = a(\sigma_{\mathrm{HX}}\Delta p)^b \tag{2.4}$$

In this context, w refers to the mass flow rate of the cooling air, while σ_{HX} represents the density ratio of the heated air at the heat exchanger. The term Δp denotes the static pressure drop across the heat exchanger, and the constants a and b are specific to the matrix core design

[15]. These factors determine how the pressure drop depends on the cooling air's mass flow rate, influenced by the heat exchanger's design and air properties.

A more comprehensive modeling approach for the heat exchanger's pressure drop involves using the Darcy-Forchheimer equation as a volumetric momentum source term within the Navier-Stokes equations, accounting for both viscous (linear) and inertial (non-linear) resistance effects, rather than relying only on a single empirical correlation. A detailed explanation of how this momentum source term is integrated into the governing equations is provided in Section 3.8.2, focusing on how the Darcy-Forchheimer quadratic drag law equation models the pressure drop characteristics of the heat exchanger in CFD.

Choosing the appropriate heat exchanger type is a critical step in the design of cooling installations. For this study, a liquid-to-air heat exchanger is used. A trade-off must be made between two key factors to meet the cooling requirements: the entry area of the heat exchanger and the pressure drop characteristics across the heat exchanger [15]. Increasing the entry area reduces the pressure drop and internal drag by allowing the airflow to be distributed over a larger surface, thereby reducing the velocity through the core. However, this also results in a larger internal volume, which is often challenging to accommodate within a wing configuration. To mitigate this constraint, the heat exchanger is typically angled to increase the frontal area while reducing the pressure drop. However, this approach may lead to an increase in external drag due to the increased frontal exposure of the heat exchanger. Conversely, decreasing the entry area increases velocity through the core, resulting in a higher pressure drop and increased internal drag, but it reduces external drag by minimizing the frontal exposure of the heat exchanger. As highlighted by Miley [15], high-speed aircraft require a smaller inlet area to accommodate the required mass flow, whereas low-speed aircraft require a larger inlet area for the same purpose. The author also notes that reducing the frontal area of the heat exchanger is often necessary due to internal volume constraints, particularly in a wing configuration. As discussed above, a trade-off must be made between internal and external drag to achieve an optimal balance. The study by van Heerden *et al.* [16] found that the cooling installation drag from the heat exchanger contributed to 2-3% of the total aircraft drag during cruise.

Moreover, the angled positioning causes the airflow to enter and exit the core matrix at oblique angles, reducing the frontal area exposed to the airflow while simultaneously increasing the heat transfer surface area in contact with the air, thereby improving overall heat dissipation [3, 15]. As a result, the core matrix effectively functions as a turning vane system, influencing flow behavior within the duct. Further details on how staggered heat exchangers generate greater oblique flow angles for the same drag penalty can be found in [15, 18].

2.2.3. NOZZLE AND OUTLET

The nozzle and outlet serve two primary functions: regulating the cooling air mass flow rate and exhausting it into the ambient air, with the objective to have minimal drag penalty by recovering some of the momentum of the cooling air [15, 28]. To achieve this, the outlet design must carefully balance the size of the opening, accounting for reductions in air density and internal pressure losses. The outlet area is calculated based on the ratio of cooling air volume per second to the exit velocity. The exit velocity is determined from the exit dynamic pressure, which is defined by the difference between the total pressure behind the heat exchanger and the static pressure at the outlet.

Moreover, in configurations where the ducted wing is submerged within the propeller slipstream, the flow gains additional momentum, increasing the dynamic pressure. Due to the rotational effects of the propeller, the slipstream remains highly non-uniform, with axial velocity components directly contributing to dynamic pressure. As a result, the total pressure at the outlet is influenced not only by the slipstream but also by internal losses from the diffuser and heat exchanger, as highlighted by Katzoff [21]. Under ideal conditions, losses in the converging outlet passage are negligible, according to the same author.

In a cooling installation, the optimal outlet passage is designed as a nozzle with a smoothly converging duct that opens downstream [21]. This type of design minimizes losses by maintaining a favorable pressure gradient along the duct walls. The gradual convergence of the nozzle shape ensures smooth airflow guidance, preventing abrupt changes in direction or cross-sectional area that could induce flow separation. The design of a smoothly converging duct helps prevent boundary layer separation, ensuring efficient airflow management and minimizing drag. An example of a ducted airfoil section, illustrating the smooth duct geometry, is depicted in Figure 2.10. Additionally, a hinged flap at the outlet is used to control the duct mass flow rate, allowing for precise control over cooling performance.

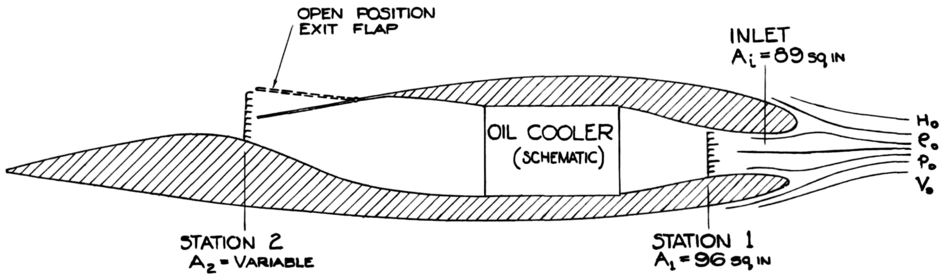

Figure 2.10: Details of a ducted airfoil section [8].

The flow conditions in the vicinity of the outlet, are important in terms of how it affects the mass flow within the duct [18]. In a ducted airfoil, the pressure differential between the upper and lower surfaces influences the mass flow rate. Positioning the outlet on the upper surface, where local pressure is lower than the freestream, creates a larger pressure differential that increases the mass flow rate. Furthermore, the air quantity passing through the outlet naturally adjust with the angle of attack, due to the relative increase in the lift coefficient of the negative pressures at the outlet [29]. In contrast, by placing the outlet on the lower surface, where pressures are higher, reduces the pressure differential, thereby decreasing the mass flow rate.

Sweberg and Dingeldein [29] also investigated how the presence of outlet openings on both the upper and lower surfaces of a wing influenced the stall characteristics of propeller-driven fighter aircraft, as shown in Figure 2.11. Wind tunnel tests on a full-scale model demonstrated that placing the wing-duct outlet on the upper surface increased the maximum lift coefficient, as illustrated in Figure 2.11b. The arrows indicate the specific angles of attack at which the aircraft was set during the wind tunnel tests. While the maximum lift coefficient increases with the outlet on the upper surface, the lift coefficient at lower angles of attack is generally smaller compared to configurations with the outlet on the lower surface. In contrast, placing the outlet on the lower surface results in a higher lift coefficient at lower angles of attack but a slightly reduced maximum lift coefficient overall. Additionally, at high angles of attack, positioning the outlet on the upper surface appears to delay stall compared to when the outlet is on the lower surface, maintaining a similar maximum lift coefficient to that of a plain airfoil [29].

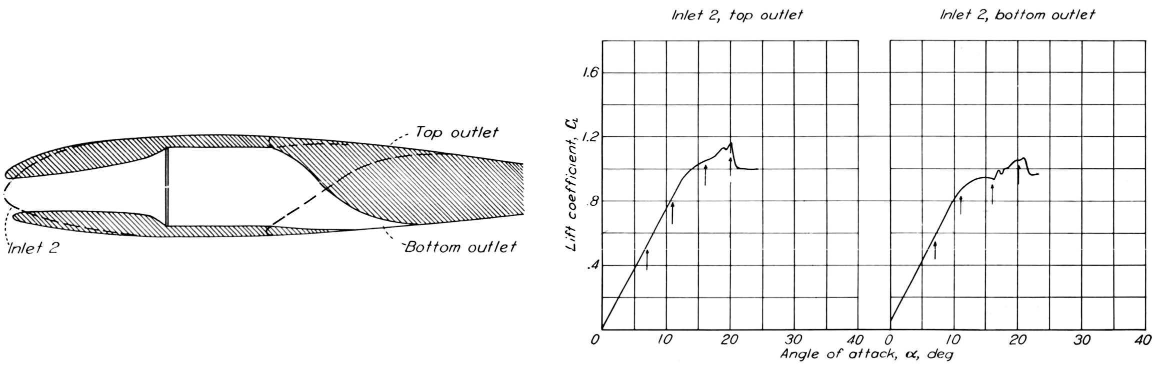

(a) Outlet configurations

(b) Lift coeffienct for the various outlet configurations

Figure 2.11: Effect of wing-duct-outlet location on the stalling characteristic [29].

Furthermore, according to Harris and Recant [10], the placement of the outlet opening on the upper surface of the wing anywhere from 25 to 70% of the chord length can yield high efficiencies. This range allows for greater design flexibility, enabling adjustments to the cooling installation location without significantly affecting the overall aerodynamic performance. Harris and Recant [10] also discovered that when the outlet is smaller in size compared to the inlet, it results in effective boundary-layer control. This can enhance the maximum lift coefficient in comparison to the plain airfoil. As mentioned earlier, the nozzle's outlet area can be made adjustable by employing a hinged flap, as seen in Figure 2.10, allowing it to adapt to different flight conditions. As outlined in Section 2.2.1, the formula for the overall inlet-velocity ratio, shown in Equation 2.1 is composed of the product of external and internal diffusion [23]. The formula can be expressed in terms of pressure coefficient and area ratios between the exit station (e) and station (b), as indicated by the control volume as shown in Figure 2.5. This same formula, as shown in Equation 2.5, is derived from theory concepts detailed in Küchemann and Weber [18].

$$\frac{V_b}{V_o} = \left(\frac{V_i}{V_o}\right)\left(\frac{V_b}{V_i}\right) \sim \sqrt{\frac{-C_{p_e}}{C_{p_b} + \left(\frac{A_b}{A_e}\right)^2}} \tag{2.5}$$

where C_{p_e} represents the pressure coefficient calculated from the difference in static pressure between the exit and the ambient air, while C_{p_b} denotes the pressure coefficient derived from the total pressure drop across the heat exchanger core, according to Martin [12]. Given that the geometry of the diffuser is fixed, the area A_b and consequently the ratio of internal diffusion V_b/V_i remain constant. This implies that the amount of external diffusion V_i/V_o is controlled by the exit area A_e [12]. Therefore, the flap serves dual functions as both a throttle and a pump, regulating the overall inlet-velocity ratio V_b/V_o and thereby controlling the flow of cooling air [12, 15]. Throttling is used during cruising to reduce cooling drag by reducing the cooling air flow that sufficiently meets the cooling requirements, while pumping is used during climbing or ground operations to induce adequate cooling air flow [15]. Ideally, the angle of the flap should be adjusted to ensure that any increase in drag is minimized. Miley [15] points out that positioning the outlet in a low-pressure region on the wing to enhance pumping and thus increase cooling flow may result in increased external friction drag and pressure drag due to flow separation. However, decreasing the outlet size to throttle flow at high speeds can reduce overall efficiency, even though it may lower the power required for cooling [10]. Piancastelli *et al.* [30] and Eissele *et al.* [31] noted that using the Meredith effect can reduce the drag caused by the cooling installation.

2.3. WING-BODY JUNCTURE FLOW PHENOMENA

The aerodynamic performance of aircraft is strongly influenced by the flow characteristics at wing-body junctions, where complex interactions between boundary layers and vortical structures occur. These junction flows, prevalent in wing-fuselage and wing-nacelle configurations, occurs when the boundary layer from a smooth surface, such as a fuselage or nacelle, impinges on an attached obstacle, like a wing. This interaction triggers three-dimensional boundary layer separation well upstream of the wing due to the streamwise adverse pressure gradient induced by the wing [32, 33]. The wing's boundary layer interacts with the incoming boundary layer, resulting in the formation of strong coherent vortical structures, such as horseshoe vortices (HSVs), secondary corner vortices, and potential separation in corner regions [32, 33]. The resulting interference drag, caused by the mixing of boundary layers and locally increased turbulence, makes the flow in the junction vicinity highly complex and anisotropic [32, 34]. This drag can account for up to 10% of the total drag on modern aircraft, according to Gand *et al.* [35], emphasizing the importance of optimizing these junction regions. Recent advancements in drag reduction strategies, such as the development of anti-fairings by Belligoli *et al.* [36], have shown promising results in modifying junction flow behavior. Unlike traditional convex fairings or so called leading-edge fillets, anti-fairings use concave geometries to generate favorable pressure forces, thereby reducing interference drag and improving overall aerodynamic performance. Adding fairings improve the lift-to-drag ratio at several angles of attack [36].

While junction flows are well-documented in traditional wing-body configurations [33–40], their behavior in propeller-driven aircraft with wing-integrated ram-air ducts remains an open area of investigation, introducing additional complexities. The junction flow in a nacelle/ducted-wing configuration is particularly complex due to the intricate geometry involved. Unlike conventional wing-body junctions, the presence of a ram-air duct results in the wing being divided into upper and lower surfaces that enclose the duct. These surfaces, shaped from a reference airfoil profile with an altered inlet, interact with both the freestream flow and the nacelle boundary layer. The presence of the ducted heat exchanger causes this interaction to introduce unprecedented aerodynamic phenomena, making the flow dynamics in this configuration a novel field of investigation. The interaction of the two airfoil-like surfaces in close proximity, the heat exchanger's flow resistance, and the nacelle boundary layer further complicate the flow dynamics in the junction regions. The HSV forms due to the strong streamwise adverse pressure gradient near the wing leading-edge, and its characteristics become dependent on the heat exchanger flow resistance. Furthermore, the interaction between the two perpendicular boundary layers at the nacelle/ducted-wing junction can induce corner flow separation, which are triggered by gradients of the Reynolds stresses [35, 37]. This can lead to increased turbulence production, drag, and pressure losses at the nacelle-wall juncture. Thus, these secondary flow structures in the junction region further impair aircraft aerodynamics by contributing to interference drag. The following section elaborate on the typical flow characteristics of junction flows, with a specific focus on their implications for wing-integrated duct designs. This understanding is essential to accurately interpret the flow behavior and draw reliable conclusions for optimal wing-integrated duct performance using numerical methods in this research.

2

2.3.1. TYPICAL FLOW CHARACTERISTICS OF JUNCTION FLOWS

To understand the flow behavior at wing-body junctions under realistic conditions, numerous studies have focused on simplified configurations, such as a wing profile mounted perpendicularly on a flat plate. This configuration allows for a detailed study of the complex interactions between boundary layers and vortical structures, as thoroughly investigated by many authors [33–40]. An overview of the typical flow behavior in wing-body junctions is shown in Figure 2.12, which reveals two key secondary flow phenomena. Near the leading-edge, a HSV forms as the incoming boundary layer separates and wraps around the wing, convecting in the streamwise direction near the surface while gradually diffusing and extending into the wake. Furthermore, near the junction, corner separations may develop close to the trailing-edge as the boundary layers respond to both streamwise and spanwise pressure gradients. Combined with the downstream convection of the HSV, these gradients contribute to the highly anisotropic and turbulent flow characteristic of the junction region. In turbulent flow regimes, the HSV dominates the junction flow and impairs aerodynamic performance by increasing interference drag. However, while a large corner separation area can have an even greater impact on drag, its formation and underlying conditions are not yet fully understood, according to Belligoli *et al.* [36]. To further understand the global dynamics of junction flow phenomena, each key secondary flow feature is detailed below.

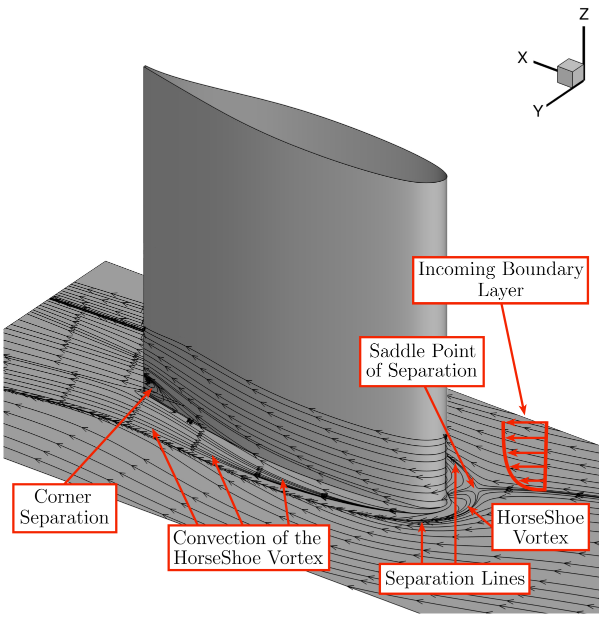

Figure 2.12: Overview of typical flow behavior in a wing-body junction configuration, based on data from Gand *et al.* [37].

HORSESHOE VORTEX

The HSV is considered a secondary flow of the first kind, as described by Prandtl [37]. This vortical flow structure forms as the streamwise pressure gradient induced by the wing causes the incoming boundary layer to decelerate, separate, and roll up into multiple coherent vortices. As shown in Figure 2.12, the saddle point, also referred to as the 3D stagnation point, upstream of the leading-edge indicates the onset of boundary layer separation, marking the initiation of the HSV [33]. The separation lines pass through the stagnation point, extending around both sides of the wing where the flow separates from the flat plate [32, 33]. The continual freestream flow fills the leading-edge separation zone, while the HSV legs wrap around the wing and convect swirling structures downstream, where the initially large velocity gradients gradually reduce as the vortices convects [37, 39]. Diffusion of the mean flow quantities takes place as the vortex convects downstream, remaining visible in the wake region of the wing-body junction [37]. Furthermore, the legs of the HSV have opposite vorticity, with one leg showing the same rotational direction as the vorticity of the incoming boundary layer. Additionally, smaller secondary vortices form along each leg, featuring vorticity in the opposite direction to maintain the streamline topology [33]. Simpson [33] found that the HSV is unsteady in terms of its location, size, and circulation. Moreover, according to Fleming *et al.* [38], the strength and stretching rate of the HSV depend on the Bluntness Factor (BF) of the wing's leading-edge and the Momentum Deficit Factor (MDF) to quantify the influence of the incoming boundary layer [34].

The BF is a parameter that depends on the geometry of the wing, specifically the shape from the leading-edge to the maximum thickness of the airfoil profile, and is defined as

$$\mathrm{BF} = \frac{1}{2}\frac{R_0}{X_T}\left[\frac{T}{S_T} + \frac{S_T}{X_T}\right] \tag{2.6}$$

where X_T represents the chordwise position of the maximum thickness T of the airfoil, S_T is the length measured along the surface curvature from the leading-edge to the point of maximum thickness, and R_0 is the leading-edge radius [32–34, 37]. An experimental investigation by Mehta [40] focused on the impact of various leading-edge shapes on junction flow, revealed that a rounded leading-edge generates a stronger HSV with a higher stretching rate, whereas a sharper leading-edge creates a weaker HSV [37].

Furthermore, the MDF is a dimensionless parameter that depends on both the Reynolds number based on the momentum thickness (θ) of the incoming boundary layer at an upstream location x, and the Reynolds number based on the maximum thickness of the airfoil, and is defined as:

$$\mathrm{MDF}_x = Re_{\theta_x} \cdot Re_T \tag{2.7}$$

This relation quantifies the combined effects of the incoming boundary layer momentum thickness and the airfoil thickness on junction flow dynamics. Specifically, it characterizes how the interaction between the boundary layer momentum distribution and the wing-induced pressure gradient influences the strength and positioning of the HSV near the airfoil's maximum thickness. An increase in Re_T causes the HSV to move closer to the wing, reducing its vertical extent. However, for fixed flow conditions, Re_T remains constant, and MDF becomes a function of the boundary layer momentum thickness θ only. A higher MDF, which corresponds to a larger boundary layer momentum deficit, correlates with a stronger response to the adverse pressure gradient imposed by the wing, leading to an earlier and stronger HSV formation. As a result, its vortex core remains closer to the surface, with vorticity increasingly concentrated near the wall, resulting in a more elliptic shape [38]. This intensifies wake interactions, leading to greater unsteadiness in the junction region, which in turn increases turbulence levels and drag [33, 38]. Additionally, the vortex legs move further apart in the spanwise direction within the wake, increasing vortex-induced interactions [33]. In contrast, a lower MDF is associated with a lower boundary layer momentum deficit, resulting in less intense HSV formation. As a result, wake interactions are weaker, and overall aerodynamic losses, such as interference drag and turbulence production, are mitigated.

2

CORNER SEPARATION

Corner separation occurs at the junction of a flat plate and a wing due to adverse pressure gradients in both the streamwise and spanwise directions. These competing gradients induce strong three-dimensional velocity variations, generating highly anisotropic turbulence in the junction region, making it more prone to separation. It is recognized as a secondary flow of Prandtl's second kind [33], this phenomenon is triggered by gradients in Reynolds stresses, which increase turbulent momentum transfer within the junction boundary layer [35, 41]. The interaction between the HSV and corner separation has been less extensively studied, according to Gand *et al.* [37]. However, Barber [39] conducted a detailed experiment that led to the development of a model describing the interaction between the HSV and the corner separation, as depicted in Figure 2.13. The findings indicate that the behavior of junction flow is predominantly governed by the values of the Bluntness Factor (BF) and the Momentum Deficit Factor (MDF) [37], as discussed earlier. The vorticity of the HSV can interact with the local adverse pressure gradients, influencing corner separation depending on the vortex strength. In Figure 2.13a, a thick incoming boundary layer results in a stronger HSV, which brings higher-momentum fluid from outside the boundary layer into the corner region. This process energizes the near-wall flow, enhancing the ability to sustain the adverse pressure gradient and delaying the onset of separation and flow reversal in the corner. However, while this increases the skin friction drag due to the steeper velocity gradients, preventing flow separation helps avoid the much larger pressure drag that would otherwise result from a separated flow region. In contrast, as shown in Figure 2.13b, a thinner incoming boundary layer generates a weaker HSV, which is less effective at pulling high-momentum fluid into the corner region. Consequently, this leads to larger corner separations, increasing drag and reducing overall aerodynamic efficiency.

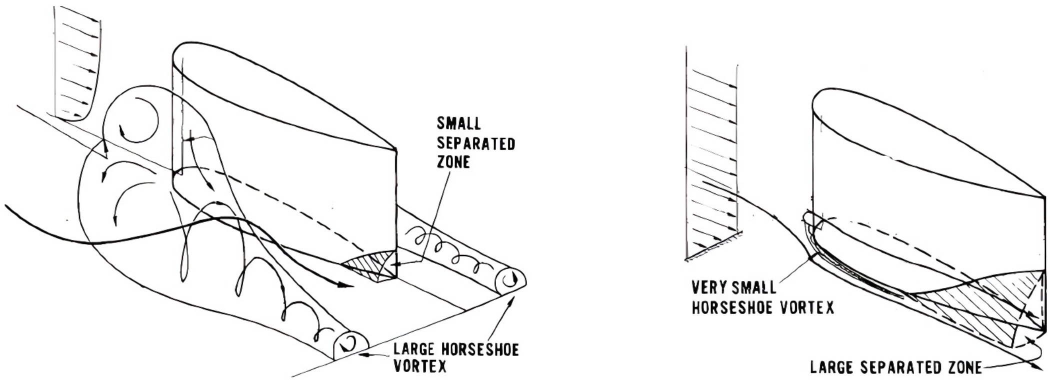

(a) Thick boundary layer

(b) Thin boundary layer

Figure 2.13: Boundary layer and wing interactions effect on corner flow separation [37, 39].

Part II

Methodology

3

NUMERICAL SET-UP

This chapter describes the numerical set-up used to analyze the aerodynamic performance of the wing-integrated duct and the flow behavior at the wing-body junction. This research utilizes viscous RANS CFD simulations to efficiently explore a wide range of duct designs through Design of Experiments (DoE), providing a cost-effective and time-efficient alternative to experimental campaigns while offering detailed insights into the flow field. The chapter covers the governing equations for RANS simulations, turbulence modeling, operating conditions, 2D and 3D computational domains and boundary conditions, and the mesh setup. To validate the numerical setup, the RANS methodology is first assessed using a baseline airfoil case. Additionally, a thermal and pressure drop analysis of the heat exchanger is performed to assess its impact on aerodynamic performance.

3.1. GOVERNING EQUATIONS

Steady-state viscous RANS simulations are necessary for accurately capturing the complex flow physics around the intricate geometry of wing-integrated ram-air ducts and junction flow phenomena. Unlike inviscid approaches, viscous RANS calculations account for a range of critical aerodynamic effects, including boundary layer development, pressure distribution, flow separation, wake behavior, and secondary flow structures such as HSV and corner separation at the wing-body junction. By resolving these effects, RANS simulations provide for a detailed analysis of the aerodynamic performance of ducted wings, capturing the external flow characteristics and their interaction with the internal duct flow through the heat exchanger. As a result, including viscous effects is essential for investigating how different wing-integrated duct designs impact the overall drag of the cooling installation.

The Navier-Stokes (NS) equations for a Newtonian fluid, governing conservation of mass (Equation 3.1) and momentum (Equation 3.2), are given as follows:

$$\frac{\partial \rho}{\partial t} + \nabla \cdot (\rho \mathbf{u}) = 0 \tag{3.1}$$

$$\rho \left(\frac{\partial \mathbf{u}}{\partial t} + (\mathbf{u} \cdot \nabla)\, \mathbf{u} \right) = -\nabla p + \mu \nabla^2 \mathbf{u} + \rho \mathbf{g} + \mathbf{S_m} \tag{3.2}$$

where ρ represents the fluid density, $\mathbf{u}$ denotes the velocity vector field, p is the static pressure, μ is the dynamic viscosity, $\mathbf{g}$ is the gravitational acceleration vector, and $\mathbf{S_m}$ accounts for the momentum source term, such as those for porous media or user-defined sources [42]. RANS simulations decompose the solution variables in the instantaneous NS equations into a time-averaged mean component and fluctuating components to account for the effects of turbulence [42]. In this approach, the Reynolds decomposition is applied to the velocity vector and any scalar quantities as follows:

$$\mathbf{u} = \overline{\mathbf{u}} + \mathbf{u}', \quad \varphi = \overline{\varphi} + \varphi' \tag{3.3}$$

3

where $\overline{\mathbf{u}}$ and $\overline{\varphi}$ represent the time-averaged components, and $\mathbf{u}'$ and φ' denote the fluctuating components. Substituting these decompositions into Equation 3.1 and Equation 3.2 and applying the Reynolds averaging rules results in the following equations:

$$\frac{\partial \overline{\rho}}{\partial t} + \nabla \cdot \left(\overline{\rho \mathbf{u}}\right) = 0 \tag{3.4}$$

$$\overline{\rho}\left(\frac{\partial \overline{\mathbf{u}}}{\partial t} + \left(\overline{\mathbf{u}} \cdot \nabla\right)\overline{\mathbf{u}}\right) = -\nabla \overline{p} + \mu \nabla^2 \overline{\mathbf{u}} + \overline{\rho}\mathbf{g} + \overline{\mathbf{S_m}} - \nabla \cdot \left(\overline{\rho \mathbf{u}'\mathbf{u}'}\right) \tag{3.5}$$

The addition term $\boldsymbol{\tau} = -\overline{\rho \mathbf{u}'\mathbf{u}'}$ in the momentum equation represents the Reynolds stress tensor, which results from turbulent fluctuations introduced by the nonlinear convective term in the NS equations. Its second-order symmetric nature introduces six additional unknowns in the RANS equations ($-\overline{\rho u_i' u_j'}$): three normal stresses and three off-diagonal shear stresses. However, in the case of 3D flow, the RANS equations provide only four equations (three for momentum and one for continuity) to solve for the mean flow quantities. This imbalance leads to the closure problem, as no governing equations exist for the additional Reynolds stresses, resulting in an underdetermined system of equations with ten unknowns. To address this, empirical approximations such as turbulence models are employed to represent the effects of turbulence in the averaged momentum equations, providing the necessary closure to solve the system. Details about the specific turbulence model used in this research are provided in the following section. Since a steady-state approach is assumed, the time derivative term in the continuity and momentum equations is omitted, as temporal variations in the flow field are not considered. This assumption implies that all flow properties are resolved as time-invariant, and any transient flow phenomena, including vortex shedding and unsteady separation, are inherently excluded from the analysis.

Furthermore, in this research, the system of Partial Differential Equations (PDEs) governing fluid flow are discretized into algebraic equations over finite volumes using a CFD solver. RANS simulations are particularly suited for this investigation as it captures the mean flow behavior of turbulent flows while offering significantly lower computational costs compared to Direct Numerical Simulation (DNS) or Large Eddy Simulation (LES). For the high Reynolds numbers and intricate geometries involved, resolving all turbulent scales as in DNS is computationally expensive. Similarly, while LES effectively resolves large-scale turbulence, its requirement for fine grids and small time steps near walls, along with its inherently time-dependent formulation, makes it unfeasible for this study due to the extensive geometrical parameter sweeps involved in the DoE approach.

3.2. TURBULENCE MODELING

Using RANS simulations requires selecting an appropriate turbulence model to close the set of equations by approximating the effects of the Reynolds stress tensor. In this research, a linear

Eddy Viscosity Model (EVM) is used based on the Boussinesq hypothesis [42], which assumes that the Reynolds stress tensor scales linearly with the mean strain rate tensor, given in tensor form as:

$$-\overline{\rho u_i' u_j'} = \mu_t \left(\frac{\partial \overline{u}_i}{\partial x_j} + \frac{\partial \overline{u}_j}{\partial x_i} \right) - \frac{2}{3} \rho k \delta_{ij} \tag{3.6}$$

where μ_t is the turbulent (eddy) viscosity, $\left(\frac{\partial \overline{u}_i}{\partial x_j} + \frac{\partial \overline{u}_j}{\partial x_i} \right)$ is the mean strain rate tensor, k is the turbulent kinetic energy ($\frac{1}{2}\overline{\rho u_i' u_i'}$), and δ_{ij} is the Kronecker delta which assumes turbulence is isotropic [42]. The Reynolds stress tensor, which introduced six additional unknowns, is now reduced to a single new unknown, which is the eddy viscosity μ_t. The eddy viscosity is a turbulence model quantity that represents the effective turbulent mixing of momentum due to large turbulent eddies, and is different from molecular viscosity (μ). Moreover, since μ_t is not directly known, it must be approximated using a turbulence model to achieve closure of the RANS equations. The EVM was chosen because it is relatively less computationally expensive while still providing accurate results. In contrast, Reynolds Stress Model (RSM) directly solve transport equations for each component of the Reynolds stress tensor, making it much more computationally expensive but accurate. Due to the large number of ducted wing design variations in the DoE study, RSM was not considered feasible for this research.

Furthermore, in this research, a two-equation turbulence model is used, solving two additional transport equations, one for the turbulent kinetic energy k, which represents turbulence intensity, and another for either the turbulence dissipation rate ϵ or the specific dissipation rate ω, both of which describe the rate at which turbulence is dissipated. The k-ω Shear Stress Transport (SST) turbulence model by Menter [43] is used, which blends the two separate k-ϵ and k-ω models, combining their respective advantages. The blending is achieved through a switching function, where Wilcox's k-ω model is superior in capturing boundary layer effects near walls, while the k-ϵ model is applied in free shear flows, as it performs poorly in regions with strong adverse pressure gradients and flow separation [43].

Moreover, the k-ω SST model is extended with the γ-Re_θ transition model, which improves the turbulence model's ability to capture flow separation and transition effects more accurately. This makes it particularly useful for aerodynamic applications where boundary layer transition significantly impacts drag and performance. The γ equation models intermittency, which controls the transition from laminar to turbulent flow, while the Re_θ equation estimates the Reynolds number based on the boundary layer momentum thickness, which is used to predict the onset of transition. Although fully turbulent flow is assumed in this study, the intermittency γ is set to one, effectively bypassing transition modeling. However, the γ-Re_θ transition model still refines turbulence production and dissipation terms, leading to more accurate boundary layer development and improved predictions of separation and aerodynamic performance compared to standard turbulence models. For completeness, additional turbulence models are tested in Section 3.7.4 to provide insights into the sensitivity of the results to turbulence model selection.

3.3. RANS SOLVER SET-UP

Throughout this study, steady RANS simulations were conducted using ANSYS® Fluent, a commercial finite volume CFD solver that discretizes the governing PDEs of the continuous physical domain into finite control volumes over which the RANS equations are solved. Furthermore, Fluent was chosen for its robust porous media modeling capabilities and its flexibility in incorporating source terms into the governing energy equation, allowing for an accurate representation of the heat exchanger's influence on aerodynamic forces through pressure drop and thermal effects. The simulations must accurately represent the intended flow conditions, therefore this section provides an overview of the numerical setup, including flow assumptions, solver selection, and discretization schemes.

The simulations in this study serve as a benchmark for future wind tunnel validation, with operating conditions set at sea level for low subsonic flow ($M < 0.3$). This permits the assumption of incompressible flow and the use of a pressure-based solver. When the heat transfer source term is activated, the energy equation is solved using the incompressible ideal gas law, which allows density to vary with temperature while neglecting pressure effects. In this formulation, density is a function of the operating pressure but remains unaffected by local pressure variations in the flow field [44], as pressure fluctuations at low subsonic Mach numbers are too small to have a significant impact on density. This relationship is defined by the equation of state in Equation 3.7, where p_{op} is the operating pressure set to 101 325 Pa, and R is the specific gas constant. This temperature-dependent density variation is necessary to capture thermal expansion effects of the heat exchanger within the ducted nozzle flow.

$$\rho = \frac{p_{\text{op}}}{RT} \tag{3.7}$$

Additionally, the dynamic viscosity μ is computed using Sutherland's law, which provides a temperature-dependent model for viscosity. This formulation is widely used for gases at moderate temperatures and is given as [44]:

$$\mu(T) = \mu_0 \left(\frac{T}{T_0}\right)^{\frac{3}{2}} \frac{T_0 + S}{T + S} \tag{3.8}$$

where $\mu(T)$ is the dynamic viscosity at temperature T, μ_0 is the reference dynamic viscosity at the reference temperature T_0, and S is Sutherland's constant, which is specific to the gas being modeled.

Furthermore, the Coupled algorithm is employed for pressure-velocity coupling, as it solves the momentum and continuity equations simultaneously within a single system, reducing numerical errors associated with iterative decoupling. This scheme is particularly well-suited for handling aerodynamic flows with strong pressure gradients and flow separation. To improve numerical resolution and minimize truncation errors, 2$^{\text{nd}}$ order spatial discretization schemes are applied to pressure, momentum, intermittency (γ), turbulence kinetic energy (k), and specific dissipation rate (ω) using a 2$^{\text{nd}}$ order upwind scheme, enhancing solution accuracy and stability. The solution is initialized using hybrid initialization, which solves Laplace's equation for velocity and pressure to enhance stability and accelerate convergence [42]. To ensure a well-converged solution, the residuals for all governing equations are required to drop below 10^{-3}, following best practices for steady RANS simulations. At high angles of attack, flow unsteadiness introduces oscillatory residual behavior due to increased separation and vortex shedding. In such cases, the solution is considered converged when the residuals stabilize within a bounded range, and the aerodynamic forces are monitored for consistency before extracting final values. For steady flow conditions, residuals typically exhibit monotonic decay, reflecting numerical stability and convergence.

The 2D and 3D CFD simulation process, is outlined in the flowchart presented in Figure 3.1. A Python script was created to automate the execution of simulations on the high-performance computing (HPC) cluster, where the pre-generated mesh is loaded, physics models, material properties, and solver settings are applied as detailed in this section, and the appropriate boundary conditions, as described in Section 3.5, are configured.

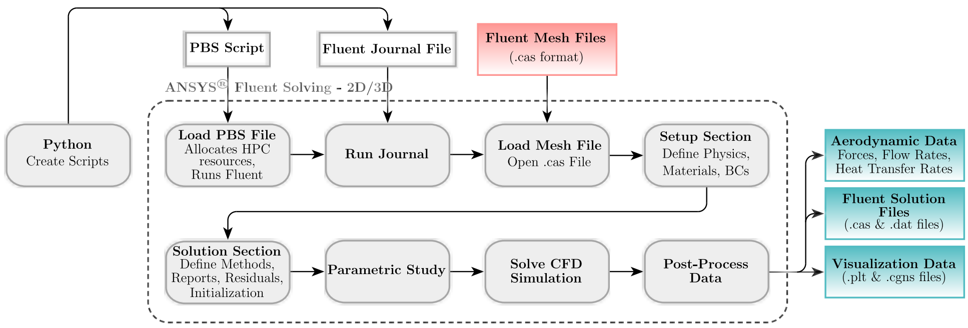

Figure 3.1: CFD simulation flowchart on the HPC.

3.4. DESIGN OF EXPERIMENT AND GEOMETRICAL PARAMETRIZATION

Design of Experiments (DoE) is a structured statistical method used to analyze the relationships between input variables (factors) and output responses, enabling a systematic exploration of system behavior and identification of key interactions among input variables [45]. A full factorial design approach is used to systematically evaluate the effects of multiple factors on a response variable by evaluating all possible combinations of their levels. This method provides a thorough exploration of the design space, allowing for the estimation of main effects and interactions between factors without the need for physical replication or randomization, as numerical simulations are deterministic [45]. By systematically varying factors, the factorial design evaluates the aerodynamic characteristics and performance of the wing-integrated duct, establishing a robust framework for parameter sensitivity analysis and offering insights into the underlying aerodynamic principles.

Factor	Level 1	Level 2	Level 3	Level 4	Level 5
R_u	0.01	0.02	-	-	-
R_l	0.01	0.02	-	-	-
LDR	0.2	0.3	0.4	-	-
d/c	0.095	0.105	0.115	-	-
φ	0°	10°	20°	30°	40°
t_{hx}/c	0.05	0.10	0.15	-	-
x_{hx}/c	0.200	0.225	0.250	0.275	-
ε	0.72	0.81	0.88	-	-

Table 3.1: Factors and corresponding levels for the DoE full-factorial design study.

Table 3.1 summarizes the input factors and their respective levels under consideration. With eight factors and multiple levels, the design test matrix consists of 6480 unique configurations of a wing-integrated duct for exploration. This setup captures and evaluates all main and higher-order interactions for their impact on the system response, including lift, drag, and duct mass flow rate. The selected factors were identified as critical to the performance and geometry of the wing-integrated duct system.

The geometric parameters considered in the ducted airfoil design, including the radii of the upper and lower airfoil lips (R_u, R_l), leading-edge droop ratio (LDR), gap-to-chord ratio (d/c), stagger angle (φ), the heat exchanger thickness-to-chord ratio (t_{hx}/c), position-to-chord ratio (x_{hx}/c), and porosity (ε), are selected for their critical influence on the aerodynamic and thermal performance of the system. Below, the significance and motivation behind each factor are explained, showing how they affect key performance metrics:

3

- **Lip radii (R_u, R_l):** Control duct lip curvature, affecting flow separation by altering stagnation point location and entry losses.
- **Leading-edge Droop Ratio (LDR):** Defines the vertical offset of the lip, scaled by the gap-to-chord ratio ($\frac{\Delta h}{d/c}$), to align duct flow entry, especially at high angles of attack.
- **Gap-to-chord ratio (d/c):** Determines the spacing between the upper and lower lips, affecting pressure recovery, flow stability, and mass flow rate through the duct.
- **Stagger angle (φ):** Adjusts the angle of the lower airfoil relative to the upper airfoil, resulting in a chordwise displacement that impacts aerodynamic performance by altering the interaction between the two airfoils and optimizing the entry flow alignment with the external airflow.
- **Heat exchanger parameters (t_{hx}/c, x_{hx}/c, ε):** Define the thickness and position of the heat exchanger, normalized by the chord length, along with its porosity. These parameters directly influence the aero-thermal performance by affecting heat transfer, pressure drop, and both internal and external aerodynamics.

By parameterizing the ducted airfoil in this manner, the study performs a systematic evaluation of aerodynamic interactions within the system, capturing the effects of key geometrical variations on flow behavior, pressure distribution, and heat transfer. Figure 3.2 presents the geometrical parametrization, providing a visual representation of the parameters being investigated. Furthermore, four different outlet positions are analyzed, with all configurations sharing the same geometric parametrization up to the point of maximum thickness-to-chord ratio. To simplify the ducted airfoil representation, the aft section beyond the maximum thickness-to-chord ratio is excluded, as observed in Figure 3.2. The outlets are positioned aft of the maximum thickness and in the vicinity of the trailing-edge on both the upper and lower surfaces of the airfoil, providing further insights into their impact on the aero-thermal performance.

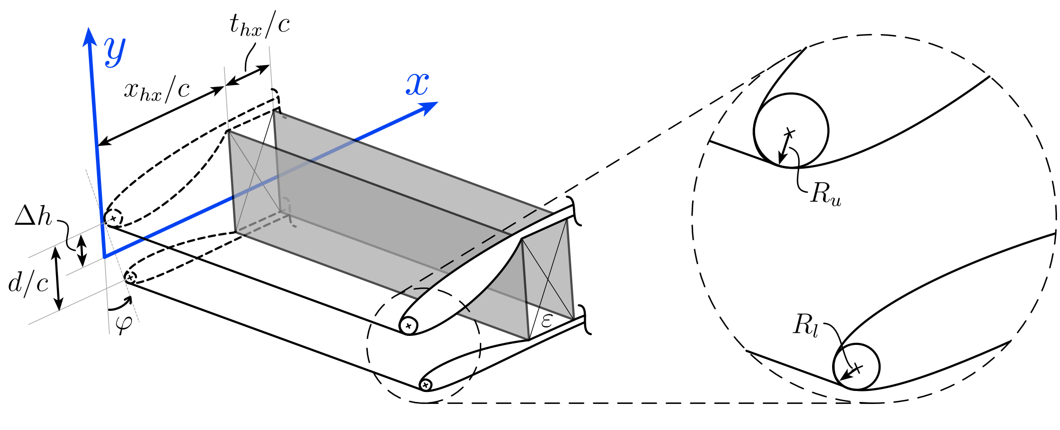

Figure 3.2: Geometrical parametrization of the ducted wing.

The geometry generation process for the ducted airfoil, as shown in the flowchart provided in Figure 3.3, represents the first step in the CFD workflow, providing the input geometry necessary for meshing and fluid domain creation. The ducted airfoil geometry modeled in this research is based on the NASA MS(1)-0317 medium-speed airfoil, selected for its relevance to the application, as detailed in Section 3.7.1. This airfoil serves as the base shape, allowing for a comparative analysis of aerodynamic performance differences introduced by the ducted airfoil geometry. Using CAD software, the duct housing the heat exchanger was designed within the airfoil while preserving its outer contour to maintain the base airfoil shape. The inlet and heat exchanger volume of the ducted airfoil geometry were parameterized, as shown in Figure 3.2. The DoE test matrix was subsequently imported into the CAD software, where Python scripts automated the generation of the 2D ducted airfoil geometries by applying the specified parameter variations listed in Table 3.1.

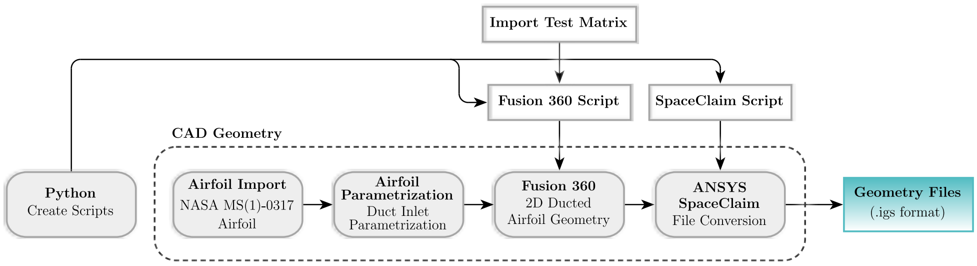

Figure 3.3: Airfoil geometry generation flowchart.

3.5. DOMAINS AND BOUNDARY CONDITIONS

This section describes the computational domains and their associated boundary conditions (BCs) for both 2D and 3D RANS simulations. The computational domains are applicable to both the basic wing and the wing-integrated duct. The effect of varying outer domain dimensions, and thus the influence of boundary conditions on the flow field in the vicinity of the wing, is analyzed through aerodynamic coefficients, as provided in Section B.2.

3.5.1. TWO-DIMENSIONAL

For the DoE full-factorial study and the basic wing, 2D simulations were performed to study aerodynamic performance. The c-type computational domain is illustrated in Figure 3.4. The inlet is situated $20c$ upstream of the wing, while the outlet is placed $30c$ downstream, to minimize disturbances in the static pressure field and other flow properties in the vicinity of the wing. Symmetry BCs are applied to the sides of the domain to replicate an infinite wing, effectively eliminating 3D aerodynamic effects. With the wing held static in the domain, a velocity-inlet BC is applied at the inlet to define the x and y velocity components, enabling adjustments for different angles of attack. Additionally, turbulence properties are prescribed at the inlet, including intermittency (γ), turbulence intensity (I), and turbulence length scale (L_t), which influence boundary layer transition and turbulence development. At the outlet, the gauge pressure was set to zero to match the freestream static pressure, as defined by the operating pressure, and is therefore relative to it. Furthermore, the wing is specified with a no-slip BC, imposing zero velocity at the wall to accurately capture boundary layer effects. Finally, the porous medium (PM) inlet and outlet are set as interfaces, allowing to transfer flow variables such as velocity, pressure, and turbulence quantities between adjacent zones. The domain is extruded by a single cell in the z-direction over a span of $1c$, effectively creating a quasi-3D

3

problem, as no significant variations can develop in this direction due to the symmetry BCs.

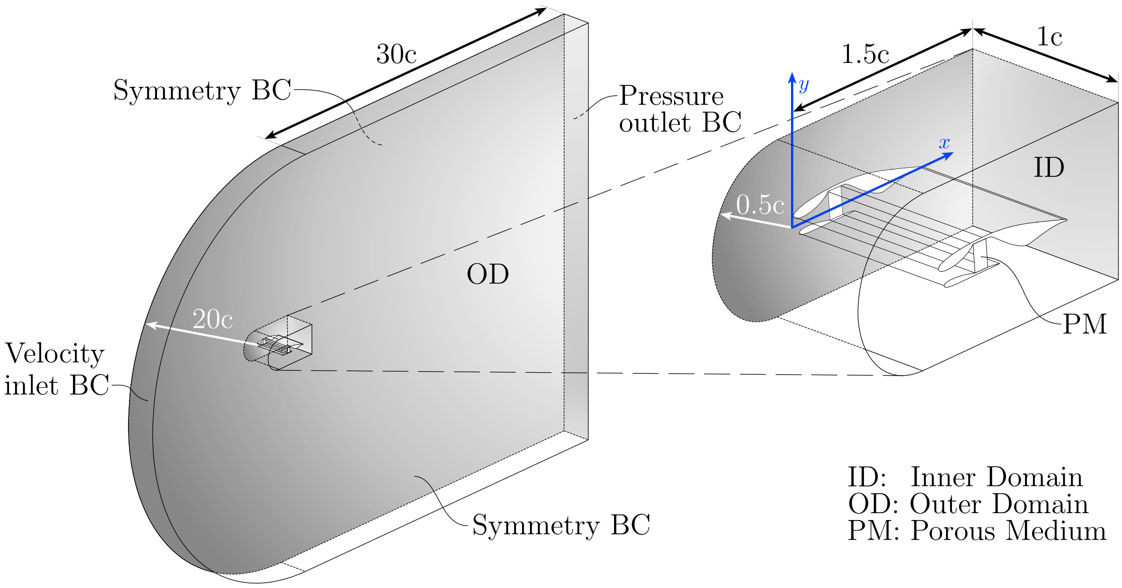

Figure 3.4: 2D computational domain and boundary conditions for a ducted wing with the heat exchanger modeled as a porous medium.

3.5.2. THREE-DIMENSIONAL

For the basic and ducted wing configurations, 3D simulations were performed to analyze aerodynamic performance characteristics and investigate wing-body junction flow phenomena. To capture the juncture flow of the nacelle/ducted-wing configuration, the basic and ducted wing profiles are mounted perpendicularly on a flat plate. The transition from a full 3D analysis to a quasi-3D analysis is motivated by both computational cost and theoretical considerations. While full 3D simulations provide a complete representation of flow interactions, they introduce added complexity due to curvature effects, 3D boundary layer development, and spanwise pressure gradients. By simplifying the problem to a quasi-3D case, where the ducted wing is mounted on a flat plate, key aerodynamic phenomena such as junction flow behavior and boundary layer development can be isolated without additional complexities introduced by nacelle contour effects. The flat plate extends $1c$ upstream of the wing, as shown in Figure 3.6, allowing the boundary layer to develop naturally and transition into a turbulent state before interacting with the wing. This approach is particularly beneficial for investigating the impact of heat exchanger induced flow resistance on junction flow, as it eliminates confounding factors and helps in the development of general aerodynamic theories. This methodology aligns with established aerodynamic research practices for junction flows, where fundamental flow mechanisms are typically investigated on flat plates before including full 3D complexities. Moreover, this approach allows for systematic parametric studies, allowing aerodynamic effects to be analyzed in a controlled manner before transitioning to a full 3D analysis. Additionally, it also serves as a validation step to ensure the methodology is robust before refining the model further. An illustration of this abstraction process is shown in Figure 3.5, where the full 3D case represents the complete nacelle/ducted-wing configuration, capturing all spatial interactions and flow complexities. In contrast, the quasi-3D case simplifies the analysis by considering a representative spanwise section, reducing computational cost while preserving key aerodynamic characteristics.

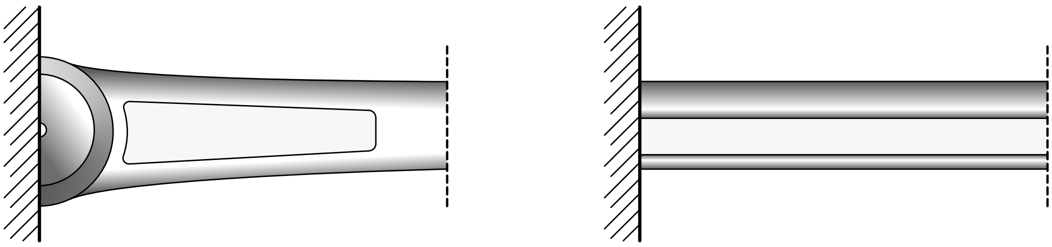

(a) Full 3D case

(b) Quasi-3D case

Figure 3.5: Illustration of the abstraction process for aerodynamic analysis of the ducted wing (front view). The full 3D case captures the complete nacelle/ducted-wing configuration, while the quasi-3D case simplifies the analysis by considering a representative spanwise section, reducing computational cost.

Furthermore, the c-type computational domain is illustrated in Figure 3.6. Similarly to the 2D domain, the inlet is situated $20c$ upstream of the wing, while the outlet is placed $30c$ downstream, to minimize disturbances in the static pressure field and other flow properties in the vicinity of the wing. Symmetry BC is applied to the right side of the domain to replicate an infinite wing, effectively eliminating 3D aerodynamic effects on that side. The velocity-inlet and pressure-outlet BCs are identical to those used in the 2D domain, as discussed previously. Furthermore, both the wing and the flat plate were specified with no-slip BCs. This imposes zero velocity at the wall, accurately capturing boundary layer effects. The flat plate extends $1c$ ahead of the wing, allowing the boundary layer to naturally develop and transition into a turbulent state before interacting with the wing, as mentioned earlier. In the regions outside the flat plate, a slip BC is imposed to neglect wall friction, preventing additional boundary layer growth, as illustrated in Figure 3.6. Finally, the porous medium (PM) inlet and outlet are set as interfaces, allowing to transfer flow variables such as velocity, pressure, and turbulence quantities between adjacent zones. The domain is extruded by multiple cells in the z-direction over a span of $1c$ to create a prism layer, ensuring proper resolution of the boundary layer development on the flat plate with $y^+ \leq 1$.

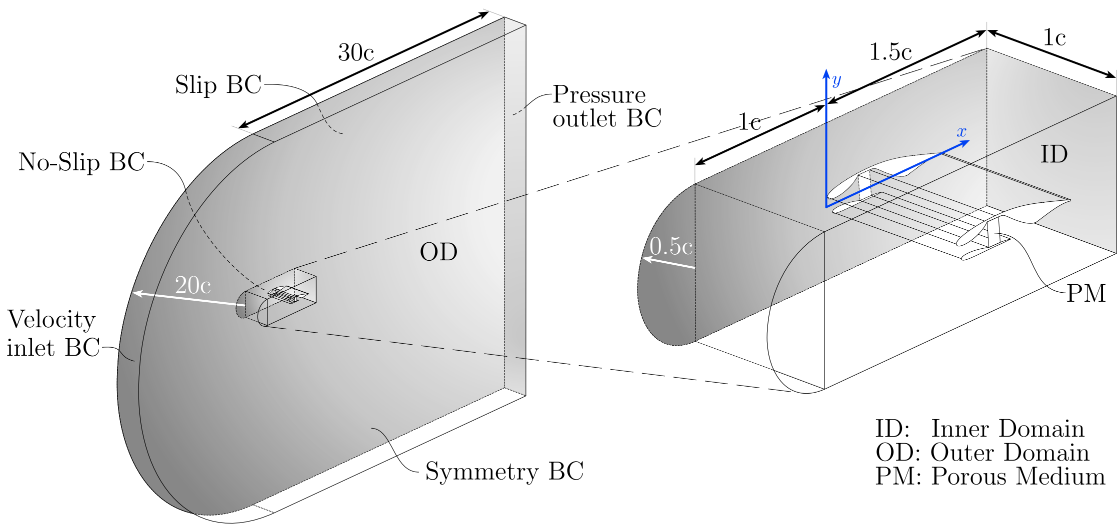

Figure 3.6: 3D computational domain and boundary conditions for the nacelle/ducted-wing configuration with the heat exchanger modeled as a porous medium.

3.6. GRID SETUP AND DEPENDENCY STUDY

All simulations are conducted using the unstructured solver, ANSYS® Fluent, with the hybrid mesh generated in Cadence® Fidelity Pointwise. In the regions shown in the computational domain in Figure 3.4 and Figure 3.6, the outer domain (OD) and porous medium (PM) are meshed with structured elements, while the inner domain (ID) uses an unstructured mesh due to the intricate ducted airfoil geometry. The T-Rex anisotropic tetrahedral extrusion method was used in the near-wall regions to generate hexahedral/prismatic layers, sufficient to resolve the boundary layer down to the viscous sublayer with $y^+ \leq 1$. The dimensionless wall distance y^+, is a parameter that quantifies the distance from the wall in terms of viscous length scales, as defined in Equation 3.9.

$$y^+ = \frac{y u_\tau}{\nu} \tag{3.9}$$

where y is the normal distance from the wall, ν is the kinematic viscosity, and u_τ is the friction velocity, which is computed based on the local wall shear stress τ_w and density ρ, given as:

$$u_\tau = \sqrt{\frac{\tau_w}{\rho}} \tag{3.10}$$

The wall shear stress, as shown in Equation 3.11, can be determined using the skin friction coefficient C_f, which is empirically derived based on Prandtl's one-seventh power law [42], as given in Equation 3.12:

$$\tau_w = \frac{1}{2}\rho V_\infty^2 C_f \tag{3.11}$$

$$C_f = 0.027 Re_x^{-\frac{1}{7}} \tag{3.12}$$

This empirical relation provides an estimate for the wall shear stress in a turbulent boundary layer. However, its accuracy may vary depending on flow conditions and Reynolds number based on the distance x from the leading-edge, as defined in Equation 3.13.

$$Re_x = \frac{\rho V x}{\mu} \tag{3.13}$$

The first-layer cell thickness of the hexahedral/prismatic layer is estimated by rearranging Equation 3.9, and an appropriate growth rate is applied to define the full prismatic layer. The wall-resolving approach accurately capture near-wall phenomena, including flow separation, adverse pressure gradients, and the transition from laminar to turbulent flow. The prism layer is followed by tetrahedral elements, which transition to hexahedral elements in the outer domain (OD). The mesh density across the entire domain is controlled by adjusting the connector dimensions and spacing, refining the near-wall regions for all no-slip boundaries, setting the first-layer thickness of the prism layers, and controlling the associated growth rate. An example of the generated mesh is shown in Section B.1.

The mesh generation process for the ducted airfoil is shown in the flowchart provided in Figure 3.7. A Pointwise Glyph script was created to automate the mesh generation process. In each script call, the structured OD was loaded and used as a reference domain since it remains unchanged. Subsequently, the generated ducted airfoil geometries were automatically meshed upon being imported into the ID for each case. Additionally, the script assigns the appropriate volume and boundary conditions, as discussed in Section 3.5, before exporting the grid. Furthermore, the script is executed through a batch file to automate the mesh generation process for the multiple configurations of the DoE test matrix efficiently.

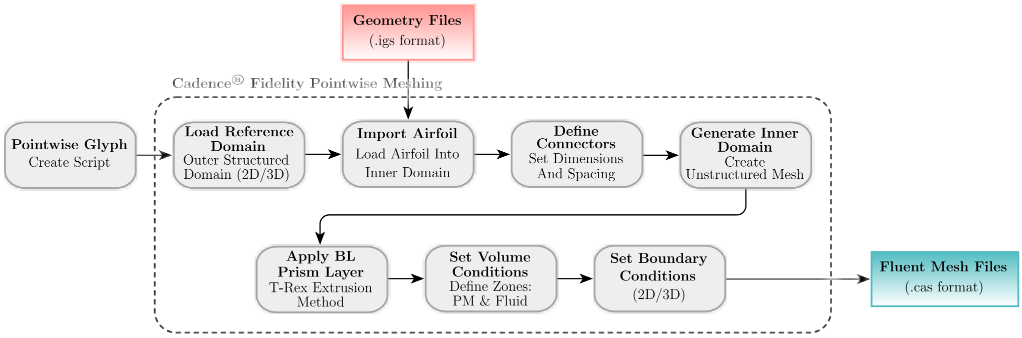

Figure 3.7: Mesh generation flowchart.

In CFD, simulation accuracy is inherently affected by various error sources, each originating from different stages of the numerical modeling process. Modeling errors originates from simplifications in the governing equations, such as the RANS formulation, approximations in turbulence models like the k-ω SST model, and assumptions imposed by artificial boundary conditions, all of which inherently limit the fidelity of physical representation. The extent of modeling errors is assessed in Section 3.7, where airfoil validation is performed by comparing CFD estimated aerodynamic coefficients with experimental data. Iterative errors originate from solving discretized equations through numerical methods that terminate after finite iterations, resulting in a residual imbalance between the computed and exact discrete solutions. In this study, iteration error is controlled by setting the solver residual convergence criteria to 10^{-5}, ensuring it remains small compared to other errors. Round-off errors, caused by finite-precision arithmetic, are similarly small due to the use of double-precision computations and are typically overshadowed by larger error sources. Among these, spatial discretization error is largest, as it results from approximating continuous flow quantities–velocity, pressure, and temperature–across discrete grid cells, introducing numerical diffusion via interpolation of gradients and fluxes. Quantifying and mitigating this error is critical to ensuring result reliability, particularly in resolving fine-scale flow phenomena such as boundary layers, wake regions, and flow separation. This error can be reduced through finer, high-quality meshes that better resolve steep velocity and pressure gradients, thereby improving the accuracy of aerodynamic force predictions.

To assess discretization error, a grid dependency study was conducted using a systematic grid refinement approach. The computational grid was refined with at least five different levels of spatial resolution. For 2D simulations, the connectors in Cadence® Fidelity Pointwise were refined using a refinement ratio of $\sqrt{2}$, whereas for 3D simulations, a refinement ratio of $\sqrt[3]{2}$ was applied. As previously indicated, to accurately capture boundary layer effects, the mesh was refined to resolve the viscous sublayer, maintaining $y^+ \leq 1$, as required for the SST k-ω turbulence model in a fully resolved approach. The prism layer growth rate was adjusted accordingly to maintain a constant first-layer thickness, ensuring a consistent near-wall resolution across all grid levels.

The selected quantities for this study are the lift and drag coefficients at representative cruise and climb conditions. To estimate the spatial discretization error, the least-squares formulation of the grid convergence index developed by Eça and Hoekstra [46] was applied, assuming that iterative and round-off errors are negligible. This method was selected to address the scatter observed in computed lift and drag coefficients, particularly at higher angles of attack where complex flow phenomena like unsteady flow separation occur. Additionally, the use of a hybrid mesh in the inner domain introduces variability in the grid resolution. The least-squares approach accounts for this variability, providing a robust estimation of discretization error and ensuring reliable uncertainty quantification despite the presence of scatter [47].

Using the approach described by Stokkermans [48] and Eça and Hoekstra [46], the error estimate is based on Richardson extrapolation and is obtained using Equation 3.14.

$$\delta_{RE} = \phi_i - \phi_0 = \alpha h_i^p \tag{3.14}$$

Here, ϕ represents the numerical solution of the selected quantity, α is a constant coefficient, h_i denotes the average cell size of grid i, and p is the observed order of convergence [46]. To estimate the error, ϕ_0, α, and p are determined using Equation 3.15, which is a least-squares minimization function, where n_g represents the number of grids.

$$S(\phi_0, \alpha, p) = \sqrt{\sum_{i=1}^{n_g} \left(\phi_i - (\phi_0 + \alpha h_i^p)\right)^2} \tag{3.15}$$

Moreover, the standard deviation of the fit is calculated using Equation 3.16, which requires the number of grids n_g to be at least four. The equations for the theoretical order of convergence ($p = 2$) used to compute δ_{RE}^* and standard deviation U_s^* are detailed by Eça and Hoekstra [46].

$$U_s = \sqrt{\frac{\sum_{i=1}^{n_g} \left(\phi_i - (\phi_0 + \alpha h_i^p)\right)^2}{n_g - 3}} \tag{3.16}$$

In cases where the data does not exhibit monotonic convergence, alternative uncertainty quantification is used, using the maximum difference between all available solutions, ΔM [46]. The maximum difference based on selected grids n_{sel}, as defined by Stokkermans [48] and shown in Equation 3.17, is applied by assigning more weight to finer grids, ensuring that the uncertainty calculation reflects the most reliable results while minimizing the influence of less accurate grids. The discretization uncertainty U_ϕ, determined based on the observed order of convergence p, can be calculated using Equation 3.18 [46, 48].

$$\Delta M = \max\left(|\phi_i - \phi_j|\right), \quad \text{with } 1 \le i \le n_{sel}, 1 \le j \le n_{sel} \tag{3.17}$$

$$U_\phi = \begin{cases} \min\left(1.25\delta_{RE} + U_s, 1.25\Delta_M\right), & 0 < p < 0.95, \\ 1.25\delta_{RE} + U_s, & 0.95 \le p < 2.05, \\ \max\left(1.25\delta_{RE}^* + U_s^*, 1.25\Delta_M\right), & p \ge 2.05, \\ 3\Delta_M, & p < 0 \text{ or oscillatory.} \end{cases} \tag{3.18}$$

The results of the grid dependency study, along with the estimated discretization uncertainty, are provided in the following chapters for each simulation to assess the consistency and reliability of the computed quantities. Additionally, the grid size and refinement ratios (h_i/h_1) are provided, where h_i represents the average cell size of grid i, and h_1 corresponds to the finest grid [48].

3.7. VALIDATION OF RANS SIMULATION SET-UP

The MS(1)-0317 medium-speed airfoil is used as a validation case to ensure the simulation setup accurately predicts aerodynamic performance metrics, including lift, drag, and pressure distributions, for the purposes of this research. Furthermore, this airfoil serves as the baseline geometry for configurations involving ram-air ducts housing heat exchangers. The process includes an analysis of the experimental flow conditions and solver set-up, a grid dependency study, and a comparison of computational results against experimental data. Together, these steps confirm the accuracy and reliability of the simulation set-up implemented in ANSYS® Fluent.

3.7.1. AIRFOIL PROPERTIES AND RELEVANCE

The MS(1)-0317 airfoil investigated by McGhee and Beasley [49], shown in Figure 3.8, is a 17%-thick airfoil developed by NASA to meet the aerodynamic requirements of general aviation aircraft operating in the medium-speed regime. Its thick profile makes it an ideal choice for the wing-integrated ram-air duct configurations examined in this study. The MS(1)-0317 airfoil was tested experimentally at chord Reynolds numbers ranging from 2×10^6 to 12×10^6 and Mach numbers between 0.10 and 0.32 in the NASA Langley Low-Turbulence Pressure Tunnel. Although these speeds are lower than the typical cruise Mach numbers observed in turboprop aircraft such as the ATR-72 or Dash 8 (Mach 0.45-0.55), this study focuses on examining the aerodynamic effects of wing-integrated ducts without focusing on a particular aircraft type.

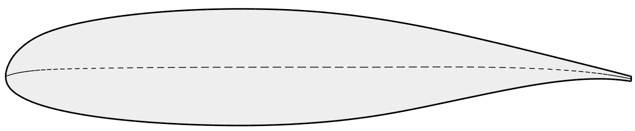

Figure 3.8: Medium-speed NASA airfoil MS(1)-0317 profile [49].

3.7.2. FLOW CONDITIONS AND SOLVER SET-UP

For simulations to match experimental data, it is important to accurately replicate the boundary and flow conditions, including key similarity parameters such as the Reynolds number and Mach number. In this study, a chord-based Reynolds number of 6×10^6 is selected based on the reference NASA experiment by McGhee and Beasley [49], which serves as the validation case. The corresponding Mach number, as used in the NASA experiment, is 0.15, indicating low subsonic flow. The wind tunnel model tested by NASA had an airfoil chord length of 0.61 m [49].

The speed of sound ($a = \sqrt{\gamma R T}$) is calculated using the specific heat ratio γ, the universal gas constant R, and an assumed sea-level temperature of 25 °C. Based on this, the inlet velocity corresponding to a Mach number of 0.15 is calculated as $51.922\,\mathrm{m\,s^{-1}}$. With the Mach number matching the experimental conditions, the inlet velocity is used to compute the Reynolds number, where the characteristic length is set to $1c$ in the simulations.

Achieving a Reynolds number of 6×10^6 requires a specific combination of air density ρ

and dynamic viscosity μ. In the pressurized wind tunnel, it is assumed that the density was adjusted by varying the pressure, as dictated by the ideal gas law, while keeping the temperature constant, which in turn kept the dynamic viscosity unchanged. However, the exact method used by NASA to achieve the target flow conditions is not explicitly documented.

In addition to these parameters, accurately specifying turbulent quantities is important to fully match with the experiment inlet conditions. These quantities, including turbulence intensity and turbulence length scale, govern boundary layer development and flow behavior in the vicinity of the airfoil, influencing aerodynamic performance predictions. The turbulence intensity in the NASA Langley Low-Turbulence Pressure Tunnel ranges from 0.02% to 0.08% [50], with the upper limit used in this study. Furthermore, the turbulence length scale was set to 0.01 at the inlet. While specific turbulence length scale data is unavailable, this value was chosen based on typical estimates for low-turbulence environments, assuming a small fraction of the airfoil chord length.

For this validation study, second-order spatial discretization schemes are applied to all flow variables to improve numerical resolution and reduce truncation errors. The Coupled algorithm is employed for pressure-velocity coupling. Furthermore, the k-ω SST model with the γ-Re_θ transition model is used for turbulence modeling due to its ability to predict natural transition to turbulence accurately. No forced transition was implemented using a User-Defined Function (UDF), as the experimental data provides results for natural transition. However, specific details regarding the boundary layer state, such as the exact transition location, are not documented in the available experimental references. Instead, the transition model predicts the onset of turbulence based on the local flow conditions, ensuring a physically consistent approach.

3.7.3. GRID DEPENDENCY

For the validation of the airfoil's aerodynamic performance, Table 3.2 shows the grid resolutions analyzed in the grid dependency study, with grid 1 selected for its highest accuracy. Table 3.3 provides the sectional lift and drag coefficients (C_l and C_d) at 2° and 10° angles of attack for various grids, along with the discretization error for grid 1, the estimated exact solution, the observed order of convergence, and the standard deviations of the fits. Monotonic convergence was observed in all cases, with the observed order of convergence p exceeding the theoretical order of $p = 2$ in every instance. As a result, the theoretical order was applied to calculate the discretization error, as shown in Equation 3.18. A good fit was achieved for the lift coefficient C_l at 2° and 10° angles of attack, as the standard deviation of the observed order closely aligns with that of the theoretical order. Additionally, the estimated discretization errors for grid 1, at 0.55% and 0.84% for 2° and 10° angles of attack respectively, indicate that the solution has reached a satisfactory level of convergence. For the drag coefficient C_d, the discretization errors for grid 1 are notably higher, at 3.19% and 3.92% for 2° and 10° angles of attack, respectively. This is likely due to the increased sensitivity of drag calculations to numerical diffusion, particularly in regions with high gradients, such as the boundary layer and wake. Drag, being a second-order effect of pressure and shear stress, is more sensitive to inaccuracies in capturing flow gradients compared to lift, which is predominantly governed by pressure differences. The higher uncertainty in drag highlights the need of finer grids to minimize numerical diffusion and improve the accuracy of drag predictions. The results indicate that the solution achieved with grid 1 is adequately converged, making it suitable for use in the remainder of this study.

Grid	Number of cells	h_i/h_1
6	79748	4.15
5	149422	3.03
4	278979	2.22
3	487407	1.68
2	799146	1.31
1	1374684	1.00

Table 3.2: Grid resolutions of the computational domain for RANS simulation setup validation.

ϕ_i	$C_l(\alpha=2°)$	$C_d(\alpha=2°)$	$C_l(\alpha=10°)$	$C_d(\alpha=10°)$
ϕ_6	0.6523	0.0058	1.5959	0.0110
ϕ_5	0.6349	0.0071	1.5391	0.0136
ϕ_4	0.6224	0.0081	1.5043	0.0150
ϕ_3	0.6240	0.0080	1.5144	0.0148
ϕ_2	0.6239	0.0080	1.5120	0.0147
ϕ_1	0.6233	0.0079	1.5109	0.0146
p	3.66	3.73	4.33	4.85
U_s(%)	0.14	0.95	0.19	0.88
U_s^*(%)	0.20	1.27	0.29	1.48
$\lvert U_{\phi_1}\rvert$(%)	0.55	3.19	0.84	3.92

Table 3.3: Grid dependency study for RANS simulation setup validation.

3.7.4. COMPARISON OF COMPUTATIONAL AND EXPERIMENTAL DATA

To establish confidence in the numerical setup and validate its capability to accurately predict aerodynamic performance, the aerodynamic coefficients, and pressure distribution are compared with experimental data. Figure 3.9 presents a comparison of the lift and drag coefficients as a function of the angle of attack. The presented data, both computational and experimental, corresponds to natural transition conditions. For completeness, additional turbulence models, alongside the k-ω SST model with the γ-Re_θ transition model, are tested to provide insights into the sensitivity of the results to turbulence model selection. Furthermore, the experimental data includes a reported error margin of 2% because wind tunnel boundary corrections were not applied in the original study [49]. Since the CFD simulations do not include wind tunnel walls, no additional corrections are required for the numerical results, ensuring direct comparability with the experimental data.

As shown in Figure 3.9a, the computed lift coefficients demonstrate good agreement with the experimental data. The curves follow the expected trend, with C_l increasing linearly at lower angles of attack and beginning to level off as the stall angle is approached. The difference between the models is negligible up to approximately 10°, confirming that the numerical setup accurately captures the aerodynamic performance in the linear region. Moreover, as shown in Figure 3.9b, the computed drag coefficients align well with the experimental data only when using transition turbulence models. The observed trends confirm that the pressure and viscous forces are well resolved by the numerical setup.

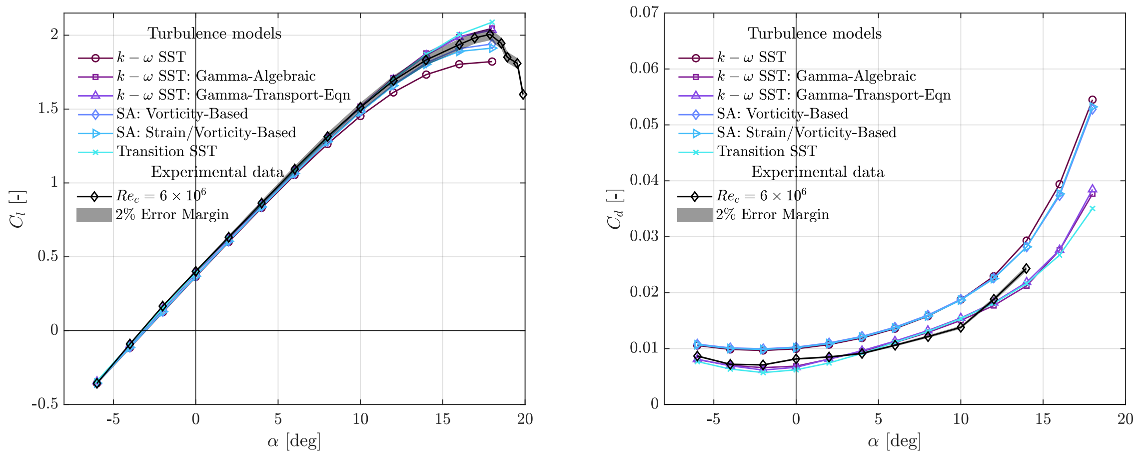

(a) Lift coefficient (C_l)

(b) Drag coefficient (C_d)

Figure 3.9: Comparison of computed lift and drag coefficients using different turbulence models against experimental data at $Re_c = 6 \times 10^6$.

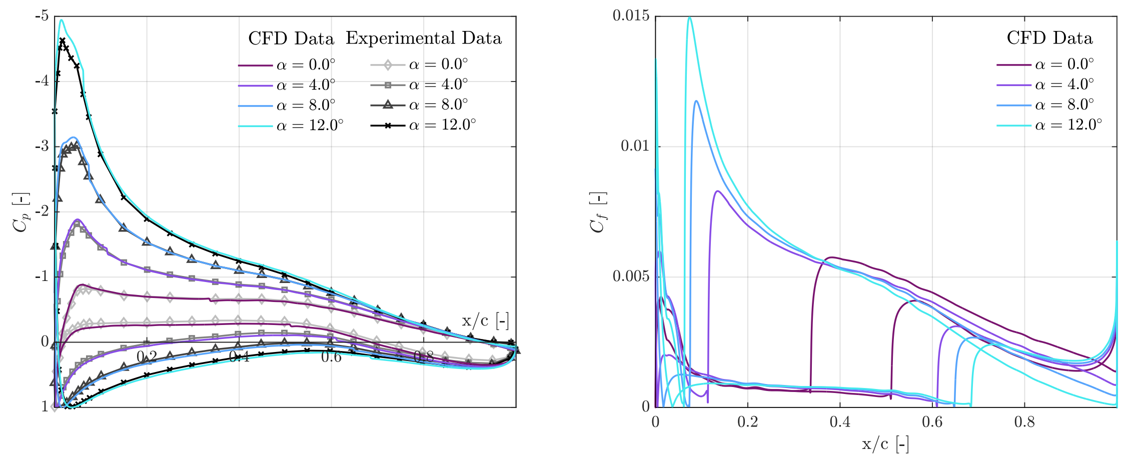

(a) Pressure coefficient distribution (C_p)

(b) Skin friction coefficient distribution (C_f)

Figure 3.10: Comparison of the pressure coefficient distribution, against experimental data, and the shear distribution in terms of skin friction coefficient at $Re_c = 6 \times 10^6$.

In Figure 3.10, the pressure distribution is compared with experimental data, alongside the skin friction coefficient. The experimental data for the pressure distribution is for forced transition, with no data available under natural transition. Furthermore, no experimental data is available for the skin friction coefficient. The computed results were obtained using the k-ω SST turbulence model combined with the γ-Re_θ transition model, with the intermittency γ set to 1, representing fully turbulent flow. However, even with γ is 1, bypassing natural transition prediction, local flow conditions–such as near the stagnation point–can still show laminar-like characteristics due to minimal turbulence production. Additionally, the transition model continues to solve the governing equations for intermittency and the transition onset Reynolds number, allowing subtle transitional effects to persist. As seen in Figure 3.10a, the pressure distribution show good agreement with the experimental data for the available angles of attack (0°, 4°, 8°, and 12°), as these were the only angles provided in the experimental dataset. The trends at lower angles of attack, including the suction peak near the leading-edge and the gradual adverse pressure gradients, are well captured. However, at higher angles of attack, discrepancies between the results are observed in the suction peaks near the leading-edge while general trends are captured. Moreover, the skin friction coefficient, as illustrated in Figure 3.10b, clearly indicates the transition from laminar to turbulent flow on the airfoil's surface. On the upper surface, this transition shifts forward with increasing angle of attack, while on the lower surface, it shifts backward. Since experimental transition locations are not available, a direct comparison cannot be made. However, differences in the transition process between CFD and wind tunnel testing are expected due to variations in surface roughness, freestream turbulence, and other environmental factors. Despite this, the overall agreement in pressure and shear distributions confirms that key flow physics, such as boundary layer behavior, pressure gradients, and wall shear stresses, are well captured, further supporting the validity of the numerical setup.

3.8. THERMAL AND PRESSURE-DROP ANALYSIS OF THE HEAT EXCHANGER

This section describes the methodology for analyzing the thermohydraulic performance of the heat exchanger, modeled as a porous medium in the CFD setup, to effectively predict the aerothermal behavior of the wing-integrated duct. The focus is on developing a low-order heat exchanger model that evaluates the performance of a crossflow, unmixed-unmixed configuration, designed to dissipate heat generated by hydrogen fuel-cell systems. The objective is to validate the heat exchanger's thermal performance and pressure drop behavior under sea-level static conditions, which represent the worst-case scenario for cooling due to high ambient temperatures. Furthermore, the preliminary sizing of the heat exchanger is performed to ensure it fits within the available space inside the wing. The analysis includes iterative calculations based on the ε-NTU method for thermal performance and pressure drop modeling using the Darcy-Forchheimer approach. The heat source is implemented as an energy source term using a UDF to evaluate the thermal performance of the heat exchanger. The pressure-drop characteristics are modeled directly using ANSYS® Fluent's built-in porous media functionality, which incorporates a momentum source term into the governing equations.

3.8.1. HEAT EXCHANGER CONFIGURATION AND ASSUMPTIONS

The heat exchanger considered in this study is a crossflow configuration with both fluids unmixed, as shown in Figure 3.11. This arrangement prevents cross-mixing of fluid streams, ensuring consistent thermal performance and a well-defined temperature distribution. The effectiveness of such a configuration is determined using the ε-NTU method, as closed-form analytical solutions are unavailable for this flow arrangement [51, 52]. While the effectiveness (ε) is influenced by input conditions (e.g., mass flow rates and temperatures), the relationship between ε and NTU is defined by the specific flow arrangement and mixing conditions. Moreover, the chosen heat exchanger topology is particularly suitable for compact applications, such as wing-integrated ducts, due to its ability to balance high heat transfer rates and moderate pressure drops within limited spatial constraints. While crossflow configurations are not the most compact in terms of flow arrangement, they are often preferred due to their ease of manufacturing and integration into such systems.

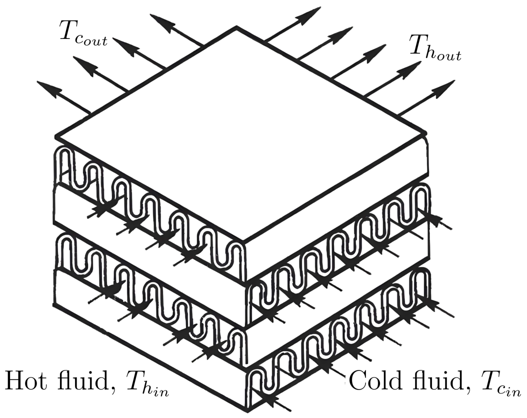

Figure 3.11: Crossflow heat exchanger configuration with both fluids unmixed, (adapted from [51]).

According to Sain *et al.* [3], the cooling power required for the fuel-cell stacks of LTPEM-FCs is approximately 560 kW. In this study, a single heat exchanger is analyzed, designed to handle half of the total cooling load 280 kW, as part of a simplified approach. This assumption reflects the focus on a single duct in a two-dimensional setup, while acknowledging that the complete TMS would involve a bi-duct configuration. The thermal performance and pressure-drop characteristics are analyzed under hot day sea-level static conditions, representing the worst-case scenario for cooling efficiency due to elevated ambient temperatures.

The preferred coolant is a 50-50 ethylene glycol-water mixture, chosen for its favorable thermal properties and low freezing point, making it well-suited to meet the cold-start requirements of the LTPEM fuel cell stacks [3, 53]. Moreover, the specific heat values are assumed constant, with 3410 $\mathrm{J\,kg^{-1}\,K^{-1}}$ for the coolant and 1006.5 $\mathrm{J\,kg^{-1}\,K^{-1}}$ for air. The cooling air flows in a crossflow configuration with the coolant stream, entering the heat exchanger at 27.5 °C and dissipating the heat generated by the fuel-cell stacks. Additionally, the coolant enters the heat exchanger at a temperature of 80 °C. Moreover, both air and coolant are treated as incompressible fluids. A constant heat transfer coefficient U of 130 $\mathrm{W\,m^{-2}\,K^{-1}}$ [3] is assumed across the heat exchanger, which ensures uniform thermal performance during steady-state operation. The compactness of the heat exchanger, defined as the ratio of heat transfer surface area to total volume, is assessed to verify that the design fits within the available wing space while maintaining the required cooling and aerodynamic performance.

3.8.2. PRESSURE-DROP PERFORMANCE CALCULATIONS

The pressure-drop performance of the heat exchanger was analyzed using the porous media modeling capabilities available in ANSYS® Fluent. This approach models the heat exchanger as a porous zone, eliminating the need for detailed flow passage meshing, which would otherwise require extremely fine meshes, reduce cell quality, and substantially increase computational cost. The heat exchanger is modeled as an anisotropic porous zone and are defined within the computational domain for the two-dimensional and three-dimensional analyses as illustrated in Figure 3.4 and Figure 3.6, respectively. Three heat exchangers, each with a different porosity (ε), are tested to analyze the flow resistance they induce within the duct and its resulting impact on the aerodynamic performance of the wing. Porosity, according to Beltrame *et al.* [54], is the fraction of the total volume occupied by voids through which the flow passes, and is strongly related to the heat exchanger core geometry. Due to the reduced flow area in the heat exchanger core, the fluid within the porous zone is forced to accelerate by a factor of $1/\varepsilon$ [54], which directly affects the pressure-drop and thermal performance characteristics.

$$S_i = -\left(\sum_{j=1}^{3} D_{ij}\mu v_j + \sum_{j=1}^{3} C_{ij}\frac{1}{2}\rho|v|v_j\right) \tag{3.19}$$

In the porous medium, a momentum sink is added as a source term to the governing momentum equations to account for the dissipation of kinetic energy from the flow, resulting in a pressure drop as the flow passes through the heat exchanger core. This source term is modeled according to Equation 3.19, which represents the Darcy-Forchheimer quadratic drag law [55]. It consists of two components: the first term accounts for viscous losses (Darcy term), while the second term represents inertial losses (Forchheimer term) [42, 44]. Where S_i is the source term for the i-th component of the momentum equation [44], μ is the dynamic viscosity, ρ is the density, $|v|$ is the magnitude of the velocity [44], and D_{ij} and C_{ij} are prescribed matrices representing the viscous resistance factor and inertial resistance factor in an anisotropic porous medium, respectively [56]. The pressure drop is directly proportional to the fluid velocity in the viscous loss term and to the square of the velocity in the inertial loss term. As flow speeds increase, the inertial term becomes the dominant contributor to the overall pressure drop.

3

In an anisotropic homogeneous porous medium, higher resistance is applied perpendicular to the primary flow direction, forcing the flow to follow it. The D and C matrices are diagonal, containing $1/\kappa$ and C_2 on the diagonal, respectively, with all off-diagonal elements being zero, where κ represents the permeability and C_2 is the inertial resistance factor [44]. The permeability κ, quantifies how easily fluid can flow through the heat exchanger core, and is influenced by factors such as porosity and the geometry of the core, including void size, shape, and connectivity. Moreover, the relationship between porosity and permeability is nonlinear and depends based on the specific material properties and the core's geometric topology. As such, the momentum source term simplifies to the following equation:

$$S_i = -\left(\frac{\mu}{\kappa}v_i + C_2\frac{1}{2}\rho|v|v_i\right) \tag{3.20}$$

In ANSYS® Fluent, the source term is applied locally to each cell (or control volume) within the porous zone. Fluent computes the pressure gradient associated with the source term for each cell and progressively calculates the resulting pressure drop across the porous medium. Since Fluent does not know the thickness of the heat exchanger a priori, the coefficients $1/\kappa$ and C_2 must include the thickness contribution to accurately represent the pressure drop. The source term added to the governing momentum equations are expressed in units of force per unit volume (N/m^3). Furthermore, the porous medium defined in the computational domain often differs from the actual physical size of the heat exchanger. As a result, the coefficients must be adjusted to account for the actual thickness of the heat exchanger, ensuring that the pressure drop computed in the simulation accurately represents the real system. As a result, Equation 3.20 is modified to account for the thickness of the porous medium:

$$\frac{\Delta P}{L} = \frac{\mu}{\kappa}v + C_2\frac{1}{2}\rho v^2 \tag{3.21}$$

Furthermore, the superficial velocity formulation is applied to the porous medium zone, where the velocity is calculated based on the volumetric flow rate averaged over the entire porous region, including the solid matrix [44]. This formulation maintains continuity of velocity vectors across the porous interface and corresponds to the empirical resistance coefficients of the Darcy-Forchheimer model, as these coefficients are derived from bulk resistance measurements, which characterize the overall flow resistance of the heat exchanger rather than resolving its detailed internal structure. Therefore, this formulation does not account for the porosity in the transport equations, which can lead to inaccuracies when velocity gradients or local flow features are important. The relationship between the superficial velocity and the physical velocity is given by the following equation:

$$\mathbf{u}_{\text{superficial}} = \varepsilon \cdot \mathbf{u}_{\text{physical}} \tag{3.22}$$

where ε is the porosity of the medium, and the physical velocity $\mathbf{u}_{\text{physical}}$ represents the true velocity of the fluid within the voids of the heat exchanger. The physical velocity formulation does account for the porosity in the transport equation, providing a more accurate representation of the local flow behavior inside the porous medium [42].

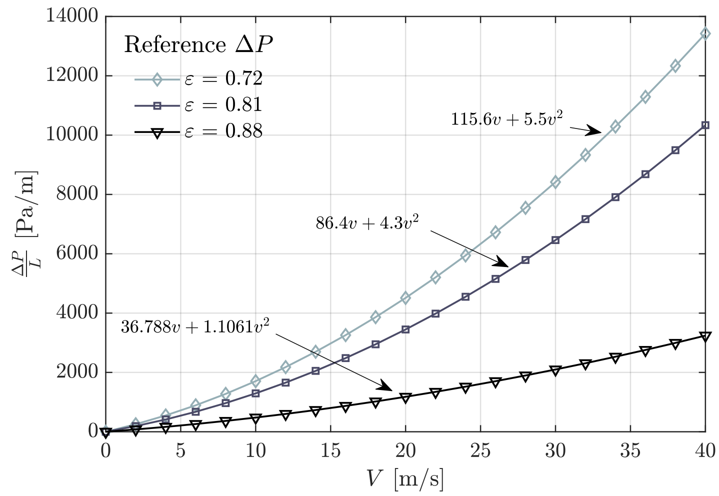

Figure 3.12: Heat exchanger pressure-drop as a function of inlet velocity. The curve fits illustrate the effect of porosity, with higher pressure drops observed for lower porosities due to increased flow resistance.

Three heat exchangers with different porosities are used to investigate how flow resistance influences wing aerodynamics. The pressure drop across a heat exchanger is often provided in literature or experimental data as a second-degree polynomial, as expressed in Equation 3.21. In Figure 3.12, the pressure gradient is plotted against the velocity at the heat exchanger inlet for three different porosity (ε). The highest porosity is derived from Musto *et al.* [56], which considers an aircraft oil cooler using a porous medium approach. The porosity value of 0.81 was obtained for an offset strip fin heat exchanger by using the *HeXacode* software [54]. For the lowest porosity case, where a higher pressure drop is expected, obtaining real-world data was challenging. Therefore, the viscous and inertial resistance coefficients were adjusted to simulate a higher pressure drop. This porosity was determined through a parametric study in ANSYS® Fluent, where trial-and-error adjustments were made to the porosity until the resulting pressure drop curve closely matched the desired second-degree polynomial behavior. The validation of the porous medium for accurately predicting the pressure-drop characteristics of the different heat exchangers is discussed in Section 3.8.4.

3.8.3. Thermal performance calculations

This study focuses on a sizing problem, aiming to evaluate whether the heat exchanger can fit within the wing's volumetric constraints while satisfying the thermal performance requirements, such as the heat transfer rate and pressure drop required for fuel-cell systems in turboprop aircraft. To estimate the thermal performance of heat exchangers, various approaches exist, with one commonly used method being the ε-NTU (effectiveness-Number of Transfer Units) method. The ε-NTU method simplifies the calculations required to predict the performance of heat exchangers with complex flow arrangements [57]. This method uses three dimensionless parameters to characterize heat transfer per unit surface area, with the results depended by the flow type (e.g., counterflow, parallel flow, crossflow) and geometry (e.g., micro-channel, compact) [57]. These parameters include the heat exchanger effectiveness ε also referred to as the thermal efficiency (Equation 3.28), the number of transfer units (NTU, Equation 3.26), and the heat capacity ratio C^* (Equation 3.25). To compute these parameters, a constant overall heat transfer coefficient (U) is assumed for this study, along with the specific heat values for air and the coolant, as previously mentioned, based on the data reported by Shah and Sekulic [52]. The optimum coolant mass flow rate ($\dot{m}_\mathrm{h}$) and total heat transfer area (A) must be determined to meet the cooling demands. Once the heat transfer area is calculated, it is compared against the available volume within the wing to ensure it fits. The compactness of the heat exchanger varies with porosity, with values of approximately $800\,\mathrm{m^2\,m^{-3}}$ for $\varepsilon = 0.72$, $700\,\mathrm{m^2\,m^{-3}}$ for $\varepsilon = 0.81$, and $600\,\mathrm{m^2\,m^{-3}}$ for $\varepsilon = 0.88$ [52]. Additionally, the outlet temperatures of the cold and hot fluids (T_{c_out}, T_{h_out}) should be of similar magnitude to avoid large temperature gradients that could adversely impact the thermal performance.

The heat transfer scheme for an unmixed-unmixed crossflow heat exchanger integrated within a ducted wing is illustrated in Figure 3.13, where the terminal temperatures of the cold fluid (T_c) are aligned parallel to the freestream, and the terminal temperatures of the hot fluid (T_h) are oriented perpendicular to the incoming flow. The heat transfer rate $\dot{q}$, must satisfy the cooling requirement for the fuel stacks and is directly influenced by the cold mass flow rate, which varies with the porosity of the heat exchanger.

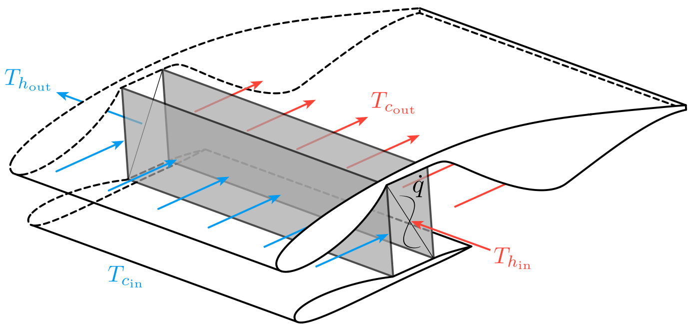

Figure 3.13: Heat transfer scheme of an unmixedunmixed crossflow heat exchanger inside a wing-integrated duct.

The heat exchanger specifications used in these computations are listed in Table 3.4, and for a detailed walkthrough of the computations, see Appendix A. The main steps for evaluating the thermal performance are discussed below. It should be noted that the following methodology for estimating the heat transfer area and hot mass flow rates uses an optimization routine implemented in MATLAB.

Specification	Value	Unit
Heat transfer rate $\dot{q}$	280	kW
Heat transfer coefficient U	130	$\mathrm{W\,m^{-2}\,K^{-1}}$
Temperature air inlet $T_{c_{\text{in}}}$	27.5	°C
Specific heat capacity air $c_{p_{\text{c}}}$	1006.5	$\mathrm{J\,kg^{-1}\,K^{-1}}$
Temperature coolant inlet $T_{h_{\text{in}}}$	80	°C
Specific heat capacity coolant $c_{p_{\text{h}}}$	3410	$\mathrm{J\,kg^{-1}\,K^{-1}}$

Table 3.4: Thermodynamic specifications of the heat exchanger used for sizing calculations.

3

The heat capacity rate ratio is defined as the ratio of the smaller to the larger heat capacity rate of the two fluid streams [52], as expressed in Equation 3.25. The heat capacity rates for the cold and hot fluids are defined in Equation 3.23 and Equation 3.24, respectively. Moreover, the heat capacity rate ratio is an operational parameter, as it depends on the mass flow rates of the cold and hot streams [52], as well as their respective temperatures. In this study, the inlet temperatures and specific heat coefficients are assumed to be constant.

$$C_{\text{air}} = C_c = (\dot{m}c_p)_{\text{air}} \tag{3.23}$$

$$C_{\text{liquid}} = C_h = (\dot{m}c_p)_{\text{liquid}} \tag{3.24}$$

$$C^* = \frac{C_{\text{min}}}{C_{\text{max}}} = \begin{cases} \frac{C_{\text{c}}}{C_{\text{h}}} & \text{for } C_{\text{c}} < C_{\text{h}} \\ \\ \frac{C_{\text{h}}}{C_{\text{c}}} & \text{for } C_{\text{h}} < C_{\text{c}} \end{cases} \tag{3.25}$$

For a constant overall heat transfer coefficient U, the number of transfer units (NTU), based on the smallest heat capacity rate C_{min} [52, 57], is determined using Equation 3.26. This non-dimensional parameter is also known as the heat exchanger size factor [52], as U and C_{min} remain nearly constant and thus changes linearly with the heat transfer area A.

$$\text{NTU} = \frac{UA}{C_{\text{min}}} \tag{3.26}$$

Using the NTU and heat capacity rate ratio C^*, the thermal efficiency (effectiveness) of the heat exchanger, can be determined through the ε-NTU relationship provided in the literature for different types of heat exchangers, as expressed in Equation 3.27 [51]. This equation is for an unmixed-unmixed cross-flow type heat exchanger. Furthermore, as shown in Equation 3.28, the effectiveness is defined as the ratio of the actual heat transfer rate $\dot{q}_{\text{actual}}$, between the hot and cold fluids, to the maximum thermodynamically permitted heat transfer rate, $\dot{q}_{\text{max}}$ [52]. Moreover, a heat exchanger achieves maximum effectiveness when the outlet temperature of the fluid with the smaller heat capacity rate equals the inlet temperature of the fluid with the larger heat capacity rate [52].

$$\varepsilon = 1 - e^{\left(\frac{1}{C^*}\right)(\text{NTU})^{0.22}\left(e^{-C^*(\text{NTU})^{0.78}} - 1\right)} \tag{3.27}$$

$$\varepsilon = \frac{\dot{q}_{\text{actual}}}{\dot{q}_{\text{max}}} \tag{3.28}$$

The maximum possible heat transfer rate, as given by Equation 3.29, is determined by the smallest heat capacity rate C_{min} and the maximum temperature difference between the inlet streams.

$$\dot{q}_{\text{max}} = C_{\text{min}}(T_{h_{in}} - T_{c_{in}}) \tag{3.29}$$

Given the maximum possible heat transfer rate and the effectiveness, Equation 3.28 can be rearranged to determine the actual heat transfer rate $\dot{q}_{\text{actual}}$ of the heat exchanger, which must match the required cooling demand, as shown in Table 3.4. Once the actual heat transfer rate is known, the outlet temperatures for the air and coolant can be calculated using Equation 3.30 and Equation 3.31, respectively.

$$\dot{q}_{\text{actual}} = C_c(T_{c_{\text{out}}} - T_{c_{\text{in}}}) \rightarrow T_{c_{\text{out}}} = T_{c_{\text{in}}} + \frac{\dot{q}_{\text{actual}}}{C_c} \tag{3.30}$$

$$\dot{q}_{\text{actual}} = C_h(T_{h_{\text{in}}} - T_{h_{\text{out}}}) \rightarrow T_{h_{\text{out}}} = T_{h_{\text{in}}} - \frac{\dot{q}_{\text{actual}}}{C_h} \tag{3.31}$$

To simulate the temperature difference over the cold side, the heat transfer rate is implemented as a volumetric heat source term in ANSYS® Fluent to capture the associated thermal effects. The volumetric source term added to the governing energy equation is expressed in units of energy per unit volume (W/m^3). To implement this in the simulation, the heat transfer rate is normalized by the volume of the porous zone within the wing. In ANSYS® Fluent, the source term is applied locally to each cell (or control volume) within the porous zone. Fluent computes the temperature gradient associated with the energy source term for each cell and progressively calculates the resulting heat transfer across the porous medium zone.

Note that assigning a single value for the heat transfer rate in Fluent applies only to the specific design point under consideration. If the velocity through the duct varies, the heat transfer rate and other dependent parameters, such as the cold-side mass flow rate, will also change. To account for this variation, a 6th-degree polynomial fit is implemented in a UDF to represent the heat transfer rate as a function of the duct velocity, effectively modeling it as a variable volumetric heat source. This method allows the heat transfer rate to be represented at different velocities, enabling off-design analyses of the heat exchanger for various flight conditions.

3.8.4. PRESSURE-DROP VALIDATION IN RANS SIMULATION SET-UP

To validate the numerical setup of the porous medium and its ability to predict heat exchanger pressure-drop characteristics in ANSYS® Fluent, computed pressure drops are compared to second-degree polynomial curve fits derived from literature or experimental data. In Figure 3.14, the pressure gradient across the heat exchanger is shown as a function of velocity for three porosities (0.72, 0.81, 0.88). It can be observed that there is overall good agreement between the results, indicating that the porous medium model in Fluent effectively predicts the pressure-drop behavior for the tested heat exchanger configurations. Thus, the aerodynamic force predictions, particularly the drag of the wing-integrated duct, can be reliably estimated using the heat exchanger's pressure-drop and frontal area. However, since ANSYS® Fluent computes volumetric forces in a porous medium zone, it does not account for the contribution of the solid matrix of the heat exchanger. To accurately represent the total force, the computed force should be divided by the porosity to account for the effect of the solid matrix.

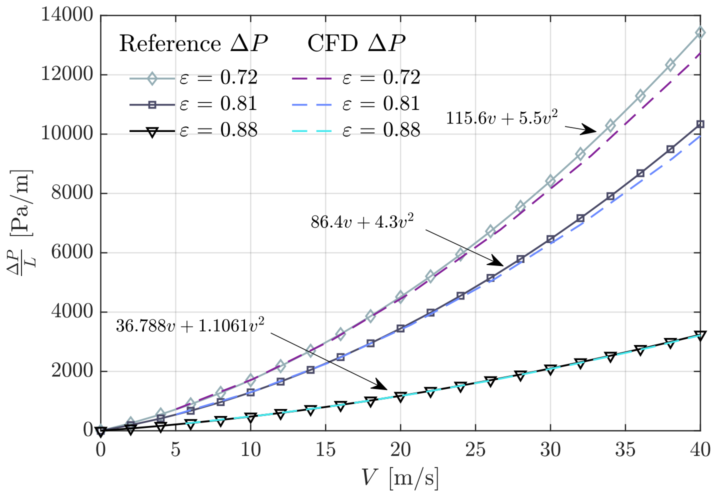

Figure 3.14: Heat exchanger pressure gradient as a function of velocity, validated with CFD data.

Furthermore, at lower velocities, the computed pressure drop closely follows the pressure-drop curves obtained from literature or experimental data for all porosities, indicating that the viscous term (Darcy term) is dominant, as expected in this regime. However, at higher velocities, discrepancies between the computed results and reference data become more noticeable, particularly for lower porosities. The inertial term (Forchheimer term) becomes dominant, as it is proportional to the square of the velocity. The noticeable discrepancy for lower porosities could be attributed to localized effects (e.g. small-scale turbulence, flow separation) within the heat exchanger at higher velocities, which are not fully captured by the Darcy-Forchheimer resistance coefficients, as these represent bulk properties, or the superficial velocity formulation utilized in ANSYS® Fluent. The superficial velocity formulation smooths localized variations by averaging the velocity across the entire volume, including the solid matrix, working well for high porosities but less accurate at low porosities, where discrepancies between physical and averaged velocities cause inaccuracies.

Part III

Results

4

2D Aerodynamic performance

In this chapter, the two-dimensional aerodynamic performance of the wing-integrated duct housing a heat exchanger are discussed. These results serve as a reference for subsequent three-dimensional analyses to investigate the complex flow phenomena at the wing-body junction. Throughout this chapter, RANS CFD results, including the grid convergence study, are systematically presented to thoroughly investigate research question 1, as delineated in Section 1.2:

> **Q1:** *What are the 2D aerodynamic implications of key geometric parameters in a wing-integrated duct under climb and cruise angles of attack?*

Furthermore, the impact of heat exchanger-induced flow restrictions on the aerodynamic performance and flow field of the ducted airfoil are qualitatively presented. This includes analyzing shifts in the stagnation point at the intake, variations in the inlet-velocity ratio, changes in the pressure distribution over the ducted airfoil, and variations in the static pressure and velocity fields. These results contribute to addressing the following research question:

> **Q2:** *How does a wing-integrated duct with restricted flow due to the heat exchanger compare to a clean wing in terms of 2D aerodynamic performance under climb and cruise angles of attack?*

Additionally, in Section 4.3, the heat exchanger thermal effects and its aerodynamic implications are investigated for the most practical ducted wing configurations by enabling the volumetric heat source term in the porous medium zone. Moreover, the feasibility of integrating the heat exchanger within the available wing volume is also assessed as part of this analysis. The effect of the propeller slipstream on the flow field is succinctly discussed in Section 4.4, focusing on how the induced flow field improves the duct mass flow rate and interacts with the duct intake.

4.1. Aerodynamic analysis of the wing-integrated duct through DoE

In this section, RANS CFD simulation results are presented to analyze the aerodynamic performance of four ducted airfoil configurations designed to house heat exchangers. As part of the

DoE, the full factorial design approach, as detailed in Section 3.4, was employed to systematically assess the effects of multiple factors on the response variables by evaluating all possible combinations of their levels. Therefore, the RANS CFD simulations were run on the High Performance Computing (HPC-12) cluster of TU Delft's Flight Performance and Propulsion department, leveraging its computational power to efficiently handle the large-scale parametric study. The CFD simulation flowchart presented in Figure 3.1 is integrated into a higher-level script on the HPC that automates the parametric study workflow.

First, a grid convergence study is conducted, as presented in Section 4.1.1, to determine the aerodynamic performance of the wing-integrated duct with the heat exchanger modeled as a porous medium zone, providing confidence in the chosen grid resolution. Then, Section 4.1.2 presents the main effects of the factors on aerodynamic performance, while Section 4.1.3 focuses on the most significant interactions between the factors, providing deeper insights into the underlying aerodynamic principles. Based on this, the most optimal airfoil shapes, identified from the discrete factor levels in the DoE study, are investigated in Section 4.1.4.

For this analysis, the same MS(1)-0317 medium-speed airfoil, as discussed in Section 3.7, is used as the reference airfoil. The results are shown for a freestream velocity of $V_\infty = 75\,\mathrm{m\,s^{-1}}$, corresponding to a Mach number of $M_\infty \approx 0.22$ and a chord Reynolds number of $Re_c \approx 5\times10^6$, under sea-level static conditions. These conditions were selected to maintain incompressible flow while aligning with potential future wind tunnel validation efforts, as discussed in Chapter 7. The turbulence intensity is set to 0.08%, and the turbulence length scale is prescribed as 0.05 m, corresponding to a fraction of the airfoil chord length. Additionally, the intermittency is set to 1, imposing fully turbulent flow.

4.1.1. Grid convergence

The computational domain for the wing-integrated duct, as presented in Figure 3.4, is assessed for grid convergence to establish confidence in the selected grid. The heat exchanger is modeled as a porous medium zone in the domain, with a momentum sink added as a source term to the governing momentum equations to account for its impact on the entire flow field. Table 4.1 provides an overview of the grid sizes and their respective refinement ratios h_i/h_1 for the six grids used in the DoE study. Furthermore, Table 4.2 presents an overview of the solutions computed on different grids, including the observed order of convergence, the standard deviation of the fitted data, and the discretization error estimate associated with the chosen grid.

Grid	Number of cells	h_i/h_1
6	62081	4.27
5	113856	3.15
4	213478	2.30
3	398277	1.68
2	681502	1.29
1	1131394	1.00

Table 4.1: Grid sizes and refinement ratios for the wing-integrated duct computational domain.

To balance computational cost and solution accuracy, grid 4, a relatively coarse grid was selected as the most practical choice, providing sufficient resolution to accurately capture the relevant flow physics while keeping computational costs manageable. Given the scale of the DoE study, which involves thousands of design variations for each wing-integrated duct configuration, using a superfine grid resolution for all simulations would lead to unfeasible run times. Grid convergence for the wing-integrated duct was examined by analyzing the sectional lift and drag coefficients (C_l and C_d) at representative cruise and climb angles of attack, specifically at 2° and 10°, respectively.

In Table 4.2, all fits shows that the observed order of convergence p, aligns closely with the theoretical value of $p = 2$. Furthermore, the standard deviations of the observed order are consistent with those of the theoretical order, confirming the accuracy of the fits across all cases. While the best fit for $C_{l_{\alpha=2^\circ}}$ and $C_{d_{\alpha=2^\circ}}$ shows monotonic convergence, minor scatter is observed for the finer grids. For converged solutions, a discretization error of 5.4% was estimated for the lift coefficient using this grid, while a significantly higher discretization error of 9.5% was observed for the drag coefficient. Furthermore, $C_{l_{\alpha=10^\circ}}$ shows a monotonic convergence trend with minor scatter, while $C_{d_{\alpha=10^\circ}}$ shows noticeable scatter at finer grid resolutions. At this high angle of attack for converged solutions, a discretization error of 7.2% was estimated for the lift coefficient, while a significantly higher discretization error of 12.6% was observed for the drag coefficient. These results reflect the expected trade-offs when using a coarser grid. The increased discretization error, particularly for drag, is a known limitation of coarser grids, as drag calculations are highly sensitive to numerical diffusion, especially in regions with steep gradients such as the boundary layer and wake. The coarseness of the grid likely affects the accuracy of capturing these flow features, leading to higher errors in drag predictions compared to lift, which is primarily governed by pressure differences. Additionally, unsteady effects, not captured by steady RANS, further contribute to drag discrepancies.

ϕ_i	$C_l(\alpha = 2^\circ)$	$C_d(\alpha = 2^\circ)$	$C_l(\alpha = 10^\circ)$	$C_d(\alpha = 10^\circ)$
ϕ_6	0.8453	0.0389	1.7055	0.0346
ϕ_5	0.8338	0.0406	1.6590	0.0371
ϕ_4	0.8105	0.0437	1.5704	0.0409
ϕ_3	0.7970	0.0449	1.5525	0.0425
ϕ_2	0.7991	0.0447	1.5454	0.0416
ϕ_1	0.7995	0.0446	1.5502	0.0422
p	1.83	2.07	2.09	2.28
$U_s(\%)$	0.30	0.61	0.44	0.84
$U_s^*(\%)$	0.26	0.53	0.38	0.74
$\lvert U_{\phi_4}\rvert(\%)$	5.35	9.48	7.20	12.57
$\lvert U_{\phi_2}\rvert(\%)$	2.05	3.56	2.60	5.95

Table 4.2: Grid dependency study for the wing-integrated duct DoE analysis.

Despite the limitations associated with the grid choice, the convergence trends indicate that grid 4 provides well-converged solutions for the lift coefficient. However, for the drag coefficient, a considerable discretization error must be accounted for in the analysis. Furthermore, for the most optimal airfoil configurations, a finer grid (Grid 2) will be employed to ensure more accurate results, as discussed in Section 4.2. The discretization errors for Grid 2 are also presented in Table 4.2. This approach balances computational costs for the broader study while ensuring higher accuracy for key configurations.

4.1.2. Main effects on aerodynamic performance

The four wing-integrated duct configurations were analyzed to determine their main effects on lift and drag coefficients, as well as duct mass flow rates, at both low and high angles of attack. Main effects were calculated as deviations from the overall mean response, averaged across all simulations and factor levels. For each configuration, the overall mean of each response variable (C_l, C_d, $\dot{m}$) was calculated separately and subtracted from its respective values to obtain the deviations (ΔC_l, ΔC_d, $\Delta \dot{m}$) relative to zero. This normalization simplifies the comparison of configurations and gives insights into the sensitivity of each response variable to changes in the factors, as shown in Figs. 4.1 – 4.6. In configurations *I-A* and *II-A*, the duct outlet is located on the upper surface of the airfoil, with *I-A* positioned immediately aft of the maximum thickness and *II-A* near the trailing-edge. As the upper surface is critical for lift generation, these modifications adversely affect aerodynamic performance but are included for a better understanding of the flow physics. Configurations *I-B* and *II-B* feature the duct outlet on the lower surface of the airfoil, positioned similarly to *I-A* and *II-A*. For each factor, the trends across all response variables are discussed in detail.

Lip radii (R_u, R_l)

For most configurations, variations in the upper and lower lip radii have negligible effects on the duct mass flow rate, as the airflow transitions smoothly into the duct without inducing significant disturbances or pressure losses. However, in configuration *I-A*, where the outlet is positioned on the upper surface aft of the maximum thickness, the mass flow rate increases with larger lip radii. This can be attributed to the outlet's location within the low-pressure region created by supervelocities over the upper surface, which enhances the suction effect and induces additional flow through the duct. Additionally, larger lip radii help prevent flow separation, ensuring a smooth transition of flow into the duct and minimizing internal losses. In contrast, smaller lip radii may induce flow separation due to the thinner lip geometry, resulting in increased internal losses and a reduction in mass flow rate. Furthermore, variations in lip radii have minimal impact on the drag and lift coefficients, as the flow transitions smoothly from the external environment into the duct's gradually expanding diffuser, preserving aerodynamic efficiency. While larger lip radii have only a marginal influence on lift and drag, they provide greater flexibility for the stagnation point location under varying conditions, without significantly altering the overall pressure distribution over the airfoil.

Leading-edge Droop Ratio (LDR)

The leading-edge droop, a high-lift device typically used at high angles of attack, adjusts the airfoil's leading-edge by deflecting it downward, effectively changing the stagnation point location and increasing the local camber while preserving surface continuity. By increasing the camber and achieving better alignment with the stagnation point, the droop improves the pressure distribution by mitigating the suction peak and reducing the steep adverse pressure gradient, thereby delaying flow separation at high angles of attack and increase the maximum lift coefficient. The leading-edge droop ratio (LDR) defines the vertical displacement of the lip, scaled by the gap-to-chord ratio ($\frac{\Delta h}{d/c}$). Based on this ratio, Δh which represents the vertical distance of the upper airfoil leading-edge with respect to the x-axis is determined, as shown in Figure 3.2. Low values of vertical displacement indicate that the upper airfoil leading-edge is close to the x-axis, and vice versa. Note that while the lips are displaced, the duct gap (d/c) remains fixed, as it is a separate variable in this study.

At a low angle of attack, as expected, the LDR show no influence on the duct mass flow rate and only a marginal impact on the lift and drag coefficients for all configurations, as observed in Figs. 4.1c through 4.3c. A high LDR value results in a slight increase in the lift coefficient, attributed to improved alignment with the incoming flow. In contrast, at a high angle of attack, the LDR show a significant effect on the aerodynamic performance of all configurations, as observed in Figs. 4.4c through 4.6c. For a high LDR at this angle of attack, detrimental effects on aerodynamic performance are observed, primarily due to leading-edge separation. Vice-versa, for a low LDR, where the leading-edge is deflected further downward, the lift coefficient is enhanced by reducing the suction peak and adverse pressure gradient. Additionally, the drag coefficient gets reduced since the flow stays attached for longer. Note that the relative changes might be slightly overestimated due to the larger discretization errors associated with the drag coefficient.

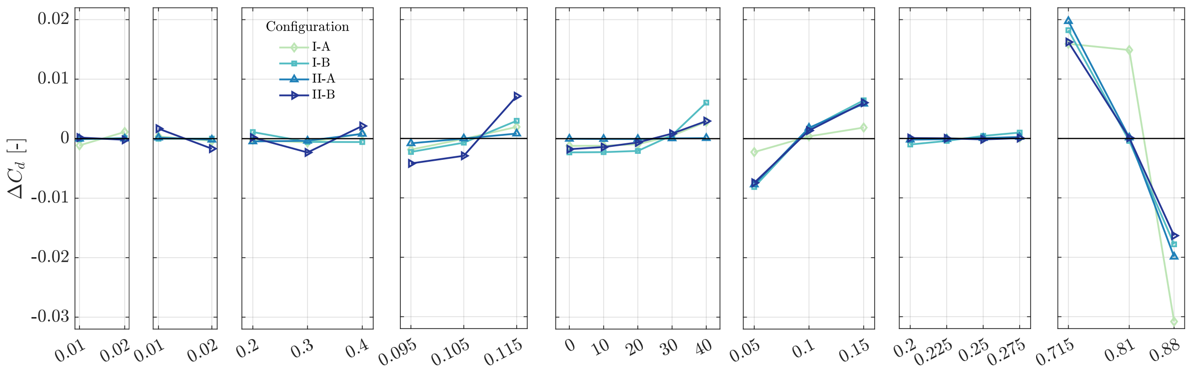

(a) R_u (b) R_l (c) LDR (d) d/c (e) φ (f) t_{hx}/c (g) x_{hx}/c (h) ε

Figure 4.1: Main effects of geometrical factors on the drag coefficient deviation ΔC_d, relative to the mean value, at an angle of attack $\alpha = 2°$ and a chord Reynolds number $Re_c \approx 5 \times 10^6$.

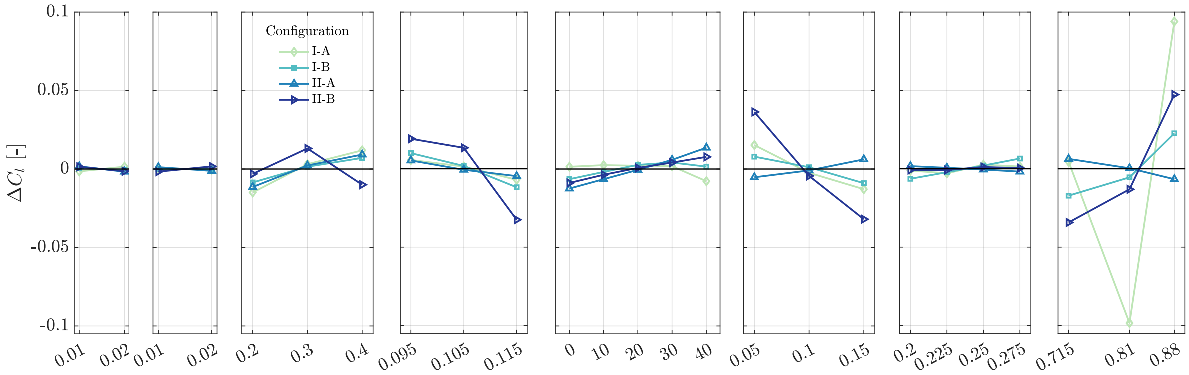

(a) R_u (b) R_l (c) LDR (d) d/c (e) φ (f) t_{hx}/c (g) x_{hx}/c (h) ε

Figure 4.2: Main effects of geometrical factors on the lift coefficient deviation ΔC_l, relative to the mean value, at an angle of attack $\alpha = 2°$ and a chord Reynolds number $Re_c \approx 5 \times 10^6$.

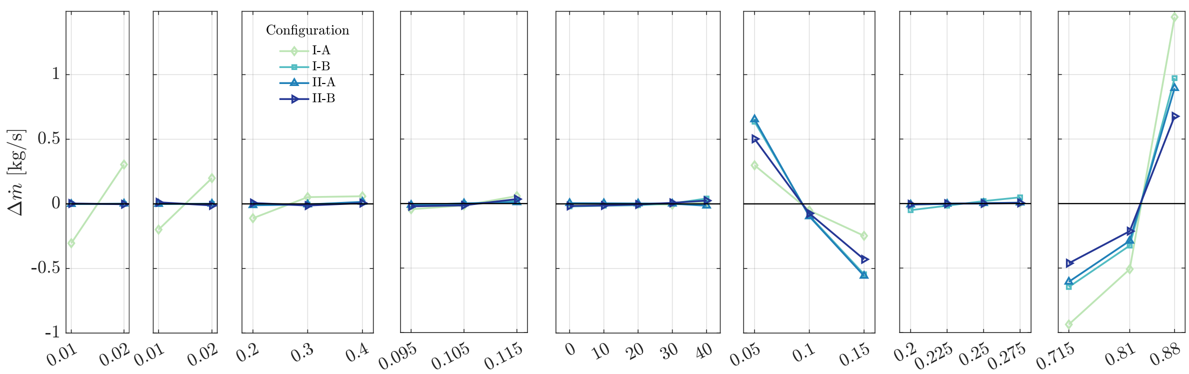

(a) R_u (b) R_l (c) LDR (d) d/c (e) φ (f) t_{hx}/c (g) x_{hx}/c (h) ε

Figure 4.3: Main effects of geometrical factors on the mass flow rate $\Delta \dot{m}$, relative to the mean value, at an angle of attack $\alpha = 2°$ and a chord Reynolds number $Re_c \approx 5 \times 10^6$.

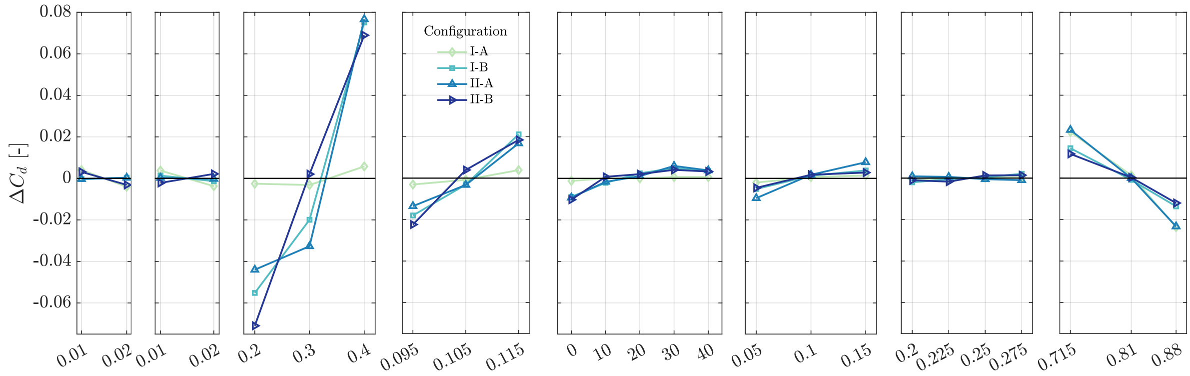

(a) R_u (b) R_l (c) LDR (d) d/c (e) φ (f) t_{hx}/c (g) x_{hx}/c (h) ε

4

Figure 4.4: Main effects of geometrical factors on the drag coefficient deviation ΔC_d, relative to the mean value, at an angle of attack $\alpha = 10°$ and a chord Reynolds number $Re_c \approx 5 \times 10^6$.

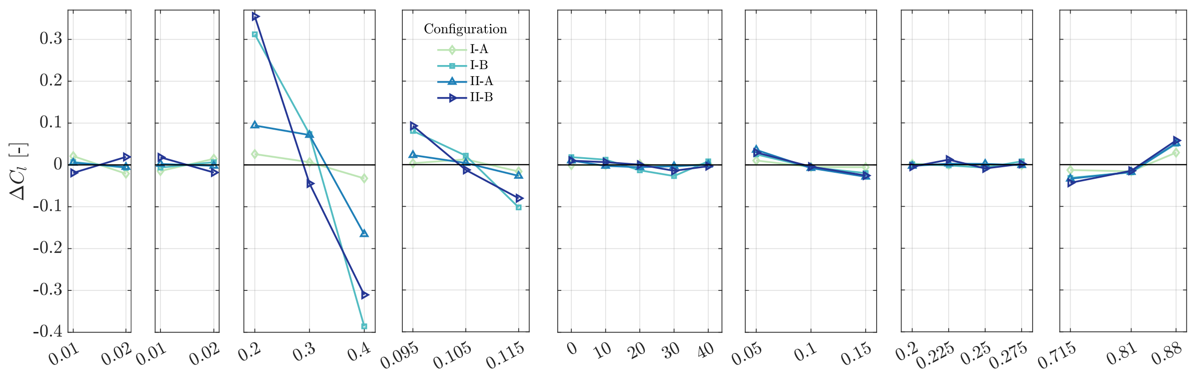

(a) R_u (b) R_l (c) LDR (d) d/c (e) φ (f) t_{hx}/c (g) x_{hx}/c (h) ε

Figure 4.5: Main effects of geometrical factors on the lift coefficient deviation ΔC_l, relative to the mean value, at an angle of attack $\alpha = 10°$ and a chord Reynolds number $Re_c \approx 5 \times 10^6$.

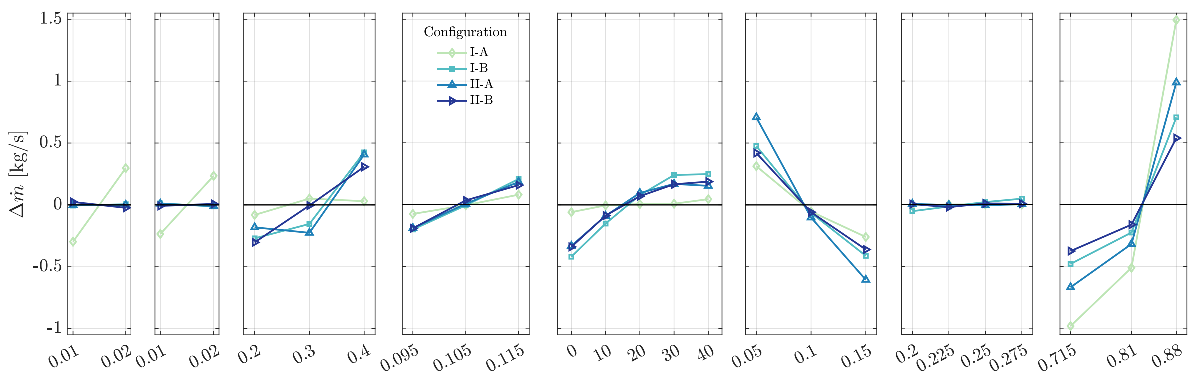

(a) R_u (b) R_l (c) LDR (d) d/c (e) φ (f) t_{hx}/c (g) x_{hx}/c (h) ε

Figure 4.6: Main effects of geometrical factors on the mass flow rate $\Delta \dot{m}$, relative to the mean value, at an angle of attack $\alpha = 10°$ and a chord Reynolds number $Re_c \approx 5 \times 10^6$.

Gap-to-chord ratio (d/c)

The gap of the duct inlet plays a critical role in defining the mass flow rate through the heat exchanger, as it effectively increases the inlet area of the duct allowing for greater airflow. The geometrical constraints ensures that the streamlined diffuser, tangent to the lips, adjusts its internal area slightly in response to the vertical movement of the upper and lower lips. At smaller gap-to-chord ratios, the narrowing of the internal streamlined diffuser induces a compression effect, resulting in a rise in static pressure upstream. The resulting mass flow rate is influenced by this static pressure rise and the location of the outlet, whether positioned on the upper or lower surface of the airfoil. This positioning defines the pressure differential between the duct and the external flow, thereby determining whether more or less mass flow rate can be achieved. At a low angle of attack, as shown in Figure 4.3d, the gap-to-chord ratio levels reveal only a marginal effect on the mass flow rate for all configurations due to the small pressure differentials, with the largest gap producing a slight increase. This is primarily due to the larger inlet area, which allow more airflow into the duct. While the upper surface experiences supervelocities, aft of the maximum thickness the adverse pressure gradient leads to a rise in static pressure, limiting the effectiveness of the low-pressure region in driving additional mass flow. On the lower side of the duct, the static pressure remains higher, further reducing the pressure differential and minimizing the impact of the gap size on the mass flow rate. In contrast, at a high angle of attack, as shown in Figure 4.6d, the mass flow rate is more affected, as indicated by the steeper slope of the trend lines. At this angle, the increased aerodynamic loading enhances the pressure differential across the duct, allowing larger gaps to result in a higher mass flow rate. However, for configuration *I-A*, a slight reduction in mass flow rate is observed, likely caused by flow separation.

As depicted in Figs. 4.1d and 4.4d, the drag coefficient shows an increasing trend with increasing gap-to-chord ratio for both low and high angles of attack. The presence of a duct alters the pressure distribution, creating a region of increased compression ahead of the duct inlet, which in turn leads to higher overall drag. Larger gap-to-chord ratios increase the frontal area and disrupt the streamlined profile of the airfoil, resulting in higher pressure drag. Moreover, it can introduce stronger interactions between internal and external flows, potentially leading to unsteady flow regions and localized disturbances. In contrast, smaller gap-to-chord ratio reduce these disruptions, thereby minimizing drag and maintaining a flow profile closer to that of the clean airfoil.

On the other hand, the lift coefficient shows a decreasing trend with increasing gap-to-chord ratio, as shown in Figs. 4.2d and 4.5d. The presence of a duct modifies the smooth pressure distribution typically observed over a clean airfoil. The stagnation points shifts, and the flow reattaches differently depending on the gap size and location. Larger gap-to-chord ratio cause greater disruption to the pressure distribution on both the upper and lower elements of the ducted wing, with their interaction further reducing the overall lift generated by the ducted airfoil. In contrast, smaller gap-to-chord ratios maintain a pressure distribution closer to that of the clean airfoil, resulting in higher lift.

Stagger angle (φ)

The stagger angle of the lower airfoil, measured relative to the upper airfoil, introduces a chordwise shift that affects aerodynamic performance by modifying the interaction between the two airfoils and optimizing the entry flow alignment with the external airflow. A change in duct staggering has minimal impact on the duct mass flow rate at a low angle of attack, as observed in Figure 4.3e, but a more pronounced effect is present at a high angle of attack, particularly for higher stagger angles, as seen in Figure 4.6e. The minimal impact at a low angle of attack is expected, as changes in stagger angle do not significantly increase the suction peak on the lower duct element. The flow can effectively sustain the adverse pressure gradient, thus it remains attached and undisturbed, thereby maintaining consistent mass flow through the duct. However, as the angle of attack increases, lower stagger angles result in a reduction in mass flow rate due to flow separation on the lower lip, as observed in Figure 4.6e. This reduction is mitigated at higher stagger angles, where the flow remains attached to the lower element, maintaining improved mass flow through the duct.

As depicted in Figs. 4.2e and 4.1e, both lift and drag coefficients progressively increase with higher stagger angles at a low angle of attack. This trend is attributed to the interaction between the two airfoil-like elements, where a higher stagger angle increases the pressure on the lower surface of the upper element. Additionally, at smaller stagger angles, the lower element deflects the airflow upward, reducing the effective angle of attack experienced by the upper element. Increasing the stagger angle minimizes this interference, allowing the upper element to experience a higher effective angle of attack, thereby enhancing lift.

Moreover, at a high angle of attack, variations in the stagger angle show only a marginal effect on the aerodynamic performance, as observed in Figs. 4.5e and 4.4e. This behavior is somewhat unexpected, and could be attributed to the intricate interaction between the flow structures around the airfoil-like elements under these conditions. The pressure region in front of the wing increases at higher angles of attack due to increased flow deflection toward the duct inlet. This, combined with the presence of the heat exchanger and its associated flow restriction, results in higher local pressures within the region between the duct inlet and the diffuser compared to lower angles of attack. Therefore, the combined effect of the higher angle of attack and the heat exchanger reduces the expected aerodynamic influence of the stagger angle, leading to only slight variations in the lift and drag coefficients.

Heat exchanger thickness-to-chord ratio (t_{hx}/c)

The pressure drop across the heat exchanger is directly proportional to its thickness (L), as indicated by Equation 3.21. Assuming constant porosity, increasing the thickness increases overall resistance as the flow must traverse a larger distance through the core. The viscous resistance increases due to extended frictional interaction between the fluid and the internal surfaces, resulting in more momentum dissipation due to viscous effects. At the same time, the inertial resistance increases as the boundary layer grows thicker within the voids, increasing flow obstruction and potentially lead to local flow separation and increased turbulence, further contributing to overall resistance. Vice-versa, reducing the thickness shortens the flow distance through the core, reducing both viscous and inertial losses and thereby lowering the pressure drop.

The effects of varying thickness are analogous to those of porosity, as both parameters influence overall flow resistance to flow. However, while porosity affects permeability and directly influences flow acceleration, thickness determines the physical length over which the resistance acts. In other words, flow resistance scales linearly with thickness but non-linearly with porosity. Therefore, conceptually a thicker heat exchanger behaves similarly to a low porosity core in terms of increased flow resistance, and vice versa, a thinner heat exchanger corresponds to a high porosity core. Albeit, since flow resistance scales quadratically with porosity, its effect on the overall resistance is generally larger than that of thickness variations.

As observed in Figs. 4.3f and 4.6f, the duct mass flow rate consistently decreases with increasing thickness and increases with decreasing thickness across all configurations for both low and high angles of attack. The increased flow resistance associated with a thicker heat exchanger restricts the airflow through the core, leading to a pressure buildup within the duct upstream of the heat exchanger, where the static pressure rises. However, the external pressure differential across the heat exchanger does not increase proportionally to compensate for the added flow resistance, resulting in a reduction in mass flow rate. In contrast, a thinner heat exchanger has lower flow resistance, allowing for higher mass flow rates under the same external conditions.

Furthermore, the trends observed for the lift and drag coefficients with varying heat exchanger thickness, as shown in Figs. 4.2f and 4.5f, and Figs. 4.1f and 4.4f, respectively, follow a similar pattern to those associated with porosity, as discussed in detail below. However, as previously explained, since flow resistance scales linearly with thickness, the aerodynamic effects of thickness variations are slightly less pronounced compared to porosity.

HEAT EXCHANGER POSITION-TO-CHORD RATIO (x_{hx}/c)

The chordwise position of the heat exchanger inside the duct has marginal effects on the overall aerodynamics performance. The trends are consistent across all configurations at both high and low angles of attack, showing only minor deviations. The geometrical constraints ensures that the streamlined diffuser, tangent to the upper and lower surface of the heat exchanger, slightly adjusts its internal area in response to the chordwise repositioning of the heat exchanger within the duct.

HEAT EXCHANGER POROSITY (ε)

The effective cross-sectional area available for airflow inside the heat exchanger scales with the porosity, given by $A_{\text{eff}} = \varepsilon A$, accounting for the reduction in area due to the presence of the solid core material. For lower porosity values, the increased flow resistance is attributed to the confined flow in the narrow voids, which leads to higher velocities, as described by Equation 3.20, resulting in greater viscous losses due to high shear stresses and increased inertial losses from turbulence and potential local flow separation. Additionally, as porosity decreases, the reduction in permeability further increases the viscous losses and thus overall flow resistance, resulting in the highest pressure drops at the lowest porosity levels. Moreover, the static pressure upstream of the heat exchanger increases due to the higher resistance imposed by the heat exchanger, which propagates upstream in subsonic flow. The flow responds by decreasing velocity to preserve the static-to-dynamic pressure relationship, according to Bernoulli's principle. In contrast, for higher porosity values, the increased effective cross-sectional area reduces flow resistance, leading to lower viscous and inertial losses. Furthermore, higher permeability at increased porosity further minimizes viscous losses, resulting in lower pressure drops, allowing for higher mass flow rates through the duct. The redistribution of upstream pressures due to the heat exchanger's porosity directly influences the inlet-velocity ratio, as discussed in Section 2.2.1.

In Figs. 4.3h and 4.6h, the trends across all configurations consistently show a decrease in duct mass flow rate with reducing porosity and an increase with higher porosity for both low and high angles of attack. However, slight variations in magnitudes are observed, with some configurations yielding marginally higher or lower values than others. For instance, at a high porosity level, in configuration *I-A* where the outlet is placed on the upper surface of the airfoil aft of the maximum thickness, the low-pressure region induced by supervelocities, improves the suction effect by increasing the pressure differential between the inlet and outlet, thereby drawing more air through the duct. However, at the trailing-edge, the local static pressure increases due to the adverse pressure gradient, decelerating the flow. Therefore, in configuration *II-A*, where the outlet is located at the trailing-edge, the lower pressure differential between the inlet and outlet results in a slightly reduced mass flow rate. Additionally, when the outlets are positioned on the lower surface of the airfoil, as in configurations *I-B* and *II-B*, similar effects are observed, as the higher local static pressure impair the suction effect. As a result, at high porosity levels, the mass flow rate is primarily controlled by the pressure differential across the heat exchanger, with flow resistance playing a minimal role due to reduced restriction in the core.

Furthermore, at lower porosity levels, the mass flow rate is mainly constrained by the increased flow resistance from the narrower core voids, even when a higher pressure differential is available across the heat exchanger. The available pressure energy is mostly dissipated to overcome the high viscous and inertial losses within the heat exchanger core, rather than being converted into flow acceleration. Additionally, the interaction between the low-momentum duct flow and the external velocity over the airfoil generates a shear layer at the outlet, the strength of which depends on the outlet's position. For example, the outlets positioned on the upper surface of the airfoil (*I-A* and *II-A*), the supervelocities over the upper surface create a pronounced shear layer at the duct exit. This sharp velocity inconsistency leads to increased turbulence and, in regions of adverse pressure gradients, potential flow separation outside the duct. The resulting pressure redistribution at the duct exit alters the pressure differential across the heat exchanger, further influencing the mass flow rate. Moreover, when the outlets are positioned on the lower surface of the airfoil, as in configurations *I-B* and *II-B*, the external flow velocities are relatively lower, resulting in a reduced velocity inconsistency. This minimizes shear layer formation and promotes a more gradual transition of the duct flow into the external flow, reducing turbulence and pressure disturbances at the exit.

As depicted in Figs. 4.1h and 4.4h, the drag coefficient shows a linear trend, increasing as porosity decreases and decreasing as porosity increases, consistently observed at both low and high angles of attack. This trend directly correlates with the heat exchanger pressure drop, where a lower porosity induces a larger flow resistance, leading to higher drag forces, while higher porosity levels, associated with a lower pressure drop, result in reduced drag forces. Note that in ANSYS® Fluent, the force in the porous medium is a volumetric force, meaning it accounts only for the resistance from the fluid flow through the void spaces and does not include the contribution from the solid matrix. To accurately represent the total drag force of the heat exchanger, the porous medium drag force must be divided by the porosity to account for the solid matrix contribution.

Moreover, the lift coefficient, as presented in Figs. 4.2h and 4.5h, increases with higher porosity and decreases with lower porosity, consistent for both low and high angles of attack. The observed trend can be attributed to the effect of pressure buildup in front of the heat exchanger. For low porosity values, the increased static pressure in front of the heat exchanger leads to a reduction in velocity, thereby decreasing the inlet-velocity ratio and causing the stagnation point on both lip contours of the inlet to shift inward. In contrast, for high porosity values, the static pressure decreases, increasing the inlet-velocity ratio and causing the stagnation point to shift outward closer to the natural flow alignment, analogous to the discussion in Section 2.2.1. The shift in the stagnation point alters the external pressure distribution over the airfoil up to the point of maximum thickness. For lower porosity values, the inward shift of the stagnation point increases the suction peak on the upper airfoil element, followed by a steep adverse pressure gradient. The increased pressure differential between the upper and lower surfaces of the upper airfoil improves lift generation, provided the boundary layer can sustain the adverse pressure gradient. However, the increased static pressure upstream of the heat exchanger causes higher pressure on the upper surface of the lower airfoil compared to its lower surface, resulting in a negative lift contribution. Thereby, the lower airfoil reduces the overall lift force of the ducted airfoil. Furthermore, for high porosity values, the outward shift of the stagnation point towards its natural flow alignment results in a more balanced pressure distribution over the upper airfoil, characterized by lower suction peaks and a smoother adverse pressure gradient. The reduced static pressure buildup upstream of the heat exchanger decreases the pressure differential on the lower airfoil, decreasing its negative lift contribution. Albeit the lift generated by the upper airfoil is slightly reduced due to the lower suction peak, the smaller negative lift contribution from the lower airfoil offsets this reduction, resulting in a higher overall lift coefficient at higher porosity values. On the other hand, as the upper surface of the airfoil is essential for generating lift, placing the duct outlet here, such as in configurations *I-A* and *II-A*, alters the pressure distribution by reducing the surface area available to sustain aerodynamic loads. With less surface to generate suction pressures, the lift contribution from the upper surface is inherently reduced, adversely affecting the overall aerodynamic performance. These observations highlights the critical role of heat exchanger porosity on the aerodynamic performance of wing-integrated ducts.

4.1.3. INTERACTION EFFECTS ON AERODYNAMIC PERFORMANCE

The aerodynamic performance of a wing-integrated ram-air duct is governed not only by the main effects of individual geometrical factors, but also by the interaction effects among these factors. These interaction effects reveal synergistic dependencies between parameters, presenting deeper insight into the coupled aerodynamics of the system. The interaction effects are analyzed using the same normalization approach as in the main effects analysis, where deviations of each response variable (ΔC_l, ΔC_d, $\Delta \dot{m}$) are calculated relative to zero. From the analysis, the most dominant interactions affecting aerodynamic performance were identified. Among these, the interaction between heat exchanger porosity and thickness-to-chord ratio, as well as the interaction between porosity and stagger angle, showed the strongest impact on aerodynamic forces and duct mass flow rate. These key interactions are discussed in detail in this section, while additional interactions–including *LDR* against stagger angle, *LDR* against duct gap, and duct gap against stagger angle–are provided in the Section B.4. Note that this analysis focuses on the interaction effects for configuration *I-B*, which is identified as the most optimal duct design in Section 4.2.1.

INTERACTIONS BETWEEN HEAT EXCHANGER POROSITY AND THICKNESS-TO-CHORD RATIO

The interaction effects between heat exchanger porosity and thickness-to-chord ratio show a more pronounced impact on aerodynamic performance compared to their individual main effects as discussed previously. When both factors are combined–low porosity and large thickness–the overall aerodynamic penalties become most severe. This interaction is most evident in the mass flow rate trends, as shown in Figs. 4.7c and 4.8c. The lowest mass flow rates occur at low porosity and high thickness levels, which is detrimental to cooling performance, where a high mass flow rate is required to maintain effective heat dissipation.

In terms of lift, the overall impact remains minor, with deviations ΔC_l relatively small at both angles of attack, as observed in Figs. 4.7a and 4.8a. However, at higher angles of attack, the interaction effects become more pronounced. Even at moderate thickness levels (0.10), lift decreases more rapidly as porosity is reduced, compared to the trends at low angles of attack.

This behavior indicates increased flow separation effects due to higher flow resistance at lower porosity levels, where the inward shift of stagnation points alters the pressure distribution and increases the suction peak with a steep adverse pressure gradient, promoting separation over the ducted airfoil. In contrast, at high porosity values, the lower flow resistance allows for a more favorable pressure distribution, leading to a small gain in lift even at the highest thickness-to-chord ratio.

For drag, the trends follow previous observations, increasing with decreasing porosity due to higher pressure drop across the heat exchanger. This effect is further exacerbated at larger thickness-to-chord ratios, where increased resistance extends over a longer flow distance, leading to additional aerodynamic penalties. As a result, the largest drag deviations (ΔC_d) occur at low porosity and a large thickness, where both factors maximize pressure losses and overall drag, as shown in Figs. 4.7b and 4.8b.

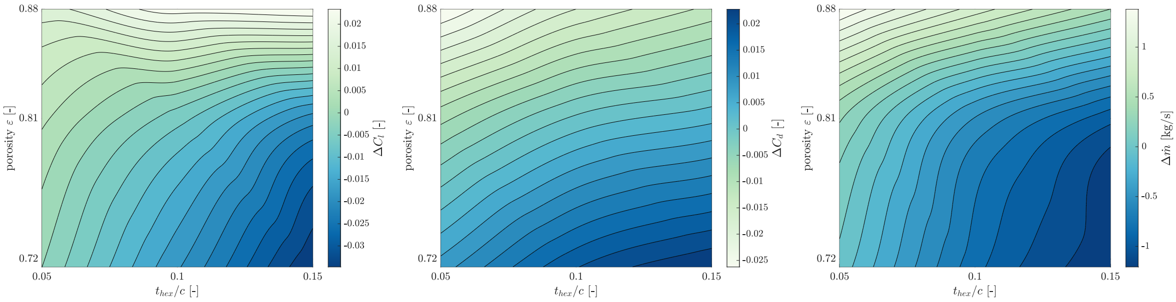

(a) Lift coefficient (b) Drag coefficient (c) Mass flow rate

Figure 4.7: Interaction effects between HX porosity and thickness-to-chord ratio on the deviation of lift coefficient (ΔC_l), drag coefficient (ΔC_d), and duct mass flow rate ($\Delta \dot{m}$) relative to the mean response value, at an angle of attack $\alpha = 2°$ and a chord Reynolds number $Re_c \approx 5 \times 10^6$.

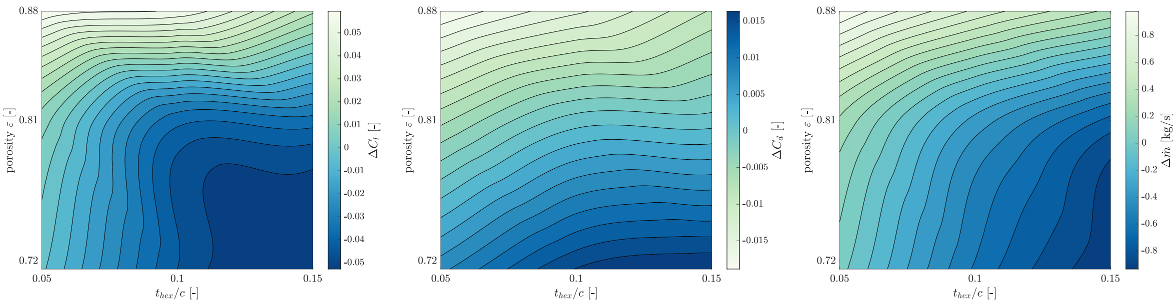

(a) Lift coefficient (b) Drag coefficient (c) Mass flow rate

Figure 4.8: Interaction effects between HX porosity and thickness-to-chord ratio on the deviation of lift coefficient (ΔC_l), drag coefficient (ΔC_d), and duct mass flow rate ($\Delta \dot{m}$) relative to the mean response value, at an angle of attack $\alpha = 10°$ and a chord Reynolds number $Re_c \approx 5 \times 10^6$.

Interactions between heat exchanger porosity and stagger angle

The interaction effects between heat exchanger porosity and stagger angle of the duct intake are complex and significantly influence aerodynamic performance. At a low angle of attack, the stagger angle has minimal impact on the duct mass flow rate, with porosity being the dominant factor–higher porosity leads to higher mass flow, as observed in Figure 4.9c. At higher angles of attack, an interaction effect emerges where increasing the stagger angle generally leads to higher duct mass flow rates, as seen in Figure 4.10c. However, this trend is not uniform across the entire porosity range. For lower porosity values (0.72-0.81), the mass flow rate initially increases with stagger angle but stabilizes beyond approximately 20°, indicating that further increases in stagger angle have little influence on mass flow rate in this range. In contrast, at higher porosity levels (above 0.81), the influence of stagger angle becomes more pronounced, with greater stagger angles resulting in increased mass flow rates. This indicates that while a larger stagger angle improves flow alignment and reduces entry losses, its effect is most significant when the heat exchanger imposes lower flow resistance.

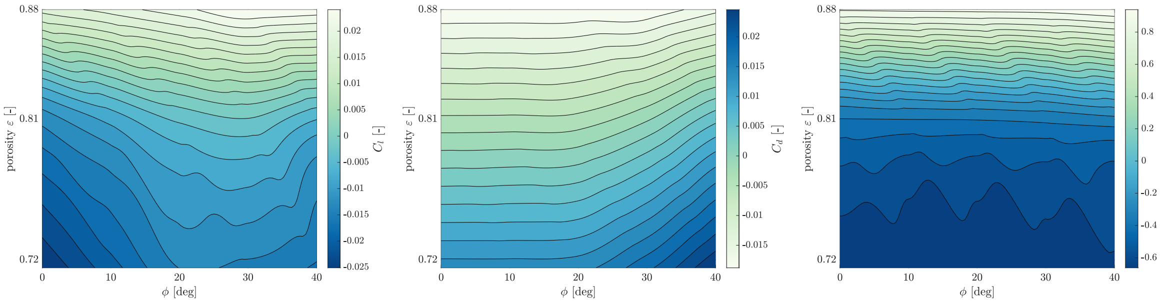

(a) Lift coefficient (b) Drag coefficient (c) Mass flow rate

Figure 4.9: Interaction effects between HX porosity and stagger angle on the deviation of lift coefficient (ΔC_l), drag coefficient (ΔC_d), and duct mass flow rate ($\Delta \dot{m}$) relative to the mean response value, at an angle of attack $\alpha = 2°$ and a chord Reynolds number $Re_c \approx 5 \times 10^6$.

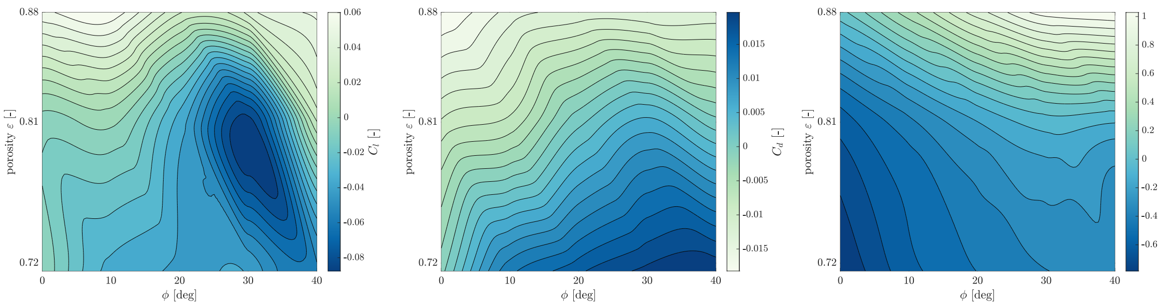

(a) Lift coefficient (b) Drag coefficient (c) Mass flow rate

Figure 4.10: Interaction effects between HX porosity and stagger angle on the deviation of lift coefficient (ΔC_l), drag coefficient (ΔC_d), and duct mass flow rate ($\Delta \dot{m}$) relative to the mean response value, at an angle of attack $\alpha = 10°$ and a chord Reynolds number $Re_c \approx 5 \times 10^6$.

In terms of lift, the overall impact remains marginal, with deviations ΔC_l relatively small at both angles of attack, as observed in Figs. 4.9a and 4.10a. At low angles of attack, the stagger angle has minimal impact on lift at high porosity values. However, at lower porosities, where flow resistance is higher, increasing the stagger angle helps mitigate lift losses by improving flow alignment into the duct. At high angles of attack, a distinct region of peak lift losses appears between stagger angles of approximately $27° - 36°$ and porosity values of $0.75 - 0.81$. This is likely attributed to excessive stagger angles, combined with increased flow resistance, inducing adverse pressure gradients and promoting flow separation, which degrades lift.

For drag, at a low angle of attack, the deviations in drag coefficient (ΔC_d) remain minimal for stagger angles up to 20°, regardless of porosity, as observed in Figure 4.9b. However, beyond this threshold, drag begins to increase, likely due to excessive stagger angles causing greater flow misalignment and pressure losses. At higher angles of attack, the trends become more pronounced, as seen in Figure 4.10b. At low porosity levels, increasing the stagger angle leads to an increase in ΔC_d, likely due to the high flow resistance generating stronger adverse pressure gradients along the lower lip, promoting earlier flow separation. As porosity increases, this effect diminishes, as the lower flow resistance reduces the adverse pressure gradient and mitigates separation effects. As a result, the stagger angle has little to no impact on drag, as the reduced resistance prevents significant aerodynamic penalties.

4.1.4. Optimal ducted airfoil shapes

Based on the evaluation of the main effects and interaction effects of the factors on aerodynamic performance, the optimal ducted airfoils in terms of aerodynamic efficiency are identified. These airfoils, with varying outlet positions, were identified as the most favorable configurations for achieving minimum drag, maximum lift, and maximum duct mass flow rates for both low and high angles of attack, as shown in Figs. 4.11 and 4.12. Since the DoE approach is utilized in this research, the optimal ducted airfoil shapes are determined based on the predefined discrete levels assigned to each factor. The optimal values for each factor are summarized in Table 4.3 for each configuration at both angles of attack. Note that this methodology does not account for continuous variations within the design space. The DoE approach effectively captures the flow physics, isolates the influence of individual factors, and identifies key interaction effects on aerodynamic performance, providing a solid foundation for determining optimal configurations within the explored design space.

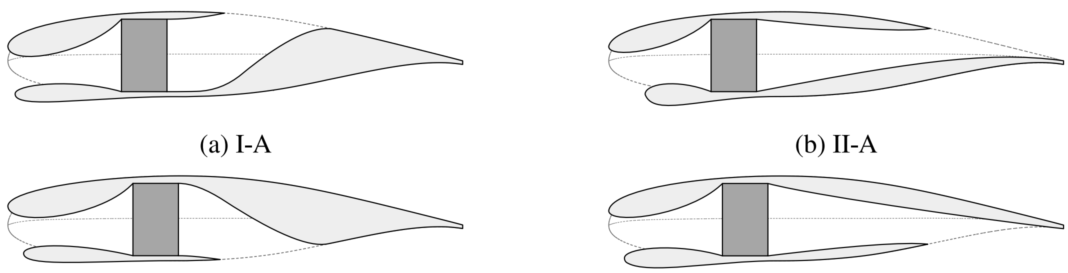

(a) I-A (b) II-A

(c) I-B (d) II-B

Figure 4.11: Optimal ducted airfoil configurations at a low angle of attack ($\alpha = 2°$), optimized for minimum drag, maximum lift, and maximum duct mass flow rate.

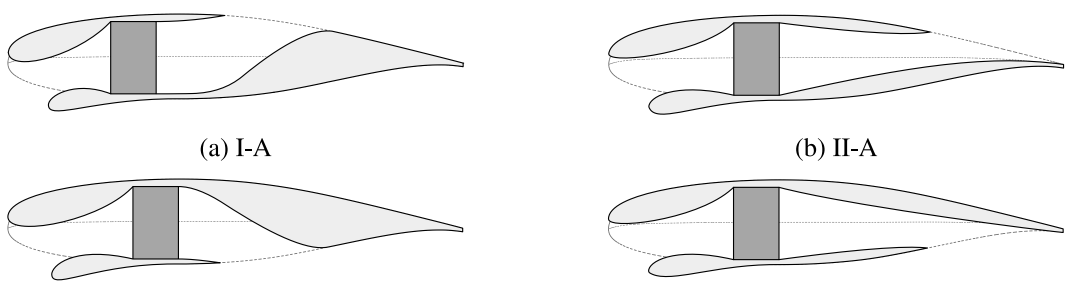

(a) I-A (b) II-A

(c) I-B (d) II-B

Figure 4.12: Optimal ducted airfoil configurations at a high angle of attack ($\alpha = 10°$), optimized for minimum drag, maximum lift, and maximum duct mass flow rate.

As observed in Table 4.3, all configurations have the maximum porosity level, aligning with expectations for minimizing flow resistance and thus maximizing mass flow rate and favorable aerodynamic performance. However, the heat exchanger thickness is fixed at 0.1, as thinner heat exchanger designs, despite their aerodynamic advantages, fail to provide sufficient internal volume to accommodate the required heat exchange area for the cooling demands associated with FCs, as discussed in Section 4.3. This balance between aero-thermal performance underscores the design trade-offs involved in developing optimal ram-air duct configurations for TMSs.

Factor	Configuration I-A		Configuration I-B		Configuration II-A		Configuration II-B	
	$\alpha = 2°$	$\alpha = 10°$	$\alpha = 2°$	$\alpha = 10°$	$\alpha = 2°$	$\alpha = 10°$	$\alpha = 2°$	$\alpha = 10°$
R_u	0.02	0.02	0.01	0.02	0.01	0.01	0.01	0.02
R_l	0.02	0.02	0.01	0.01	0.01	0.01	0.02	0.01
LDR	0.3	0.2	0.4	0.2	0.3	0.2	0.3	0.2
d/c	0.095	0.105	0.095	0.115	0.095	0.105	0.095	0.105
φ	10°	40°	20°	40°	40°	40°	20°	40°
t_{hx}/c	0.1	0.1	0.1	0.1	0.1	0.1	0.1	0.1
x_{hx}/c	0.250	0.225	0.275	0.275	0.225	0.275	0.250	0.275
ε	0.88	0.88	0.88	0.88	0.88	0.88	0.88	0.88

Table 4.3: Factor values for optimal ducted airfoil shapes at low ($\alpha = 2°$) and high ($\alpha = 10°$) angles of attack across all configurations.

4.2. AERODYNAMIC ANALYSIS OF OPTIMAL DUCTED AIRFOIL CONFIGURATIONS

In this section, RANS CFD results on the aerodynamic performance of the optimal ducted airfoil configurations are presented. Key performance parameters such as lift, drag, and duct mass flow rate are examined to determine the most suitable configuration. To improve solution accuracy, a finer grid was selected to accurately compute the aerodynamic coefficients and capture the details of the flow field. As shown in Table 4.2, the convergence trends indicate that Grid 2 is the most suitable, providing a well-converged solution for the lift and drag coefficients, with a low discretization error for lift and a slightly larger discretization error for drag. The results are shown for a freestream velocity of $V_\infty = 75\,\mathrm{m\,s^{-1}}$, corresponding to a Mach number of $M_\infty \approx 0.22$ and a chord Reynolds number of $Re_c \approx 5 \times 10^6$, undor sea-level static conditions. The rationale behind selecting these conditions is detailed in Section 4.1, where the same inlet conditions, including turbulence intensity, turbulence length scale, and intermittency, are specified.

The aerodynamic performance of the reference NASA MS(1)-0317 medium-speed airfoil is also computed under the same flight conditions. At a low angle of attack, the lift and drag coefficients are $Cl_{\alpha=2°} = 0.63$ and $Cd_{\alpha=2°} = 0.008$, respectively, while at a high angle of attack, they are $Cl_{\alpha=10°} = 1.52$ and $Cd_{\alpha=10°} = 0.016$.

First, the aerodynamic results of the various optimal configurations are compared, and the most practical ducted airfoil shape is selected for further investigation in Section 4.2.1. Subsequently, in Section 4.2.2, a qualitative assessment is conducted, focusing on the impact of heat exchanger porosity on both the aerodynamics and the entire flow field.

4.2.1. SELECTION OF THE OPTIMAL DUCTED AIRFOIL CONFIGURATION

A comparison is made between the various ducted airfoil configurations, as shown in Figure B.8, with the aerodynamic coefficients expressed as a relative percentage increase or decrease compared to the clean reference airfoil. While the results presented here correspond to a heat exchanger porosity of 0.88, additional data for lower porosity values has also been analyzed and can be found in Section B.3. Configurations *I-A* and *II-A*, with the outlet positioned on the upper surface, show a detrimental impact on lift and drag performance, as seen in Figs. 4.13a and 4.13b, a result consistent with previous discussions and anticipated aerodynamic effects. However, these configurations show an improvement in duct mass flow rate, resulting from the pressure differential between the duct inlet and outlet. On the other hand, configurations *I-B* and *II-B*, with the outlet positioned on the lower surface, show a positive effect on the lift coefficient, while the drag coefficient increases by a factor of up to 4.6 at cruise and 1.7 at climb angles of attack. Configuration *I-B* achieves a slightly higher mass flow rate than *II-B*, making it more suitable for meeting the cooling requirements of fuel cell systems, although *II-B* show greater aerodynamic efficiency but at the cost of a lower mass flow rate. Moreover, the aerodynamic shape of configuration *II-B*, as shown in Figs. 4.11d and 4.12d, may lack sufficient internal structural integrity to support the wing bending loads, potentially leading to other issues that fall outside the scope of this research. As a result, configuration *I-B* is considered the most practical option and is selected for further analysis.

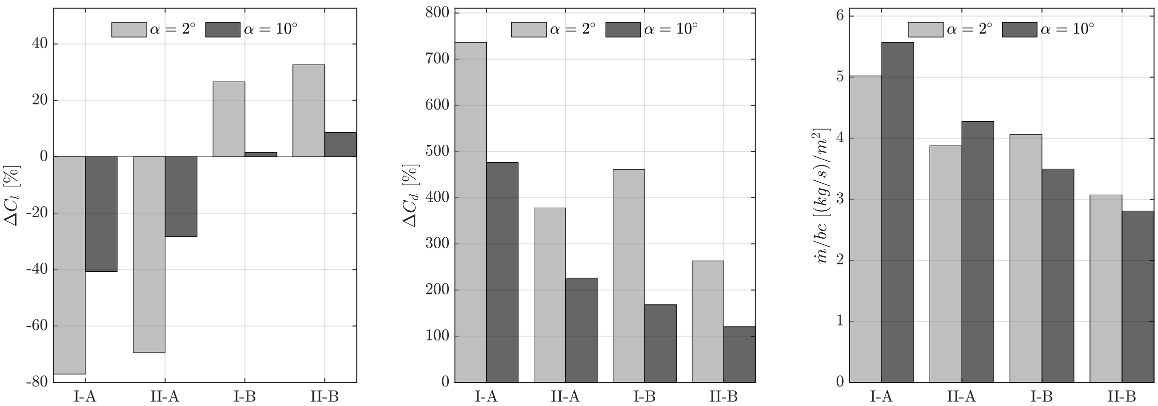

(a) Lift coefficient (b) Drag coefficient (c) Mass flow rate

Figure 4.13: Comparison of lift and drag coefficients and duct mass flow rate for the most optimal ducted airfoils relative to the clean airfoil, computed for a heat exchanger porosity of 0.88.

4.2.2. QUALITATIVE ANALYSIS OF HEAT EXCHANGER POROSITY ON AERODYNAMIC PERFORMANCE AND FLOW FIELD

The computed static pressure and velocity contours for configuration *I-B* are presented in Figs. 4.14 and 4.15, corresponding to representative cruise and climb angles of attack, respectively. The average inlet velocity of the heat exchanger is $23\,\mathrm{m\,s^{-1}}$ at the cruise angle of attack and $20\,\mathrm{m\,s^{-1}}$ at the climb angle of attack. This corresponds to an approximate pressure drop of 1400 Pa, according to Figure 3.14. The static pressure contour plots reflects this pressure drop, with a clear gradient seen across the porous medium region. Furthermore, the presence of the ducts creates a localized high-pressure region at the inlet, where the flow stagnates before entering the duct. As shown in Figure 4.14a, the duct gap is smaller in the low angle of attack configuration, resulting in a narrower duct throat compared to the high angle of attack configuration, as depicted in Figure 4.15a. This constriction accelerates the flow through the duct throat, generating higher-momentum flow. The downstream diffuser improves pressure recovery, effectively managing the adverse pressure gradient induced by the porous medium while preventing flow separation. On the other hand, at high angles of attack, the larger throat still accelerates the flow, albeit to a lesser extent. The diffuser continues to enhance pressure recovery, ensuring the flow remains stable and attached throughout the duct as seen from the streamlines. Furthermore, the heat exchanger acts as a flow straightener, promoting a more uniform flow as it exits the duct. The nozzle geometry, with its integrated curvature at the bottom of the upper surface, accelerates the flow as it exits the duct, as indicated by the compressed streamlines.

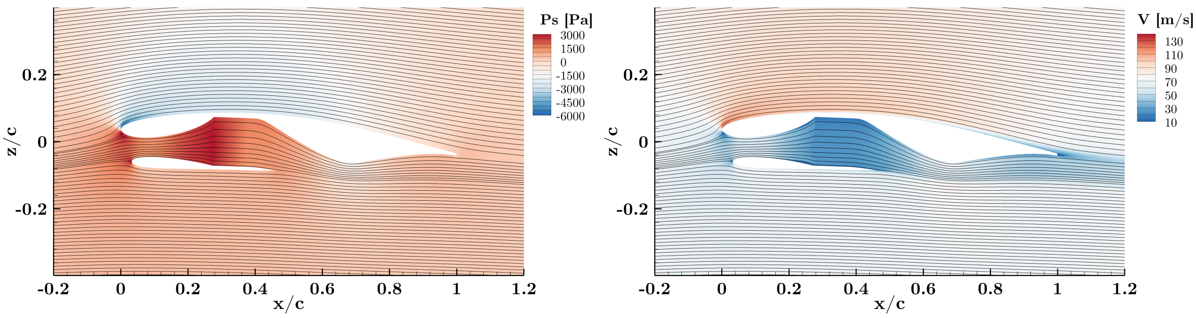

(a) Static pressure

(b) Velocity

Figure 4.14: Computed static pressure and velocity contours, including streamlines, for configuration *I-B* at $\alpha = 2°$ and a chord Reynolds number of $Re_c \approx 5 \times 10^6$.

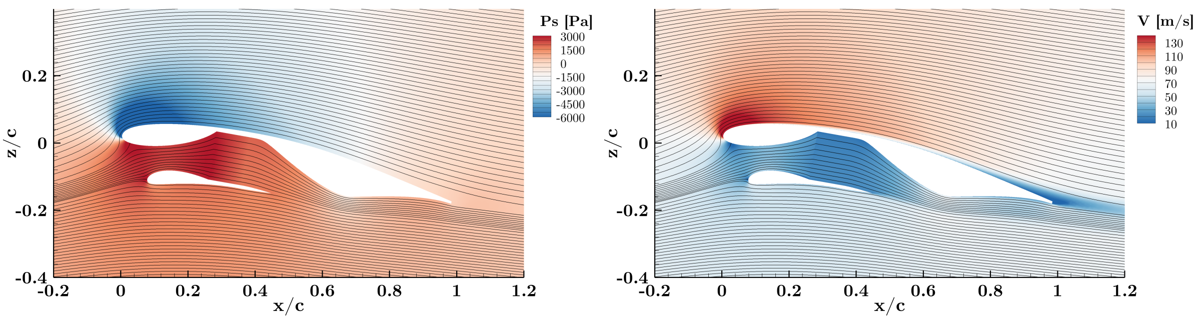

(a) Static pressure

(b) Velocity

Figure 4.15: Computed static pressure and velocity contours, including streamlines, for configuration *I-B* at $\alpha = 10°$ and a chord Reynolds number of $Re_c \approx 5 \times 10^6$.

In Figure 4.16, streamlines of the entire flow field in the vicinity of the duct inlet for different heat exchanger porosity values are plotted for the same configuration (*I-B*) at representative cruise and climb angles of attack, respectively. A heat exchanger porosity of one indicates the absence of flow resistance, effectively representing a duct with no internal blockage to the flow. The effect of varying heat exchanger porosity on the flow field around the ducted airfoil is evident up to near the point of maximum thickness, beyond which no major changes are observed. For low subsonic flow ($M < 0.3$), pressure waves propagate isotropically at the speed of sound, thereby allowing greater upstream propagation for lower porosity values due to the increased flow resistance, which alters the flow field ahead of the ducted airfoil. Furthermore, the stagnation streamlines, as depicted in Figure 4.17, provide a clearer visualization of the shift in the stagnation point caused by variations in heat exchanger porosity. By lowering the porosity, the static pressure increases, decreasing the inlet-velocity ratio and causing the stagnation point to shift inward. Vice-versa, for high porosity values, the static pressure decreases, increasing the inlet-velocity ratio and causing the stagnation point to shift outward closer to the natural flow alignment, analogous to the discussion in Section 4.1.2. The natural flow alignment occurs when the heat exchanger porosity is one, as this condition removes internal blockage effects.

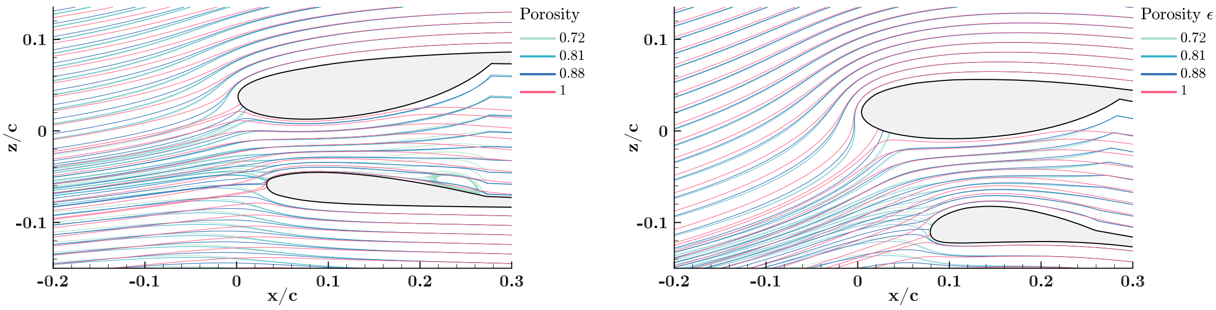

(a) Cruise angle of attack ($\alpha = 2°$)

(b) Climb angle of attack ($\alpha = 10°$)

Figure 4.16: Flow field streamlines as a function of heat exchanger porosity for different angles of attack, showing the influence of porosity on the flow field in the vicinity of the ducted airfoil.

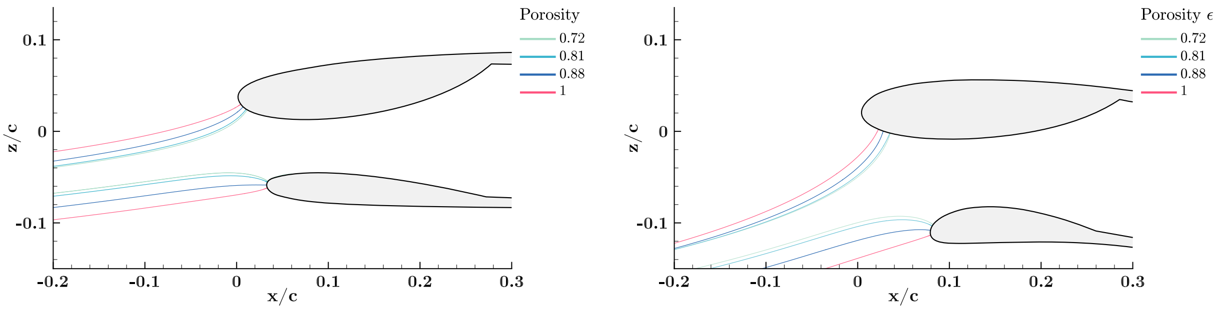

(a) Cruise angle of attack ($\alpha = 2°$)

(b) Climb angle of attack ($\alpha = 10°$)

Figure 4.17: Stagnation streamlines as a function of heat exchanger porosity for different angles of attack, showing the influence of porosity on the shift in the stagnation point in the vicinity of the leading-edge.

In Figs. 4.18 and 4.19, the influence of heat exchanger porosity on the pressure distribution is shown for the upper and lower elements of the wing-integrated duct. The shift in the stagnation point caused by flow resistance significantly impacts the pressure distribution around the duct inlet, especially at a low angle of attack, as shown in Figure 4.18a. The pressure distribution remains unaffected aft the point of maximum thickness on the upper element, located at approximately 37% of the chord. The inward shift of the stagnation point has a significant effect on the suction peak of the upper element, followed by a steep adverse pressure gradient caused by the increased flow resistance associated with low porosity, as previously discussed. This effect reduces as the flow resistance decreases with higher porosity. Despite the large suction peaks and the steep adverse pressure gradient, the boundary layer remains attached. Furthermore, on the lower surface of the upper element, between the leading-edge and the duct throat, a slight decrease in static pressure is observed due to flow acceleration. However, within the diffuser region, an increase in static pressure is observed, which is part of the pressure recovery mechanism. Following the diffuser, the pressure drop across the porous medium is observed, with the gradient quantifying the imposed flow resistance. When the flow exits the heat exchanger and enters the nozzle, the acceleration induces a pressure reduction, continuing until the flow passes the curvature along the bottom surface of the upper airfoil element. The pressure differences between the upper and lower surfaces increase as porosity decreases, indicative of higher net aerodynamic forces acting on the airfoil.

Additionally, the impact of the stagnation point shift on the pressure distribution along the lower airfoil element is shown in Figure 4.19a. Similar effects in the pressure differences between the upper and lower surfaces are observed. However, the net aerodynamic force is reversed in this case, as higher pressures on the upper surface and lower pressures on the bottom surface result in a negative aerodynamic force. Consequently, the lower element reduces the overall aerodynamic forces generated by the ducted airfoil. The same observations discussed are applicable to the upper and lower elements of the wing-integrated duct at a high angle of attack, as observed in Figs. 4.18b and 4.19b.

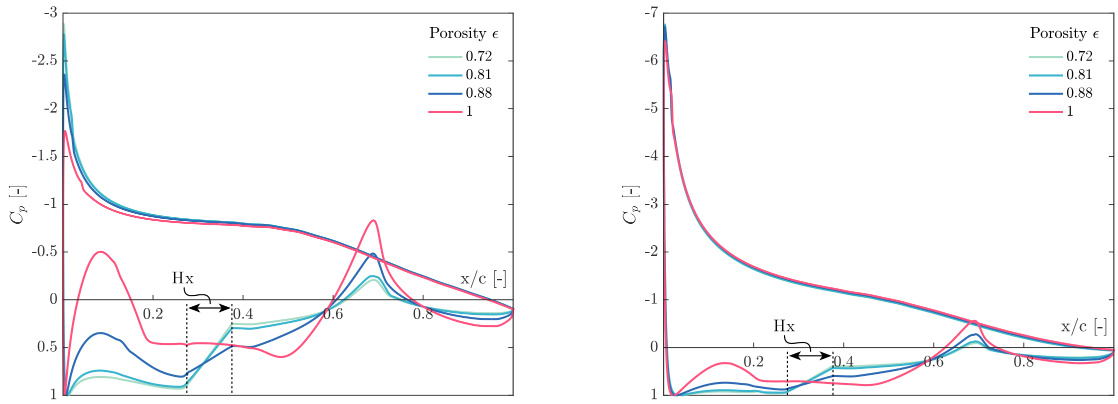

(a) Cruise angle of attack ($\alpha = 2°$)

(b) Climb angle of attack ($\alpha = 10°$)

Figure 4.18: Pressure coefficient (C_p) distribution along the upper element of the wing-integrated duct for various heat exchanger porosity levels.

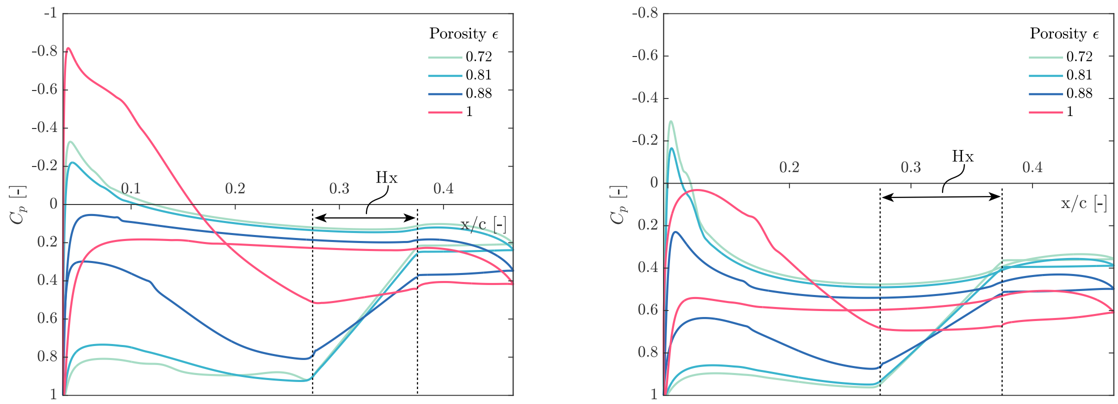

(a) Cruise angle of attack ($\alpha = 2°$)

(b) Climb angle of attack ($\alpha = 10°$)

Figure 4.19: Pressure coefficient (C_p) distribution along the lower element of the wing-integrated duct for various heat exchanger porosity levels.

4.3. Thermal performance of selected ducted airfoil configuration

In this section, additional RANS simulations are performed to evaluate the thermal performance of the wing housing the heat exchanger, while also assessing the feasibility of integrating the heat exchanger within the ducted wing. As defined in Table 3.4, the full-scale heat exchanger should achieve a heat transfer rate $\dot{q}$ of 280 kW. Considering the ATR-72 turboprop aircraft as reference, which has a root chord of 2.62 m [58], the scaled heat transfer rate for the simulation domain, where the span is fixed to 1 m, is calculated as $\dot{q}_{\text{scaled}} = \dot{q}/(c^2) = 40.8\,\text{kW}\,\text{m}^{-2}$. Since both the height and thickness of the heat exchanger scale proportionally with the chord length, the heat transfer rate scales with the square of the chord length. This ensures consistency with the airfoil's characteristic length, which is normalized to $1c$ in the domain, requiring that all parameters in the thermal performance computations be scaled accordingly relative to the reference chord length.

The most optimal ducted airfoil configurations identified from the DoE study showed that the optimal thickness-to-chord ratio for the heat exchanger is 0.10, as presented in Table 4.3. This is attributed to the thinner heat exchanger resulting in a lower pressure drop, thereby minimizing its adverse impact on aerodynamic performance. However, preliminary thermal performance computations reveal that achieving the required heat transfer rate ($\dot{q}_{\text{scaled}}$) results in a heat transfer area that exceeds the wing's internal volume constraints for a thickness-to-chord ratio of 0.10. The compactness associated with the porosity of 0.88, approximately $600\,\text{m}^2\,\text{m}^{-3}$ [52], imposes constraints on the achievable heat transfer area, making it difficult to fit within the wing's internal volume for the current thickness-to-chord ratio. As a result, a larger thickness-to-chord ratio of 0.15 must be considered to ensure the heat transfer area fits within the available volume, given the fixed compactness associated with the selected porosity. The same selected airfoil configuration (*I-B*), as discussed in Section 4.2.1 is used, with the shape illustrated in Figure 4.20. The optimal factor values for the shapes at both low and high angles of attack are presented in Table 4.4.

(a) $\alpha = 2°$ (b) $\alpha = 10°$

Figure 4.20: Optimal ducted airfoil configurations at low and high angles of attack from the DoE study, meeting fuel-cell heat dissipation requirements and optimized for minimum drag, maximum lift, and maximum duct mass flow rate.

The detailed heat exchanger sizing process for the configuration discussed in this section is provided in Appendix A. The process is conducted at a low angle of attack, representative of cruise conditions, though performed under sea-level conditions to correspond to the mass flow rate at this angle. With the heat exchanger parameters fixed, the duct velocity is varied to obtain the heat transfer rate as a function of velocity, as depicted in Figure A.2. A 6th-degree polynomial is fitted to the resulting data, enabling the estimation of off-design thermal performance, such as changes in heat transfer when the angle of attack varies. This polynomial is then implemented as a UDF in the porous zone, defined as a variable volumetric heat source term.

Factor	Configuration I-B	
	$\alpha = 2°$	$\alpha = 10°$
R_u	0.01	0.02
R_l	0.02	0.01
LDR	0.4	0.3
d/c	0.095	0.115
φ	20°	40°
t_{hx}/c	0.15	0.15
x_{hx}/c	0.275	0.275
ε	0.88	0.88

Table 4.4: Optimal factor values for configuration *I-B*, meeting the heat dissipation requirements for fuel cell systems.

In Figure 4.21, the computed static temperature distribution is shown for the optimal shapes. At a low angle of attack, as shown in Figure 4.21a, the temperature distribution indicates an average outlet temperature of approximately 310 K, consistent with the computed cold outlet temperature detailed in Appendix A. This consistency validates the thermal modeling of the heat exchanger within the computational domain in ANSYS® Fluent. Moreover, at a high angle of attack, as shown in Figure 4.21b, the average outlet temperature is slightly higher, which is expected due to the slight reduction in mass flow rate within the duct, resulting in a corresponding increase in the heat exchanger outlet temperature. It should be noted that, due to the fixed wing span in the domain, the scaling follows the chord length squared (c^2) rather than the volume. As a result, the temperature difference across the cold side remains relatively small at approximately 10 K. However, for the full-scale heat exchanger, as detailed in Appendix A, this difference increases to 26 K, resulting to a cold side outlet temperature of approximately 327 K.

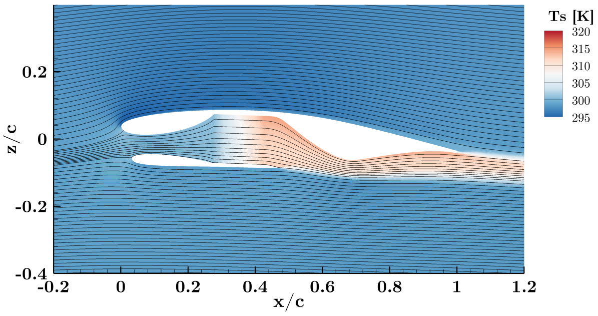

(a) Cruise angle of attack ($\alpha = 2°$)

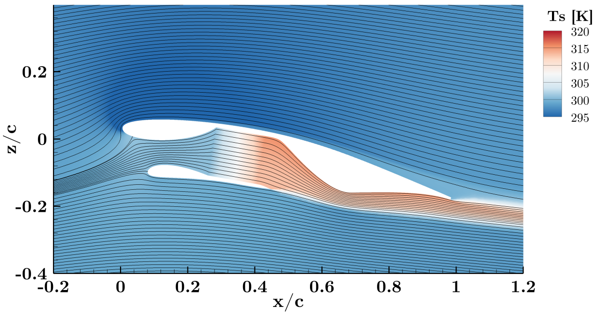

(b) Climb angle of attack ($\alpha = 10°$)

Figure 4.21: Computed static temperature distribution, including streamlines, for configuration *I-B* for a chord Reynolds number of $Re_c \approx 5 \times 10^6$.

Furthermore, the phenomenon described by Meredith [59] occurs when heat is transferred to the airflow within a ducted heat exchanger, causing the air to expand and accelerate, thereby increasing momentum and potentially contributing to thrust generation or drag reduction. The practicality of this effect depends on the nozzle design, where the added heat and resulting pressure increase from gas expansion are effectively converted into kinetic energy, as well as on the flow conditions at the nozzle exit and the Mach number. This added forward momentum offsets the drag forces associated with the cooling installation or directly contributes to thrust generation. At sea-level conditions, as observed in Figure 4.21, the relatively low outlet temperature of the scaled heat exchanger and the high ambient static pressure result in a minimal pressure differential at the nozzle exit, thereby limiting the drag reduction or thrust contribution, as observed in Figure 4.22. For the full-scale model, although the outlet temperature is slightly higher, the high static pressure at sea level still constrains the Meredith effect. At higher altitudes, the decreased ambient pressure increases the pressure differential at the nozzle exit, and the lower ambient temperature improves the heat exchanger's effectiveness, leading to a higher outlet temperature. Additionally, at higher flight speeds, the increased dynamic pressure leads to a higher mass flow rate through the duct, improving the heat transfer. This further increases the outlet temperature, and thus amplify the Meredith effect. The thrust that can be obtained through the Meredith effect at sea-level conditions is negligible compared to the drag, as shown in Figure 4.22. However, its relevance under different flight conditions, where it could potentially offset the additional cooling drag, is worth noting.

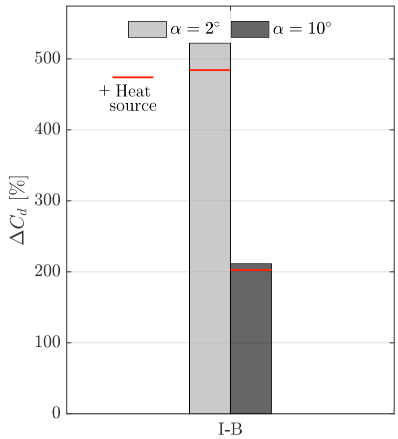

Figure 4.22: Comparison of drag coefficients for configuration *I-B* relative to the clean airfoil, for cases with and without the heat source term applied within the porous medium.

4.4. Effect of propeller-induced flow on ducted wing performance

The presence of a propeller in a ducted-wing system significantly alters the inflow characteristics, influencing duct performance through variations in axial and tangential velocity distributions. As depicted in Figure 4.23a, the propeller induces an axial velocity increase of approximately 10% to 30% over the freestream velocity. However, this increment depends on several factors, including thrust setting, blade pitch angle, advance ratio, and the specific flight condition. Higher thrust settings and lower advance ratios generally result in greater induced velocities. Due to the radial distribution of thrust, the axial velocity is non-uniform across the propeller disk, with its peak increase occurring around 70% to 80% of the propeller radius, where blade loading is highest. This distribution plays a crucial role in determining the duct's effective inflow conditions.

The increased axial velocity directly enhances duct mass flow rate, which scales proportionally with velocity for a fixed inlet area and air density. As a result, more air is ingested into the duct, improving heat exchanger performance by enhancing heat dissipation. This suggests that the spanwise extent of the duct or the thickness of the heat exchanger could potentially be reduced while maintaining the required cooling capacity. Such modifications would reduce the aerodynamic penalty associated with increased heat exchanger thickness.

In addition to the axial velocity effects, the propeller also induces tangential velocity components, as shown in Figure 4.23b, generating a swirl component in the inflow. This swirl alters the local angle of attack of the duct inlet, which impact the local aerodynamics. A moderate swirl may enhance ducted wing performance by increasing lift, while excessive swirl could induce flow separation at the lower lip of the duct leading to an additional drag penalty. The balance between axial and tangential velocity effects is therefore critical for optimizing the duct's aerodynamic performance.

While the induced increase in mass flow rate offers design advantages, the non-uniform velocity distribution complicates optimization efforts. The combined effects of axial acceleration, swirl, and boundary layer interaction require careful consideration when refining the duct geometry to minimize drag while maintaining sufficient cooling capacity. Additionally, the unsteady nature of the propeller wake introduces fluctuations in velocity and pressure, which can potentially influence unsteady heat transfer dynamics within the duct. These time-dependent variations may affect heat exchanger effectiveness, potentially requiring further optimization of the duct's internal flow characteristics to ensure stable thermal performance under varying operating conditions.

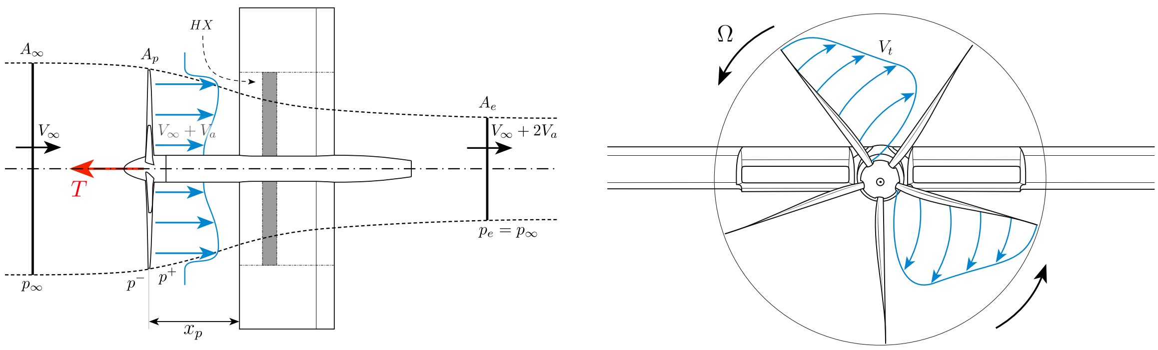

(a) Axial velocity distribution (adapted from [48])

(b) Tangential velocity distribution

Figure 4.23: Stream-tube analysis of a propeller/ducted-wing system: highlighting axial and tangential development of velocity.

4.5. CONCLUSIONS

In this chapter, the 2D aerodynamic performance of a wing-integrated duct housing a heat exchanger was analyzed under representative climb and cruise angles of attack. The impact of key external geometric parameters was presented, addressing the first research question **Q1**. Additionally, the effects of heat exchanger-induced flow restrictions on aerodynamic performance were assessed, considering variations in heat exchanger porosity, thickness, and chordwise positioning, thereby addressing the second research question **Q2**. The conclusions drawn from these analyses are presented separately, followed by a discussion on the thermal effects of the heat exchanger and its feasibility within a ducted wing.

Findings in relation to research question Q1

By analyzing the trends observed in the DoE study, the sensitivity of the lift and drag coefficients, as well as the duct mass flow rate, to key geometric parameters was assessed. The results provide a comprehensive understanding of how variations in external ram-air duct design features influence aerodynamic performance. A summary of these effects is presented below:

- Lip radii: A larger lip radius contribute to improved duct mass flow rate by minimizing internal losses, but their impact on lift and drag remains negligible. Additionally, a larger lip radius allows for greater flexibility in the stagnation point location under varying conditions, ensuring a smoother pressure transition and reducing sensitivity to changes in flow direction.

- Gap-to-chord ratio (d/c): A larger gap improves mass flow rate by expanding the inlet area but increases drag due to higher frontal area and flow interactions, while also reducing lift by disturbing the pressure distribution on the airfoil.

- Leading-edge Droop Ratio (LDR): While its effect is negligible at low angles of attack, at high angles, a lower leading-edge droop ratio improves lift and reduces drag by mitigating flow separation.

- Stagger angle (φ): While larger stagger angles improve lift and maintain higher duct mass flow at low angles of attack, its impact reduces at high angles due to increased local pressure buildup and heat exchanger-induced flow restrictions.

Furthermore, for configurations with the duct outlet positioned on the upper surface (*I-A* and *II-A*), although the placement within a low-pressure region improves the duct mass flow rate, they also leads to a substantial reduction in lift and an increase in drag due to the disruption of the upper surface responsible for generating aerodynamic loads. In contrast, configurations with the duct outlet positioned on the lower surface (*I-B* and *II-B*) show improved lift characteristics, albeit incurring an increase in drag, while the duct mass flow rates are lower due to a reduced pressure differential across the heat exchanger. It can thus be concluded that configuration *I-B*, with the duct outlet positioned just aft of the maximum thickness, represents the most practical ducted airfoil design, as it sustains higher duct mass flow rates while mitigating adverse aerodynamic effects. This configuration achieves an optimal compromise among aerodynamic efficiency, heat exchanger cooling performance, and internal structural integrity to support wing bending loads–though the latter introduces additional considerations beyond the scope of this research.

Findings in relation to research question Q2

In addressing the second research question, the effects of heat exchanger-induced flow restriction–considering variations in porosity, thickness, and chordwise positioning–were systematically assessed to determine their impact on the sensitivity of lift, drag, and duct mass flow rate. These results elucidate how the heat exchanger geometric attributes influence ducted flow behavior and overall aerodynamic performance. A concise overview of these outcomes is detailed below:

- HX porosity (ε): Porosity directly affects duct performance by regulating flow resistance, mass flow rate, and aerodynamic forces. Lower porosity increases resistance, leading to higher pressure losses, reduced mass flow rate, and increased drag, while shifting the stagnation point inward and altering the pressure distribution. Vice-versa, higher porosity allows greater airflow through the duct, reducing pressure buildup and drag while also modifying the pressure distribution by shifting the stagnation point outward, closer to its natural location on a ducted wing without a heat exchanger. These results highlight the fundamental trade-offs between aerodynamic performance and cooling efficiency in wing-integrated ram-air ducts.

- HX thickness (t_{hx}/c): A thicker heat exchanger increases flow resistance by extending the region over which viscous and inertial losses occur, reducing mass flow rate while increasing drag and pressure buildup. In contrast, a thinner core allows for improved airflow and reduced aerodynamic penalties. However, the aerodynamic impact of thickness is secondary to that of porosity, as its effect on flow resistance scales linearly rather than quadratically.

- HX position (x_{hx}/c): Repositioning the heat exchanger within the duct has little effect on aerodynamic performance, as the streamlined diffuser remains tangent to the heat exchanger surfaces and adjusts accordingly.

Beyond these primary research objectives, additional RANS CFD simulations were conducted on the most practical ducted wing configuration, incorporating a volumetric heat source term to assess the heat exchanger thermal performance and its aerodynamic implications. The volumetric heat source implementation was validated by ensuring that the computed outlet temperatures matched expected values. At sea-level conditions, the Meredith effect was found to be negligible due to low outlet temperatures and high ambient pressure. However, at higher altitudes and speeds, the increased temperature differential and reduced static pressure could enhance thrust recovery potential, making thermal effects more significant in duct performance optimization.

Furthermore, the feasibility of integrating the heat exchanger within the wing volume was analyzed as part of this study. Based on the findings from the DoE study, the ducted wing configuration with a low thickness-to-chord ratio was selected to minimize aerodynamic losses. However, as further assessments were conducted, it became evident that a heat exchanger thickness-to-chord ratio of 0.10–while aerodynamically favorable–was insufficient to meet the 280 kW thermal dissipation requirements of the fuel-cell system. To accommodate the necessary heat transfer area dictated by the compactness requirement of the selected highest porosity, a larger thickness-to-chord ratio of 0.15 was required. This design trade-off resulted in a negative impact on aerodynamic performance, as the increased thickness introduced additional flow resistance and drag penalties.

5

3D Aerodynamic performance

In this chapter the three-dimensional aerodynamic performance characteristics of the wing-integrated duct housing a heat exchanger are discussed. The optimal ducted airfoil profiles obtained from the 2D analysis is mounted perpendicularly on a flat plate to investigate the wing-body junction flow phenomena. This quasi-3D approach, as detailed in Section 3.5.2, allows for a focused study of junction flow behavior while reducing computational costs. Throughout this chapter, 3D RANS CFD results are presented to analyze the interaction between boundary layers, secondary vortical structures, and heat exchanger-induced flow resistance, addressing the following research question:

> **Q3:** *How does the aerodynamic interaction between the wing-integrated duct and a flat plate affect the 3D wing-body junction flow phenomena under climb and cruise angles of attack?*

The aerodynamic performance of the nacelle/ducted-wing configuration is scrutinized in Section 5.1, including a grid convergence study and a comparison with the 2D ducted wing model to assess performance trends. Furthermore, in Sections 5.2 and 5.3, the formation of the HSV and corner flow separation in the junction region are qualitatively analyzed to further gain insight into the impact of heat exchanger-induced flow resistance on 3D aerodynamic duct performance.

5.1. Aerodynamic analysis of the nacelle/ducted-wing junction flow

This section presents RANS CFD simulation results analyzing the aerodynamic performance and junction flow characteristics of the simplified nacelle/ducted-wing model. The same optimal ducted airfoil profiles as discussed in Section 4.2.1 are used, mounted perpendicularly on a flat plate as a simplified representation of the nacelle. The rationale for using this simplified representation is outlined in Section 3.5.2. The simulations are performed using a quasi-3D approach, where a symmetry boundary condition is applied to one side of the domain, effectively limiting three-dimensional flow effects, as shown in Figure 3.6. First, a grid convergence study is performed, as presented in Section 5.1.1, to assess the aerodynamic performance of the nacelle/ducted-wing model with the heat exchanger modeled as a porous medium zone, providing confidence in the selected grid resolution. Then, in Section 5.1.2, the aerodynamic performance of the nacelle/ducted-wing model is analyzed in relation to the 2D ducted wing model, with a focus on the impact of heat exchanger porosity on secondary flow structures in the junction. For this analysis, the same simulation and operating conditions as in the 2D analysis (Section 4.1) are applied.

5.1.1. Grid convergence

The 3D computational domain for the simplified nacelle/wing-integrated duct model, as shown in Figure 3.6, is assessed for grid convergence to gain confidence in the selected grid. Similar to the 2D analysis, the same grid convergence methodology is applied here, as discussed in Section 4.1.1. The highest heat exchanger porosity (e.g., 0.88) is assigned to the porous medium zone, as this was identified as optimal for ducted airfoils in the 2D analysis. Table 5.1 presents the grid sizes and corresponding refinement ratios h_i/h_1 for the five grids utilized in the junction flow study. Furthermore, Table 5.2 provides the solutions obtained on different grids, including the observed order of convergence, the standard deviation of the fitted data, and the discretization error estimate associated with the chosen grid.

Grid	Number of cells	h_i/h_1
5	2881866	2.24
4	5451887	1.82
3	10267386	1.47
2	18924292	1.20
1	32684400	1.00

Table 5.1: Grid sizes and refinement ratios for the computational domain of the nacelle-wing configuration.

The 3D RANS simulations are computationally expensive due to the high spatial resolution required to resolve the flat-plate and ducted-wing boundary layers, as well as to capture complex junction flow interactions and secondary vortical structures. For both boundary layers, a $y^+ \leq 1$ is required for accurate near-wall resolution using the SST $k-\omega$ turbulence model coupled with the $\gamma-\mathrm{Re}_\theta$ transition model. To balance computational cost and solution accuracy, Grid 2, with approximately 18.9 million cells, is selected for its relatively fine resolution to sufficiently capture secondary flow structures in the junction region. Grid convergence for the junction flow was verified by analyzing 3D lift and drag coefficients computed at representative cruise and climb angles of attack.

In Table 5.2, all fits shows that the observed order of convergence exceeds the theoretical value of $p = 2$. As a result, the discretization error is estimated based on the theoretical order using the formulation in Equation 3.18, specifically applying the third entry of the equation. The best fit for $C_{L_{\alpha=2^\circ}}$ and $C_{D_{\alpha=2^\circ}}$ shows monotonic convergence, though slight scatter is present for the finer grid. The difference in standard deviations between the fits using the observed and theoretical orders is negligible, indicating a good fit was obtained. It can be concluded that the lift coefficient computed at a low angle of attack has converged well on Grid 2, with an estimated discretization error of 2.5%, while a higher discretization error of 6.7% was observed for the drag coefficient. This is attributed to the high sensitivity of drag calculations to numerical diffusion, particularly in regions with steep velocity and pressure gradients, such as in the streamwise and spanwise boundary layers near the junction and wake. Furthermore, both $C_{L_{\alpha=10^\circ}}$ and $C_{D_{\alpha=10^\circ}}$ shows a monotonic convergence trend. However, the estimated discretization errors remain relatively high at 6.3% and 8.6%, respectively. At this higher angle of attack, unsteady effects become more prominent, resulting in time-varying aerodynamic loads on the ducted wing. This unsteadiness mainly comes from stronger vortex interactions in the junction region, which lead to local fluctuations in pressure and velocity fields. These transient effects are not captured using steady-state RANS simulations, such as time-dependent vortex evolution and possible intermittent flow fluctuations. Therefore, it increases discrepancies in aerodynamic force estimation. Additionally, the steep velocity gradients associated with the stronger vortical structures in the junction region at this angle of attack, may not be entirely resolved due to numerical diffusion, affecting the computed strength (circulation), size, and location of the HSV.

ϕ_i	$C_L(\alpha = 2°)$	$C_D(\alpha = 2°)$	$C_L(\alpha = 10°)$	$C_D(\alpha = 10°)$
ϕ_5	0.8156	0.0416	1.6045	0.0421
ϕ_4	0.8036	0.0430	1.5410	0.0450
ϕ_3	0.7945	0.0449	1.5036	0.0444
ϕ_2	0.7914	0.0446	1.4904	0.0454
ϕ_1	0.7919	0.0450	1.4913	0.0453
p	3.45	3.76	3.89	7.81
$U_s(\%)$	0.09	0.38	0.15	0.58
$U_s^*(\%)$	0.12	0.41	0.32	0.63
$\lvert U_{\phi_2}\rvert(\%)$	2.46	6.74	6.30	8.65

Table 5.2: Grid dependency study for the simplified nacelle-wing juncture flow analysis.

5.1.2. COMPARISON OF AERODYNAMIC PERFORMANCE METRICS

RANS simulations are performed on the nacelle/wing-integrated duct model for varying heat exchanger porosity to assess the impact of flow resistance on both overall aerodynamic performance and the junction flow characteristics. A comparison is made with the 2D ducted wing configuration, as presented in Figure 5.1, with the aerodynamic coefficients quantified as relative percentage changes compared to the clean reference wing. Note that the 3D aerodynamic coefficients are referenced to the area S, which remains equivalent to the 2D chord-based scaling due to unit span and chord, allowing direct comparison.

Due to the presence of secondary flow structures, including the HSV and corner separation, the lift coefficient decreases while the drag coefficient increases, as observed in Figs. 5.1a and 5.1b, respectively. A stronger HSV, depending on its vertical location relative to the wing surface, affects the susceptibility to corner flow separation due to the redistribution of momentum by increased Reynolds stresses within both the streamwise and spanwise boundary layers. When the HSV forms higher above the wing, its ability to entrain high-momentum freestream air into the junction region is reduced. As a result, the vortex primarily pulls low-momentum air from the wing junction, thickening the boundary layer and increasing the momentum deficit, thereby making it more susceptible to corner flow separation, especially in areas with strong adverse pressure gradients. Also, the wall shear stress is reduced due to reduced velocity gradients in these areas. Vice-versa, if the HSV forms closer to the wing, its interaction with regions of adverse pressure gradient can help mitigate the momentum deficit within the boundary layer, delaying the onset of corner flow separation. However, as high-momentum freestream air is entrained into the boundary layer, the resulting steeper velocity gradients lead to an increase in wall shear stress. Therefore, both the vertical position and circulation strength of the HSV determine whether it acts as a stabilizing or destabilizing mechanism for the boundary layers in the junction.

The computed MDF values at $x/c = -0.3$ upstream of the wing are 4.4×10^9 and 5.2×10^9 for the optimal airfoil shapes at low and high angles of attack, respectively. Similarly, the bluntness factor (BF) is determined as $\mathrm{BF} = 1.96 \times 10^{-2}$ and $\mathrm{BF} = 3.93 \times 10^{-2}$ for the respective optimal airfoil shapes. A lower BF is associated with a weaker HSV, while a higher BF leads to a stronger HSV with an increased stretching rate [37], further reinforcing its circulation strength and influence on the junction flow. At a low angle of attack, the HSV remains relatively weak due to relatively lower MDF and BF, which affects the pressure distribution on the wing only to a certain extent, leading to a small reduction in lift and increase in interference drag. As the angle of attack increases, the streamwise adverse pressure gradient upstream of the wing increases, triggering earlier onset of three-dimensional flow separation, which in turn strengthens the HSV as reflected in the higher MDF value, increasing its size and vorticity while pushing it further above the wing in vertical extent. The reduction in lift is attributed to the downwash induced by the trailing upper leg of the HSV near the wing junction, which decreases the local effective angle of attack and reduces the suction peaks in this region. This results in a localized loss of lift at the junction, analogous to the effect of wingtip vortices on the wing lift distribution. Furthermore, the downwash increases localized induced drag, further contributing to the overall drag.

In addition to interference drag, additional pressure drag from unsteady corner separation at high angles of attack further impacts the overall aerodynamic penalty, as the uplifted HSV fails to entrain sufficient high-momentum freestream air into the junction boundary layer, increasing the momentum deficit and promoting separation. Furthermore, the higher flow restriction associated with lower porosity levels further exacerbates the lift and drag coefficients due to the increased local pressure upstream of the heat exchanger, which increases the streamwise adverse pressure gradient upstream of the wing further. This results in a greater momentum deficit in the boundary layer, which corresponds to even higher MDF values, thereby reinforcing HSV formation and extend it further vertically from the wing surface.

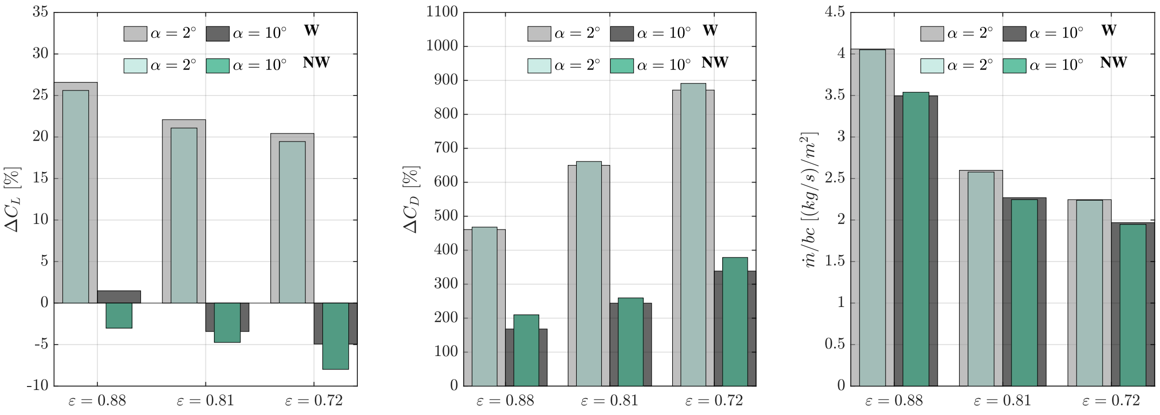

(a) Lift coefficient (b) Drag coefficient (c) Mass flow rate

Figure 5.1: Comparison of lift, drag coefficients, and duct mass flow rate for the nacelle-wing (NW) and wing-only (W) configurations relative to the clean airfoil, computed for varying heat exchanger porosities.

Moreover, the secondary flow structures in the junction appear to have minimal impact on the duct mass flow rate, as observed in Figure 5.1c, since it is mainly determined by the pressure differential across the heat exchanger. Although the trailing lower leg of the HSV may enter the duct for high porosity, it does not appear to significantly affect the mass flow rate. The relatively constant mass flow rate across different porosity levels indicates that external aerodynamics has minimal influence. Therefore, the presence of the nacelle is not expected to impact the thermal efficiency of the cooling installation. In the following sections, the changes in HSV size, strength, location, and corner flow separation are qualitatively analyzed to further understand the impact of heat exchanger induced flow resistance on the overall aerodynamic performance of the ducted wing.

5.2. THE EFFECT OF HEAT EXCHANGER POROSITY ON HORSESHOE VORTEX FORMATION

This section qualitatively analyzes the impact of heat exchanger-induced flow resistance on the HSV's size, strength, and location, providing further insight into the junction flow behavior of a ducted wing with integrated heat exchangers mounted perpendicularly on a flat plate. First, in Section 5.2.1, the development of the approach boundary layer and its sensitivity to variations in heat exchanger porosity are investigated. Then, Section 5.2.2 presents total pressure contours in the junction region and downstream wake to identify regions of energy losses associated with HSV formation in both clean and ducted wing configurations. To further characterize the HSV, Section 5.2.3 analyzes the vorticity field, while Section 5.2.4 investigates the crossflow velocity contours, both of which provide insight into HSV strength (circulation) and structure. Additional data on the turbulent kinetic energy within the junction region is provided in Section B.5. By systematically investigating these aspects, the impact of heat exchanger-induced flow resistance on HSV formation can be better understood, providing insights into its effects on the overall aerodynamics of the simplified nacelle/ducted-wing configuration.

5.2.1. UPSTREAM BOUNDARY LAYER DEVELOPMENT

The formation of secondary vortical structures in the junction region depends on the Reynolds number (Re_θ), computed based on the momentum thickness of the incoming boundary layer, and is quantified using the MDF (Equation 2.7), as defined by Fleming *et al.* [38]. Therefore, the incoming boundary layer over the flat plate must be sufficiently developed before interacting with the ducted wing to capture the formation of secondary vortical structures in the junction region.

To accurately assess the boundary layer behavior at the junction, the flat plate boundary layer development is first analyzed without the presence of the wing. The objective is to establish a fully turbulent and sufficiently thick incoming boundary layer. As observed in the computational domain in Figure 3.6, the no-slip boundary condition is imposed over a total distance of $2.5c$, consisting of $1c$ upstream of the wing's leading-edge, $1c$ along the wing attachment region, and $0.5c$ downstream of the trailing-edge. This boundary condition ensures that the fluid adheres to the solid surface due to viscous effects, with velocity gradually increasing from zero at the wall to the freestream value. The resulting velocity profile consists of a thin region of retarded flow near the wall dominated by viscous forces, transitioning to an outer region where inertial effects prevail.

The streamwise velocity profiles of the boundary layer developed along the entire flat plate, extracted from the symmetry plane ($y = 0$), are presented in Figure 5.2b. The local velocity u

at a given distance from the wall is normalized by the freestream velocity V_∞. Similarly, the distance from the wall z is normalized by the boundary layer thickness δ measured at the final station on the flat plate. The red-marked velocity profile, taken at station $x/c = 0$, represents the flow conditions at the leading-edge of the ducted wing. The computed local Reynolds number at this station is $Re_x \approx 4.8 \times 10^6$, which is well beyond the critical Reynolds number for a flat plate $Re_{cr} \approx 5 \times 10^5$, indicative of the presence of a fully developed turbulent boundary layer. The estimated boundary layer thickness δ is 0.0172 m. Furthermore, the near-wall resolution is validated by inspecting the wall-law profile at station $x/c = 0$, as shown in Figure 5.2a. The non-dimensional velocity is defined as:

$$u^+ = \frac{u}{u_\tau} \tag{5.1}$$

where u is the local velocity parallel to the wall and u_τ is the friction velocity as defined in Equation 3.10. The result in Figure 5.2a show good agreement with empirical flat plate experimental data, confirming that the turbulent boundary layer is accurately captured and resolved down to the viscous sublayer ($y^+ \leq 1$). This simple flat plate analysis provides a valuable reference for assessing the boundary layer thickness and turbulence state before its interaction with the ducted wing. In this study, the flat plate extends one chord length upstream of the wing, as detailed in Section 3.5.2. Variations in this distance were not considered, and its impact on boundary layer thickness was not assessed under the same operating conditions. Nevertheless, the current setup effectively generates strong secondary vortical structures in the junction, allowing for a detailed analysis of the simplified nacelle/wing-integrated duct model and the impact of heat exchanger flow resistance on the junction flow characteristics.

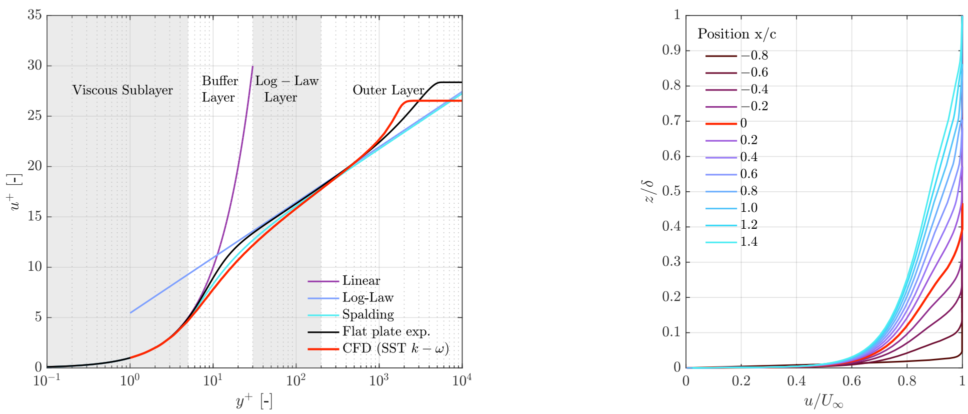

(a) Wall-law profile: non-dimensional velocity u^+ and wall distance y^+ at station $x/c = 0$

(b) Streamwise velocity profiles of the boundary layer over a flat plate

Figure 5.2: Comparison of CFD results (SST $k-\omega$) with theoretical models for the turbulent boundary layer at the ducted-wing inlet.

The boundary layer development upstream of both the clean and ducted wing mounted on the flat plate is compared at low and high angles of attack in Figs. 5.3 and 5.4, respectively. For the ducted wing housing the heat exchanger, the impact of porosity on boundary layer development is also included. For all cases, as the velocity profiles approach the wing, the flow slows down, indicated by the decrease in u/V_∞. For the clean wing, at a high angle of attack, the boundary layer separates earlier compared to lower angle of attack, as seen by the flow reversal near the wall at the last three locations ($x/c = -0.05, -0.02, -0.01$), due to the stronger adverse pressure gradient induced by the wing. Furthermore, the impact of heat exchanger-induced flow resistance extends upstream, affecting the boundary layer well before reaching the ducted wing due to the redistribution of pressure associated with variations in flow resistance. Notable effects of heat exchanger porosity on the incoming boundary layer are observed at stations ($x/c = -0.1, -0.05$). At a low angle of attack, as shown in Figure 5.3, a higher porosity–corresponding to lower flow resistance–results in a fuller boundary layer due to increased momentum entrainment. This occurs as more mass flow passes through the duct, and the reduced stagnation pressure at the leading-edge relative to the clean wing further influences the boundary layer development. At a higher angle of attack, as depicted in Figure 5.4, the same trend is present but to a lesser extent. Additionally, flow separation is observed at $x/c = -0.05$, though its magnitude remains comparable to that of the clean wing.

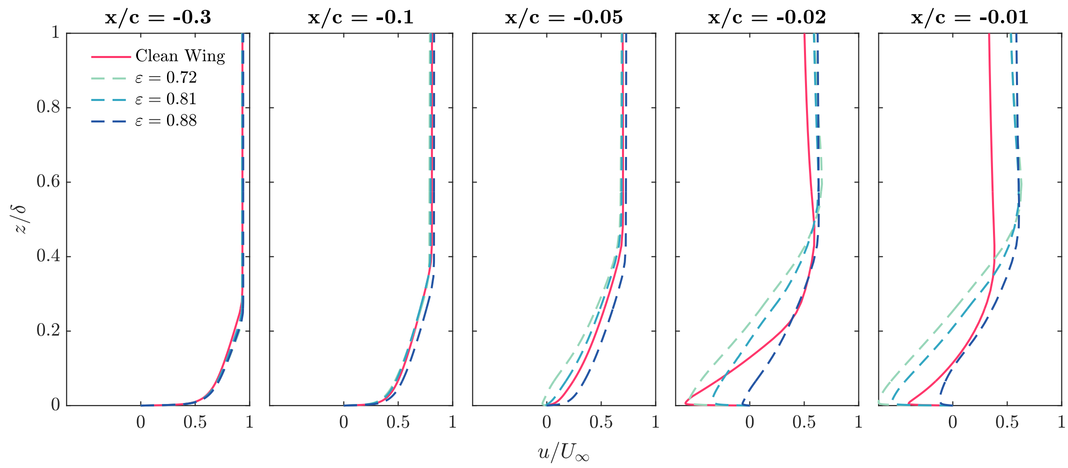

Figure 5.3: Boundary layer development at various upstream locations, computed for a low angle of attack ($\alpha = 2°$).

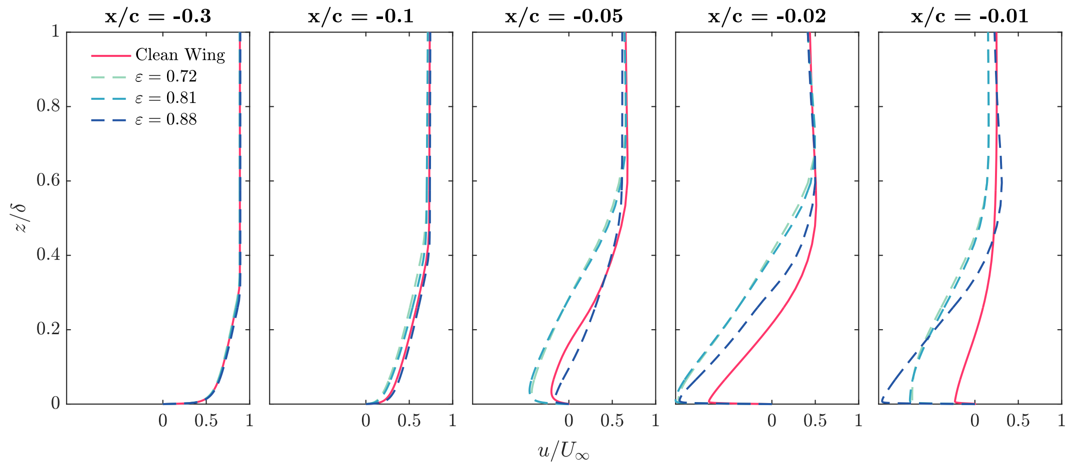

Figure 5.4: Boundary layer development at various upstream locations, computed for a high angle of attack ($\alpha = 10°$).

Furthermore, lower porosity–associated with higher flow resistance–induces a pressure rise ahead of the duct resulting in a larger boundary layer momentum deficit, preventing sustained wall attachment and causing earlier separation. At the last two stations ($x/c = -0.02, -0.01$), flow separation is apparent for both angles of attack. However, as these locations lie within the developing HSV region, the observed separation may also be influenced by vortex induced flow interactions rather than purely by the upstream adverse pressure gradient. Nevertheless, the presence of the heat exchanger and the associated porosity exacerbates adverse effects on boundary layer behavior. These observations are important, as the increased boundary layer momentum deficit associated with higher flow resistance directly affects the Reynolds number based on momentum thickness (Re_θ) and increases the MDF. As a result, this further strengthens and changes the topology of the HSV, reinforcing its influence on junction flow dynamics.

5.2.2. Total pressure ratio

To investigate the mean flow quantities in the junction region, contours of mean total pressure, vorticity, and turbulent kinetic energy are analyzed at selected streamwise locations. Streamwise slices are taken at $x/c = 0.5$, 1.0, and 1.5 to capture the progression of secondary flow structures along the wing, as depicted in Figure 5.5. The first two locations correspond to the midsection and trailing-edge of the wing, while the last location is placed further downstream in the wake. These contours are compared for both the clean wing and the ducted wing configuration, considering different heat exchanger porosities. The contour levels remain consistent within each streamwise plane to ensure a direct comparison between cases. Note that at the first streamwise slice, located at the midsection of the wing, the blank regions in the contour plots represent areas covered by the wing structure. The same setup is applied for analyzing the vorticity field and turbulent kinetic energy contours, as presented in Sections 5.2.3 and B.5, respectively.

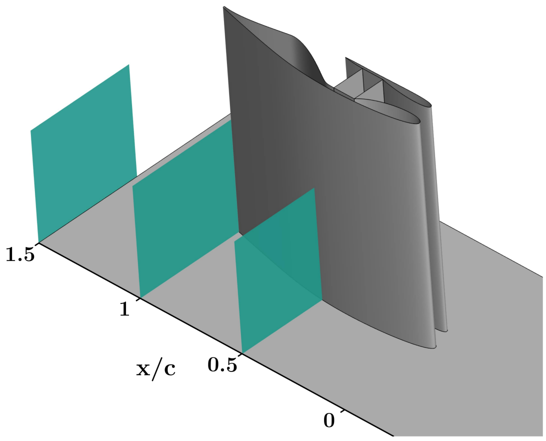

Figure 5.5: Overview of streamwise slices in the nacelle/ducted-wing CFD model, positioned along the wing and in the wake.

The three-dimensional effects due to HSV formation in the junction region, along with local flow curvature, contribute to pressure losses that are directly influenced by boundary layer behavior, vortex interactions, and turbulence generation. As observed in Figs. 5.6 – 5.8, at a low angle of attack, the HSV is apparent by a noticeable protrusion, while the flow remains largely attached with minimal separation at the junction. The pressure losses are primarily associated with streamwise boundary layer growth, the weak HSV, and the nascent wake development. For lower heat exchanger porosity, the pressure losses associated with the reinforced HSV increase slightly due to the greater flow restriction through the duct. Vice-versa, a higher porosity slightly reduces total pressure losses by allowing more airflow through the matrix core, which mitigates stagnation effects.

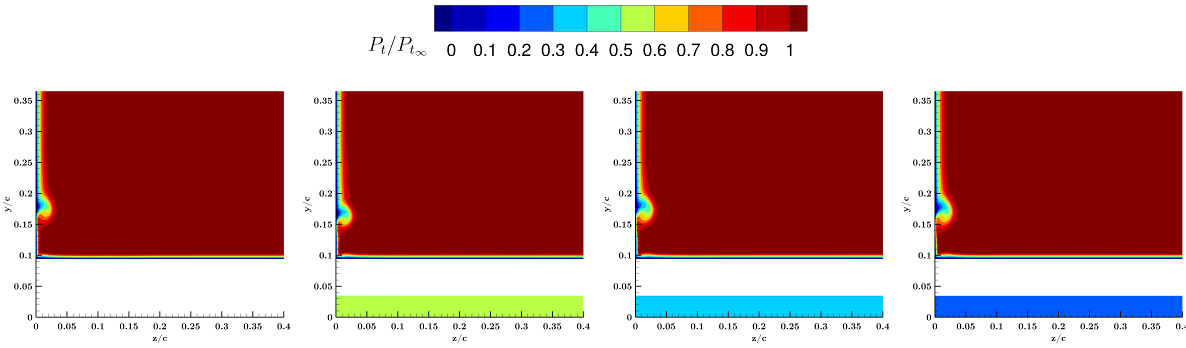

(a) Clean wing (b) HX porosity $\varepsilon = 0.88$ (c) HX porosity $\varepsilon = 0.81$ (d) HX porosity $\varepsilon = 0.72$

Figure 5.6: Contours of total pressure ratio in the plane at $x/c = 0.5$, computed for $\alpha = 2°$.

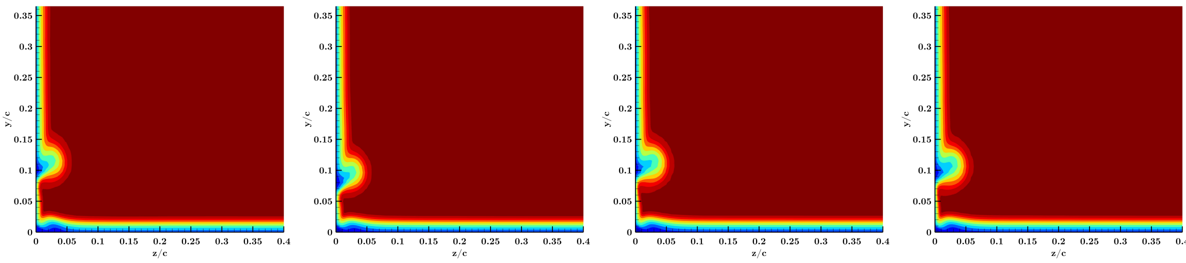

(a) Clean wing (b) HX porosity $\varepsilon = 0.88$ (c) HX porosity $\varepsilon = 0.81$ (d) HX porosity $\varepsilon = 0.72$

Figure 5.7: Contours of total pressure ratio in the plane at $x/c = 1$, computed for $\alpha = 2°$.

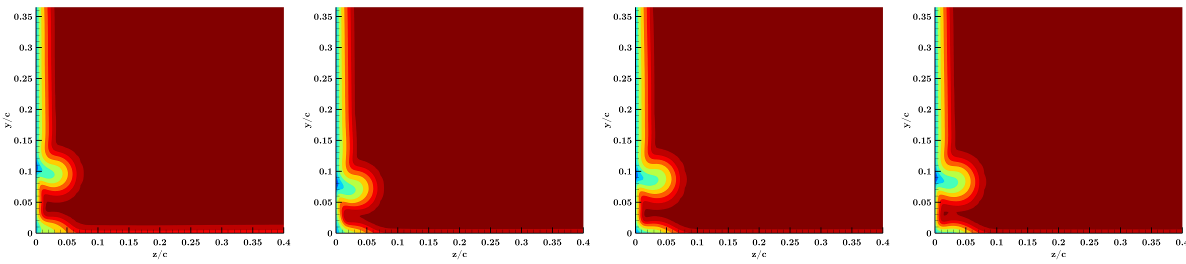

(a) Clean wing (b) HX porosity $\varepsilon = 0.88$ (c) HX porosity $\varepsilon = 0.81$ (d) HX porosity $\varepsilon = 0.72$

Figure 5.8: Contours of total pressure ratio in the plane at $x/c = 1.5$, computed for $\alpha = 2°$.

At a high angle of attack, the junction flow behavior changes significantly, as indicated by increased pressure losses due to stronger vortex formation and interactions, as observed in Figs. 5.9 – 5.11. At the midsection of the clean wing in Figure 5.9a, the larger HSV footprint results from a stronger upstream adverse pressure gradient, leading to the reinforcement of the HSV, while its vertical extent above the wing is attributed to the pressure distribution. Furthermore, decreasing heat exchanger porosity in the ducted wing strengthens the HSV further, as the increased flow resistance increases the adverse pressure gradient ahead of the wing further, resulting in a higher MDF. Additionally, the vortex legs move further apart in the vertical direction, a similar observation reported by Fleming *et al.* [38] and Simpson [33]. Furthermore, the increased momentum redistribution within the spanwise and streamwise boundary layers in the junction region due to vortex interactions leads to corner flow separation, as observed at the trailing-edge location. Although marginal corner separation is also present in the clean wing junction, the presence of the wing-integrated duct exacerbates this effect, leading to more pronounced separation. Particularly, at a high porosity level, the increased flow passing through the matrix core in the duct alters the junction flow dynamics. Albeit, the HSV is slightly located closer to the wing compared to lower porosity levels, its relatively reduced strength is insufficient to entrain high-momentum fluid into the boundary layer. Moreover, at lower porosity levels, the trailing upper leg of the HSV extends further vertically, its higher strength entrain greater momentum into the boundary layer, leading to lower pressure losses.

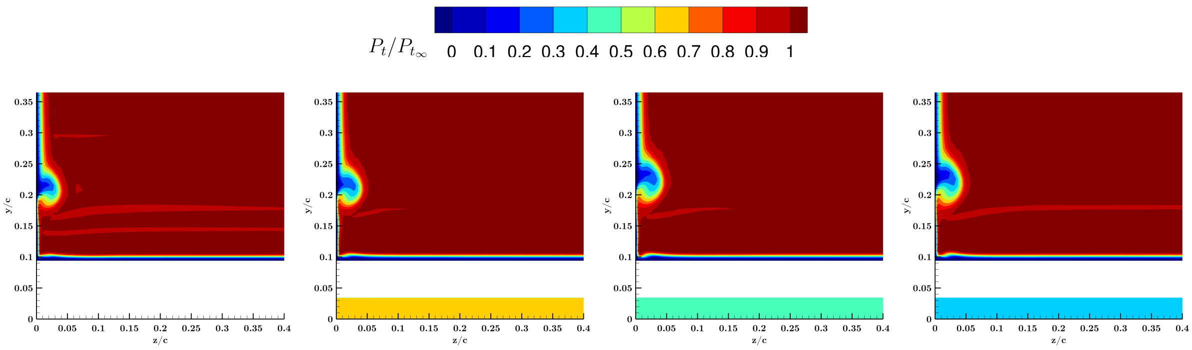

(a) Clean wing (b) HX porosity $\varepsilon = 0.88$ (c) HX porosity $\varepsilon = 0.81$ (d) HX porosity $\varepsilon = 0.72$

Figure 5.9: Contours of total pressure ratio in the plane at $x/c = 0.5$, computed for $\alpha = 10°$.

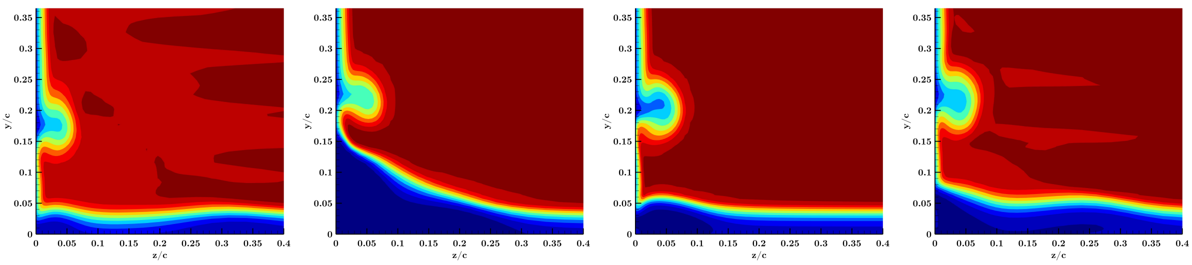

(a) Clean wing (b) HX porosity $\varepsilon = 0.88$ (c) HX porosity $\varepsilon = 0.81$ (d) HX porosity $\varepsilon = 0.72$

Figure 5.10: Contours of total pressure ratio in the plane at $x/c = 1$, computed for $\alpha = 10°$.

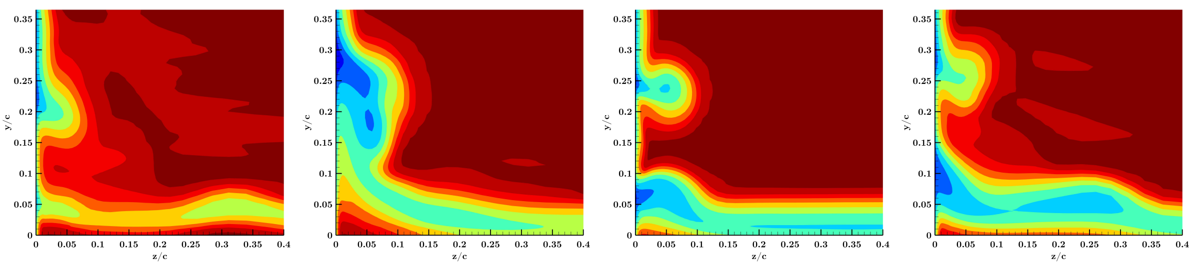

(a) Clean wing (b) HX porosity $\varepsilon = 0.88$ (c) HX porosity $\varepsilon = 0.81$ (d) HX porosity $\varepsilon = 0.72$

Figure 5.11: Contours of total pressure ratio in the plane at $x/c = 1.5$, computed for $\alpha = 10°$.

Furthermore, to better envision the full flow topology at the junction and its impact on wake development, isometric views of the clean and ducted wing CFD models are shown in Figs. 5.12 and 5.13 for low and high angles of attack, respectively. The pressure losses and 3D streamlines provide more insight into the HSV interaction in the junction, corner flow separation, and wake dissipation. At a low angle of attack, the wake remains relatively organized, with the clean wing showing a gradual momentum deficit that recovers quickly. However, for the ducted wing, the momentum deficit varies with heat exchanger porosity, recovering more slowly at lower porosity levels due to greater turbulence and shear-induced energy losses. As previously noted, minimal flow separation occurs at this angle of attack, resulting in limited pressure losses.

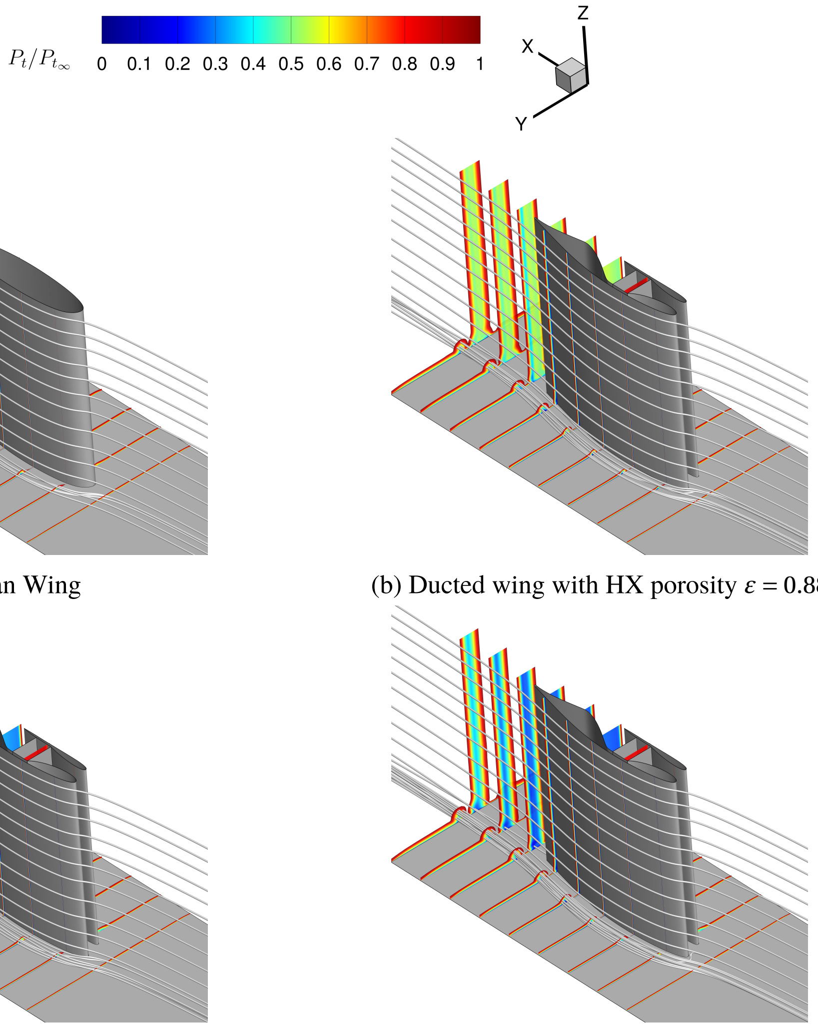

(a) Clean Wing

(b) Ducted wing with HX porosity $\varepsilon = 0.88$

(c) Ducted wing with HX porosity $\varepsilon = 0.81$

(d) Ducted wing with HX porosity $\varepsilon = 0.72$

Figure 5.12: Isometric view of the clean and ducted wing CFD model, illustrating total pressure ratio contours at multiple streamwise slices and 3D streamlines to visualize the effect of porosity variations on the flow field at a low angle of attack ($\alpha = 2°$).

At a high angle of attack, wake development becomes increasingly chaotic and unsteady. The stronger upstream adverse pressure gradient leads to stronger secondary flow structures at the junction, promoting corner flow separation, as previously discussed. In the low-porosity case, where flow restriction is highest, the stronger HSV, positioned higher above the wing surface, fails to impart sufficient momentum into the boundary layer, leading to corner separation and increased overall pressure losses. Vice-versa, in the high-porosity case, while the HSV remains relatively closer to the wing, its lower strength limits its ability to stabilize the boundary layer, resulting in increased pressure losses and a more unstable wake.

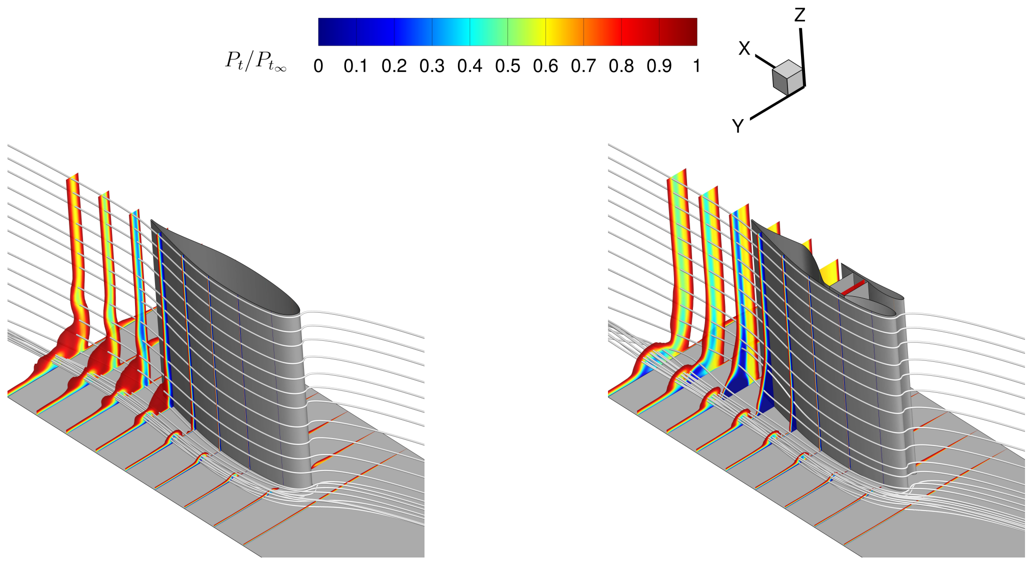

(a) Clean Wing

(b) Ducted wing with HX porosity $\varepsilon = 0.88$

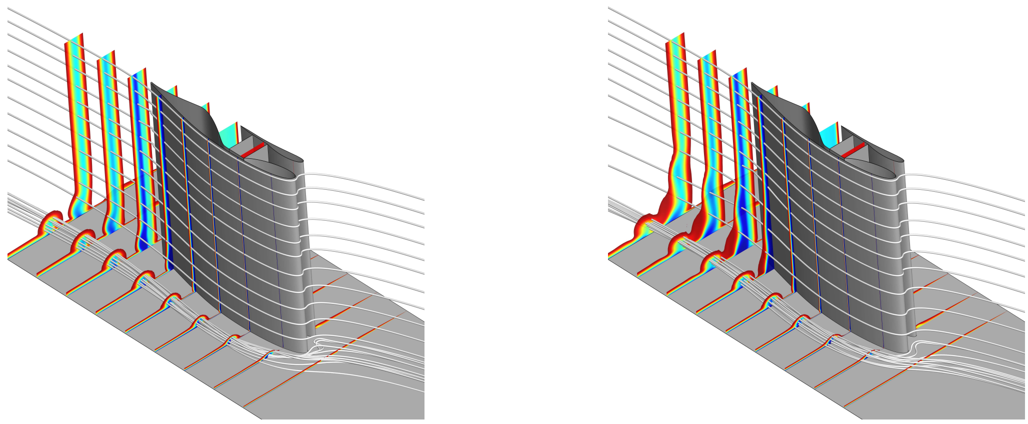

(c) Ducted wing with HX porosity $\varepsilon = 0.81$

(d) Ducted wing with HX porosity $\varepsilon = 0.72$

Figure 5.13: Isometric view of the clean and ducted wing CFD model, illustrating total pressure ratio contours at multiple streamwise slices and 3D streamlines to visualize the effect of porosity variations on the flow field at a high angle of attack ($\alpha = 10°$).

5.2.3. VORTICITY FIELD

To further characterize the HSV, the streamwise vorticity ω_x component is analyzed in the junction region. The streamwise vorticity is expressed in its dimensionless form using the chord length c and the freestream velocity V_∞, allowing for a consistent gauging of vortex strength across different cases. As observed in the contour plots below, the HSV flow structures are well captured by the RANS simulations. The boundary layer on the wing shows a thin layer of positive vorticity, due to the strong velocity gradients characteristic of viscous-dominated regions. In Figs. 5.14 and 5.17, the HSV is recognizable by the elliptical region of strong positive vorticity. Due to the sharp velocity gradients at the upper boundary of the vortex, a thin secondary shear layer of negative vorticity forms above the HSV core. As noted in the pressure loss analysis, the HSV reaches its peak vorticity at low porosity levels. Additionally, the vertical displacement of the trailing upper leg of the HSV relative to the wing surface is clearly observed.

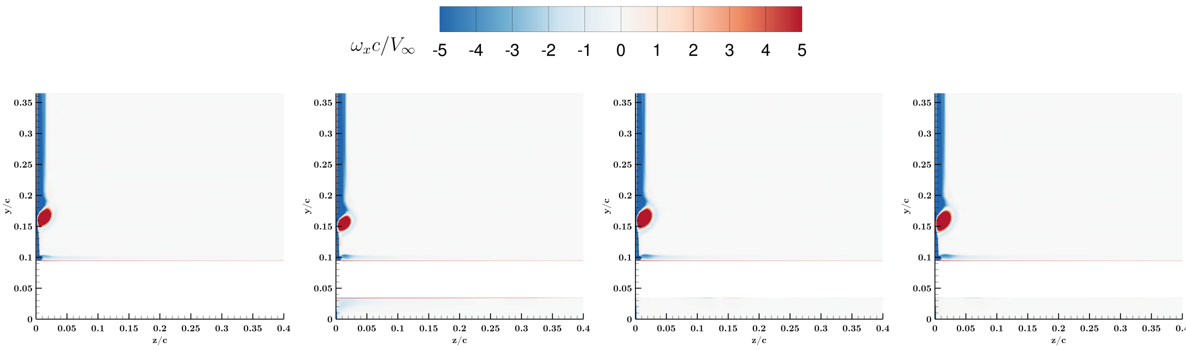

(a) Clean wing (b) HX porosity $\varepsilon = 0.88$ (c) HX porosity $\varepsilon = 0.81$ (d) HX porosity $\varepsilon = 0.72$

Figure 5.14: Contours of non-dimensional vorticity in the plane at $x/c = 0.5$, computed for $\alpha = 2°$.

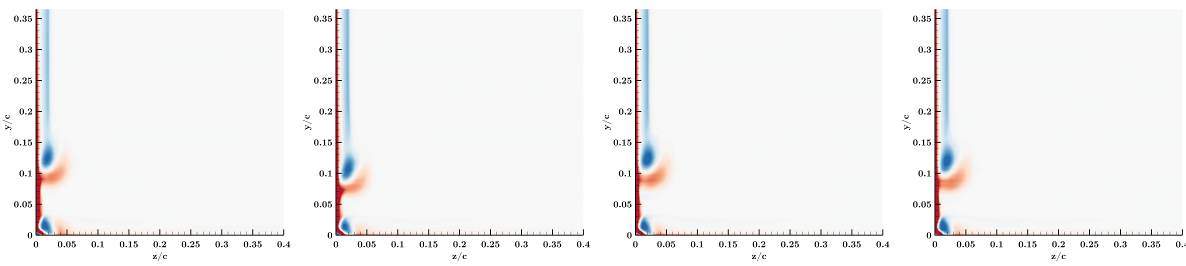

(a) Clean wing (b) HX porosity $\varepsilon = 0.88$ (c) HX porosity $\varepsilon = 0.81$ (d) HX porosity $\varepsilon = 0.72$

Figure 5.15: Contours of non-dimensional vorticity in the plane at $x/c = 1$, computed for $\alpha = 2°$.

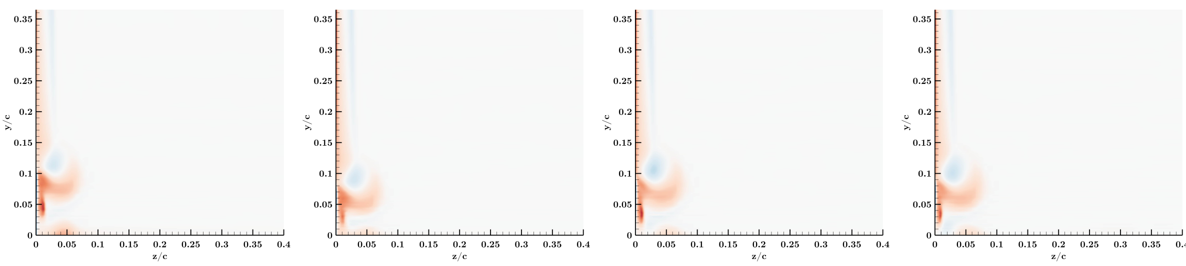

(a) Clean wing (b) HX porosity $\varepsilon = 0.88$ (c) HX porosity $\varepsilon = 0.81$ (d) HX porosity $\varepsilon = 0.72$

Figure 5.16: Contours of non-dimensional vorticity in the plane at $x/c = 1.5$, computed for $\alpha = 2°$.

Furthermore, as the HSV convects downstream, viscous diffusion and vortex stretching contribute to the redistribution and attenuation of the vorticity field. Higher porosity enhances viscous diffusion, accelerating the attenuation of vortex intensity, as observed in the HSV footprint in Figure 5.16. At this low angle of attack, no major corner flow separation occurs, resulting in weak wake structures where streamwise vorticity has largely dissipated. Additionally, at a high angle of attack, the HSV shows a larger magnitude in size, strength (circulation) and shifts higher compared to the low angle of attack, as seen in Figure 5.17. However, while this vertical displacement of the HSV is apparent, the relative shift between low and high porosity cases at high angles of attack remains marginal, as observed before. Moreover, due to large corner flow separation, the wake shows stronger vortex structures which generates additional vorticity that is convected downstream, especially for a high porosity level. The increased separation induces a more unstable wake, leading to intensified streamwise vorticity.

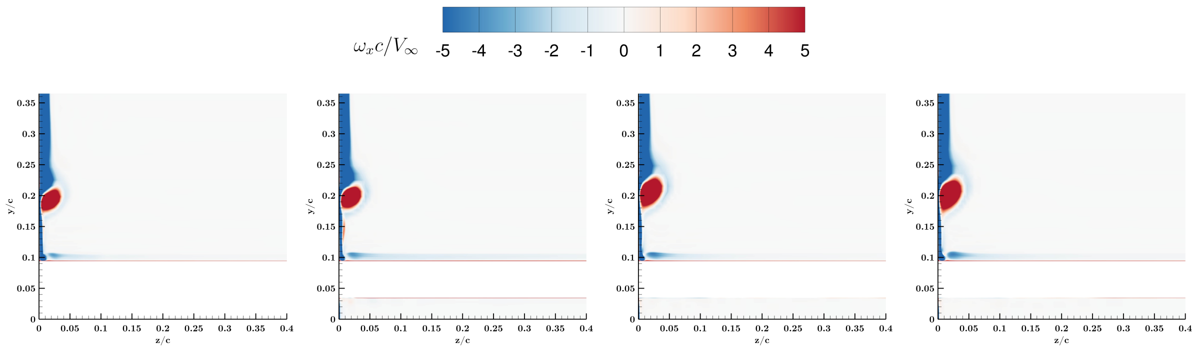

(a) Clean wing (b) HX porosity $\varepsilon = 0.88$ (c) HX porosity $\varepsilon = 0.81$ (d) HX porosity $\varepsilon = 0.72$

Figure 5.17: Contours of non-dimensional vorticity in the plane at $x/c = 0.5$, computed for $\alpha = 10°$.

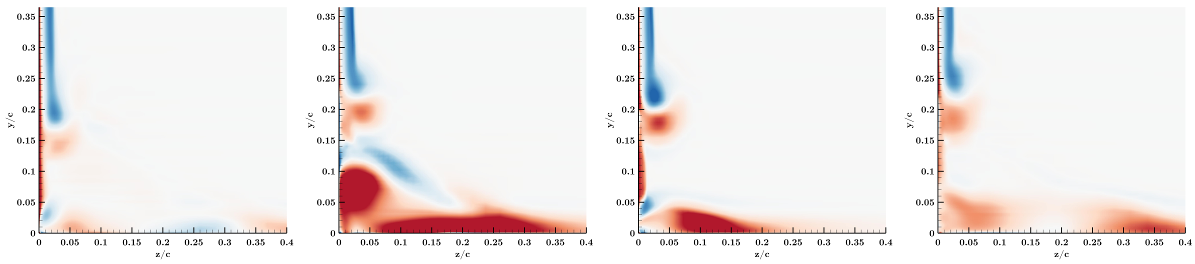

(a) Clean wing (b) HX porosity $\varepsilon = 0.88$ (c) HX porosity $\varepsilon = 0.81$ (d) HX porosity $\varepsilon = 0.72$

Figure 5.18: Contours of non-dimensional vorticity in the plane at $x/c = 1$, computed for $\alpha = 10°$.

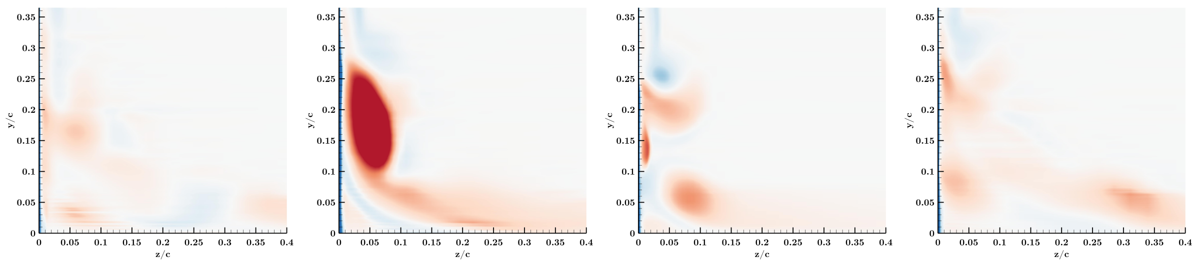

(a) Clean wing (b) HX porosity $\varepsilon = 0.88$ (c) HX porosity $\varepsilon = 0.81$ (d) HX porosity $\varepsilon = 0.72$

Figure 5.19: Contours of non-dimensional vorticity in the plane at $x/c = 1.5$, computed for $\alpha = 10°$.

5.2.4. CROSSFLOW VELOCITY FIELD

The downstream convection of the trailing legs of the HSV is further analyzed by inspecting the crossflow velocity field, providing more insights into the near-wall dynamics of the secondary flow structures across different porosity levels at both low and high angles of attack. To quantify this behavior, the crossflow velocity v is non-dimensionalized by the freestream velocity V_∞ in the plane at $z/c = 0.01$ within the junction region. As observed in Figs. 5.20 and 5.21, the HSV originates upstream of the wing, while its trailing legs wrap around the wing and convect downstream with the freestream flow, showing variations in strength and topology across different heat exchanger porosity levels. The white line indicate the vortex core, around which the flow circulates. The red regions in the plot represent flow moving in the positive spanwise direction, while the green regions indicate flow moving in the opposite direction, toward the flat plate. This opposing motion generates a region of high shear stress at the flat plate due to intense back-flow. Furthermore, it can be observed that at high porosity, the HSV originates closer to the leading-edge due to the lower flow resistance in the duct, while low porosity shifts its formation further upstream.

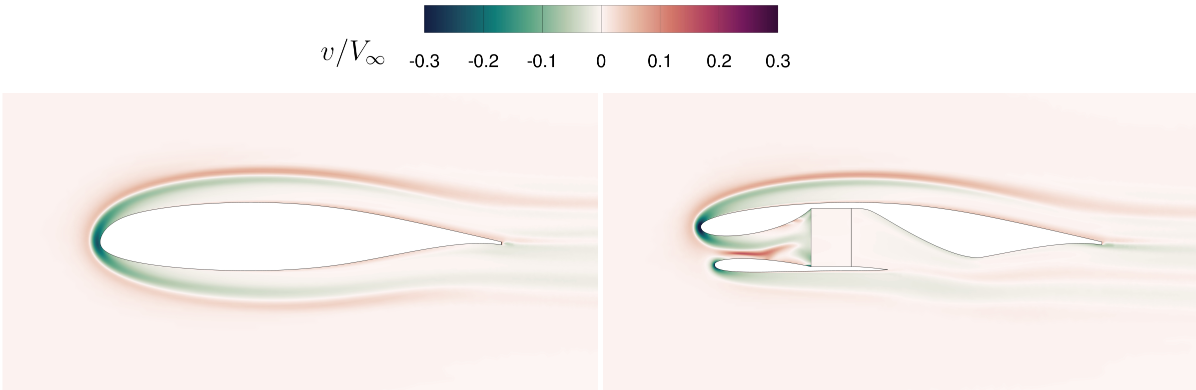

(a) Clean wing

(b) HX porosity $\varepsilon = 0.88$

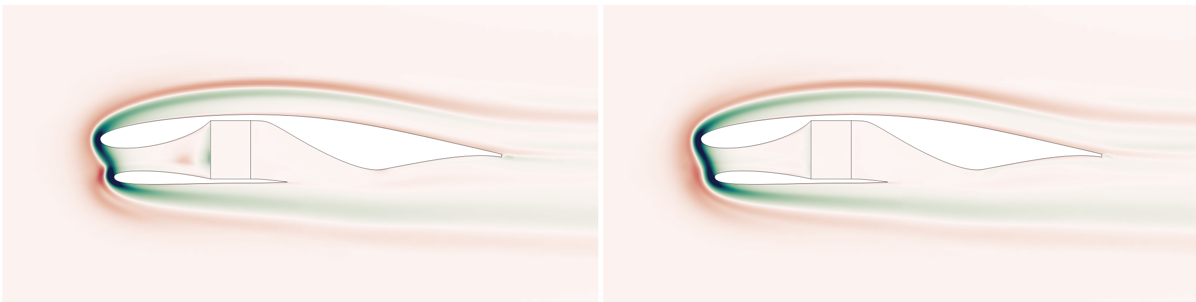

(c) HX porosity $\varepsilon = 0.81$

(d) HX porosity $\varepsilon = 0.72$

Figure 5.20: Contours of non-dimensional crossflow velocity (v/V_∞) in the plane at $z/c = 0.01$ within the junction region, for $\alpha = 2°$.

By comparing the trailing legs of the HSV around the clean wing at low and high angles of attack, as shown in Figs. 5.20a and 5.21a, the difference in vertical displacement above the wing is apparent, as noted earlier. The upper trailing leg of the HSV extends higher at a high angle of attack, where the MDF is greater due to the increased momentum deficit in the incoming boundary layer, compared to a low angle of attack. Furthermore, the intricate inlet geometry of the ducted wing alters the HSV topology at the junction, depending on the heat exchanger porosity inside the duct. An interesting observation is that, at low porosity, the high flow restriction inside the duct prevents the HSV from entering, causing it to be deflected and convected around the wing instead, as seen in Figs. 5.20d and 5.21d. For a slightly higher porosity, as shown in Figs. 5.20c and 5.21c, there is a slight tendency for the HSV to split and partially enter the duct. This effect is more pronounced at a lower angle of attack, where the relative reduced flow restriction allows part of the vortex to be entrained into the duct flow. Furthermore, for the highest porosity case in this study, the low flow resistance allows HSV to enter the duct, as observed in Figs 5.20b and 5.21b. Additionally, the lower lip shows a tendency to generate a smaller secondary HSV, though it remains significantly weaker than the primary vortex associated with the upper element. This altered vortex topology is particularly apparent at high angles of attack, where the increased interaction between the vortices and the junction region leads to major corner flow separation. This can be attributed to the weaker HSV, which fails to impart sufficient momentum into the boundary layer at the corner, reducing its resistance to the adverse pressure gradient and ultimately causing corner flow separation. Furthermore, the increased angle of attack aggravate the adverse pressure gradient in the junction region, while the proximity of the HSV plays a stabilizing role in preventing corner separation. At higher angles of attack, its displacement away from the wing surface removes this stabilizing effect, making the corner region more susceptible to separation. The impact of heat exchanger porosity on corner flow separation is further detailed in Section 5.3.

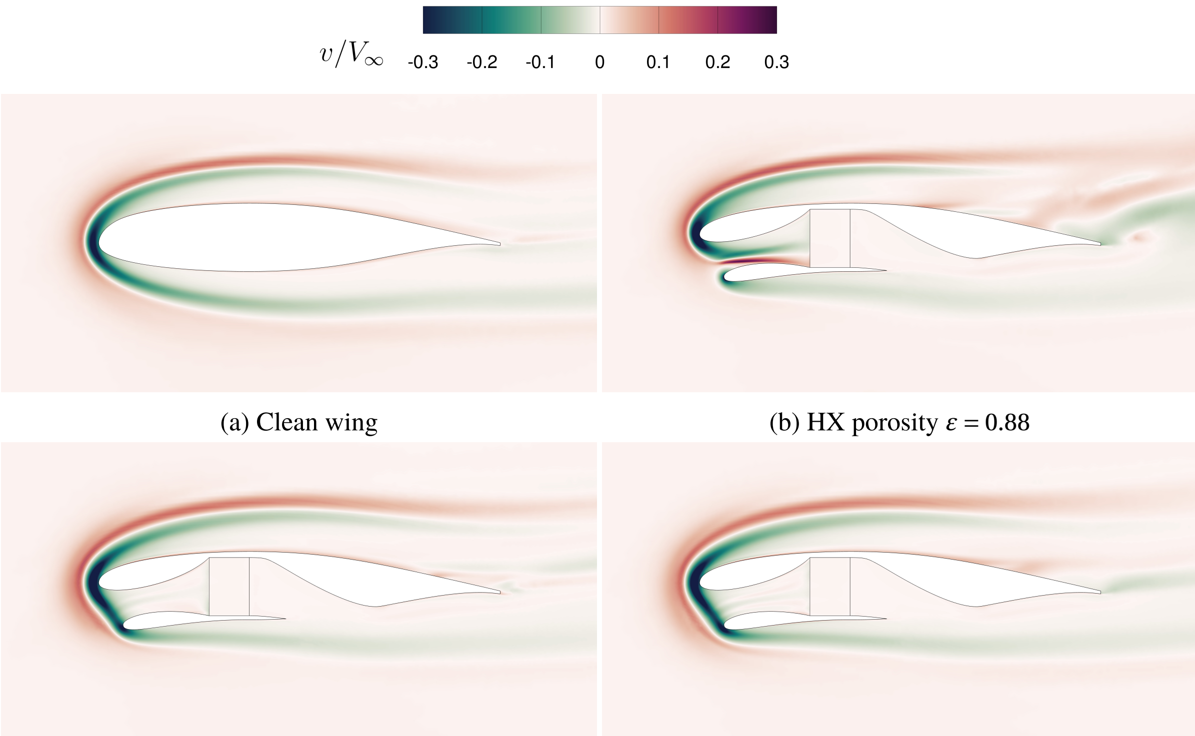

(a) Clean wing

(b) HX porosity $\varepsilon = 0.88$

(c) HX porosity $\varepsilon = 0.81$

(d) HX porosity $\varepsilon = 0.72$

Figure 5.21: Contours of non-dimensional crossflow velocity (v/V_∞) in the plane at $z/c = 0.01$ within the junction region, for $\alpha = 10°$.

5.3. The effect of heat exchanger porosity on corner flow separation

Corner flow separation near the intersection of the junction is classified as a secondary flow of Prandtl's second kind [33]. This separation occurs due to the combined effects of adverse pressure gradients in both the streamwise and spanwise directions, which results from secondary vortical structures and are further influenced by heat exchanger induced flow resistance. To scrutinize corner flow separation, wall shear stress surface streamlines are plotted in Figs. 5.22 and 5.24 for low and high angles of attack, respectively. In addition, to identify regions of back-flow, isosurfaces of the back-flow coefficient are shown in Figs. 5.23 and 5.25.

At a low angle of attack, again, the flow remains largely attached in the junction region, with only minor disturbances induced by the HSV. The surface streamlines indicate relatively smooth flow over the clean and ducted wing, with a weak HSV forming at the leading-edge. A distinct separation line is observed on the flat plate, along which the HSV is convected downstream. As discussed earlier, although the increased flow resistance associated with decreasing heat exchanger porosity leads to a local pressure rise upstream of the duct, the corner flow remains relatively stable. No significant separation regions are observed in the back-flow coefficient iso-surfaces shown in Figure 5.23. However, as expected, some back-flow occurs behind the sharp square trailing-edge due to minor flow-reversal.

Moreover, at a higher angle of attack, the impact of the HSV on corner flow separation becomes more pronounced. The surface streamlines indicate regions of localized recirculation over the aft part of the clean and ducted wing configurations, as shown in Figure 5.24. For the clean wing, corner flow separation remains marginal, with only minor recirculation zones forming near the trailing-edge due to HSV-induced momentum redistribution within the boundary layer. The back-flow coefficient iso-surface in Figure 5.25a confirm the absence of significant separated regions. However, for the ducted wing configurations, the reinforced HSV, affected by the inlet geometry and flow restriction within the duct, enhances its interaction in the junction, resulting in an earlier onset of corner flow separation. For a low-porosity heat exchanger ($\varepsilon = 0.72$), the high flow resistance in the duct prevents the HSV from entering, forcing it to wrap around the wing-body junction and convect downstream with increased vorticity. As a result, the HSV strength and vertical extend above the wing lead to a momentum deficit in the junction boundary layers rather than entraining high-momentum freestream air. This causes boundary layer thickening, increasing its susceptibility to flow separation, as shown by the surface streamlines in Figure 5.24d and the back-flow iso-surface Figure 5.25d. An interesting observation is that at a slightly higher porosity ($\varepsilon = 0.81$), despite the strong HSV being forced to wrap around the wing-body junction, the lower flow resistance in the duct alters upstream stagnation effects and redistributes momentum in the junction due to its lower vertical extend above the wing. This redistribution appears to mitigate corner separation, as evidenced by the smaller separation region in Figure 5.25c. Furthermore, for the highest-porosity heat exchanger ($\varepsilon = 0.88$), the separated flow regions, as shown in Figs. 5.24b and 5.25b, persist downstream due to the weaker HSV. While the HSV partially enters the duct, the lower flow resistance prevents it from entraining sufficient momentum into the junction. This contributes to increased wake turbulence and aerodynamic losses, aligning with the pressure loss trends observed in previous sections.

While the results provide insight into the mechanisms of corner flow separation, it is important to recognize the limitations of RANS-based turbulence models in capturing this phenomenon accurately. Previous studies [35, 60, 61] have shown that RANS models often fail to reproduce corner separation due to the high anisotropy of the junction boundary layer, which is not well accounted for by linear EVMs relying on the Boussinesq hypothesis. RSMs, which directly solve for the Reynolds stresses, offer better predictive capability in corner regions. Additionally, Gand *et al.* [60] reported that experimental investigations at lower Reynolds numbers reported good agreement between experimental data and RANS simulations, with no significant corner flow separation observed in the experiments. However, in RANS simulations, corner separation was still present, suggesting a modeling limitation. Given that the current study operates at a higher Reynolds number, the presence of stronger adverse pressure gradients and increased turbulence anisotropy in the junction further complicates the reliability of RANS predictions in corner flow separation.

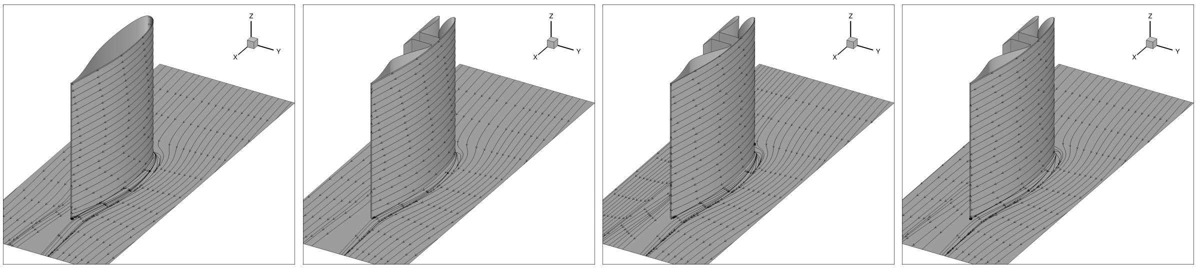

(a) Clean Wing (b) HX porosity $\varepsilon = 0.88$ (c) HX porosity $\varepsilon = 0.81$ (d) HX porosity $\varepsilon = 0.72$

Figure 5.22: Surface streamlines at the wing-body junction for clean and ducted wings at $\alpha = 2°$.

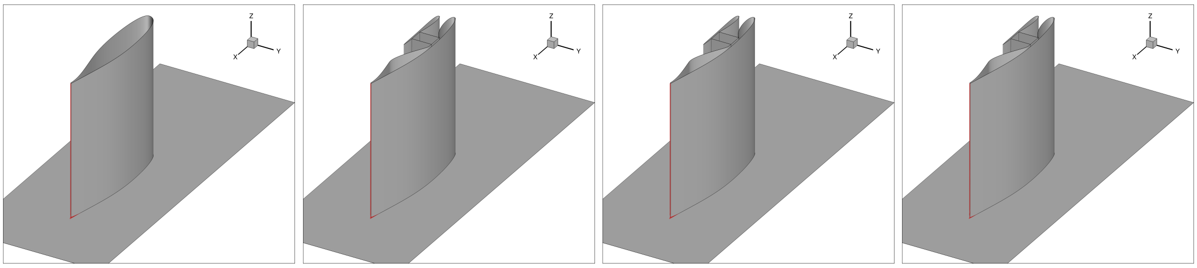

(a) Clean Wing (b) HX porosity $\varepsilon = 0.88$ (c) HX porosity $\varepsilon = 0.81$ (d) HX porosity $\varepsilon = 0.72$

Figure 5.23: Iso-surfaces of back-flow coefficient $(-u/V_\infty)$ indicating separation regions at $\alpha = 2°$.

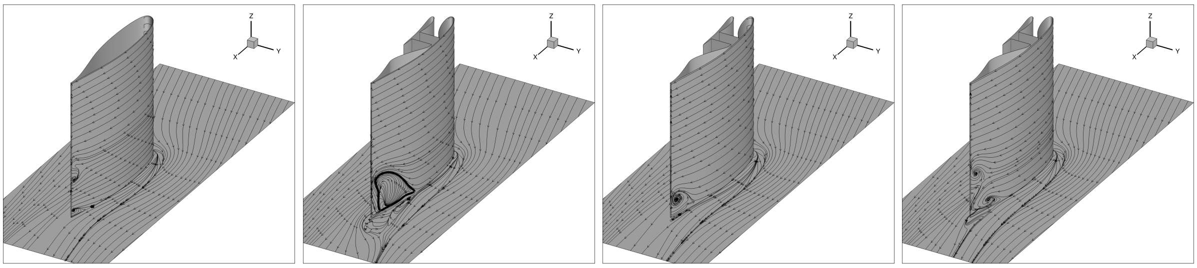

(a) Clean Wing (b) HX porosity $\varepsilon = 0.88$ (c) HX porosity $\varepsilon = 0.81$ (d) HX porosity $\varepsilon = 0.72$

Figure 5.24: Surface streamlines at the wing-body junction for clean and ducted wings at $\alpha = 10°$.

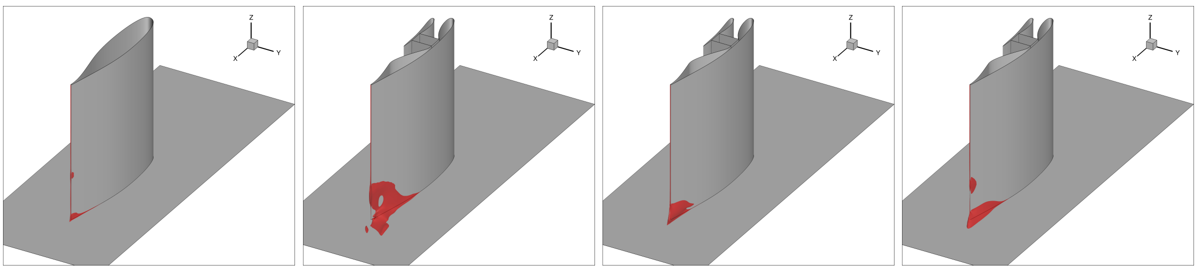

(a) Clean Wing (b) HX porosity $\varepsilon = 0.88$ (c) HX porosity $\varepsilon = 0.81$ (d) HX porosity $\varepsilon = 0.72$

Figure 5.25: Iso-surfaces of back-flow coefficient $(-u/V_\infty)$ indicating separation regions at $\alpha = 10°$.

5.4. CONCLUSIONS

In this chapter, the 3D aerodynamic performance of the simplified nacelle/ducted-wing configuration was analyzed under representative climb and cruise angles of attack, addressing the third research question **Q3**. The study focused on the aerodynamic interaction between the wing-integrated duct and the flat plate, particularly the impact of heat exchanger-induced flow restriction on HSV formation, corner flow separation, and overall aerodynamic performance. The conclusions drawn from this study are summarized below.

The heat exchanger porosity, and thus duct flow resistance, alters the incoming boundary layer characteristics and HSV strength (circulation). The boundary layer momentum deficit upstream of the wing increases with lower porosity values, resulting in a higher Reynolds number based on momentum thickness (Re_θ) and an increased MDF. This strengthens the HSV and increases its vertical extent from the wing surface. Conversely, at higher porosity levels, the HSV remains relatively weaker and shifts slightly away from the wing surface while partially entering the duct, affecting its ability to entrain high-momentum air in the junction region.

The topology of the HSV modulates the onset and extent of corner flow separation by altering the turbulent flow structure near the wing junction. At low porosity levels, the stronger HSV entrains more high-momentum freestream air into the junction boundary layer, mitigating separation to some extent. However, at high porosity levels, the weaker HSV fails to impart sufficient momentum to the boundary layer, thereby promoting earlier corner flow separation and increased aerodynamic losses. Interestingly, at an intermediate porosity level of 0.81, a balance is observed where the HSV remains strong enough to stabilize the boundary layer without excessively restricting duct flow, minimizing corner separation. This balance is achieved through sufficient vortex strength and an optimal vertical extent above the wing, effectively energizing the boundary layer.

Consequently, the heat exchanger-induced flow resistance has a strong impact on both lift and drag coefficients of the ducted wing. The HSV-induced downwash reduces the local effective angle of attack, decreasing local lift. In terms of drag, pressure drag from corner separation at high angles of attack increases due to the inability of the weaker HSV to stabilize the junction boundary layer. Additionally, HSV-induced downwash increases induced drag, while junction flow interactions contribute to interference drag, both adding to the overall aerodynamic penalty.

Furthermore, secondary flow structures in the junction region do not significantly affect the duct mass flow rate, as it is primarily governed by the pressure differential across the heat exchanger. The findings suggest that external aerodynamic interactions have a limited influence on the thermal efficiency of the cooling system, indicating that the nacelle's presence does not significantly degrade cooling performance.

These findings highlight the trade-offs associated with different heat exchanger porosity configurations. While higher porosity improves cooling performance and reduces cooling installation drag due to lower flow resistance, it also weakens the HSV in the nacelle/wing-integrated duct configuration and allows it to partially enter the duct, leading to greater corner flow separation and local aerodynamic losses in the junction region.

Part IV

Conclusions and recommendations

6

CONCLUSIONS

The research objective of this thesis is to get a fundamental understanding of the aerodynamic performance and flow characteristics of a wing-integrated ram-air duct housing a heat exchanger for propeller-driven aircraft through high-fidelity viscous RANS simulations. A sectional 2D study of the shoulder-inlet design concept for TMS was conducted, focusing on the aerodynamic implications of the heat exchanger flow resistance within the ducted wing. The primary motivation was to quantify the cooling installation drag introduced by this integration and assess the feasibility of achieving sufficient cooling capacity for fuel-cell systems, which require significant thermal management. Four different ducted airfoil configurations with varying outlet positions were analyzed using a DoE approach to evaluate the main and interaction effects of key geometrical parameters. Based on this analysis, an optimal configuration was selected, and the impact of thermal effects on aerodynamic performance was assessed. Subsequently, a 3D study was conducted on the optimal design to examine the junction flow phenomena between the flat plate and ducted wing, focusing on aerodynamic interference drag sources such as the HSV and corner flow separation, which appear to be directly influenced by the heat exchanger-induced flow resistance.

The 2D DoE analysis revealed that the leading-edge droop ratio, heat exchanger porosity, and thickness significantly impact the aerodynamic performance and duct mass flow. The droop ratio enhanced lift at higher angles of attack by moderating the upper surface suction peak, delaying inlet flow separation, and improving mass flow ingestion through better freestream alignment. Furthermore, heat exchanger porosity and thickness governed duct flow resistance, with reduced porosity and increased thickness increasing pressure losses, thus raising drag and lowering duct mass flow. Among the analyzed configurations, configuration *I-B*, with the duct outlet positioned aft of maximum thickness on the lower surface, was identified as the optimal design, balancing higher mass flow with better aerodynamic efficiency relative to the other configurations. However, it incurred a drag penalty of 4.6 times the clean airfoil at cruise and 1.7 times at climb. This expected drag penalty is associated with integrating a heat exchanger within the wing due to modifications to the reference airfoil geometry and increased flow resistance. Furthermore, thermal feasibility assessments indicated that the optimal *I-B* configuration with a heat exchanger thickness-to-chord ratio of 0.10, minimized aerodynamic penalties but fell short of the heat transfer area required for fuel-cell cooling. Increasing the thickness-to-chord ratio to 0.15 met thermal demands but raised drag to 5.2 times the clean airfoil at cruise and 2.1 times at climb. These results underscore the trade-off between aerodynamic efficiency and thermal feasibility, showing that while a thinner heat exchanger minimizes drag, a thicker core is necessary to meet the cooling requirements. However, for applications with lower cooling demands, such as conventional radiator-based thermal management systems, the thinner heat exchanger could be sufficient, allowing for lower aerodynamic penalties. This highlights the potential for tailoring the shoulder-inlet design concept to different propulsion architectures, optimizing the balance between aerodynamic efficiency and cooling capacity depending on system requirements.

The 3D aerodynamic analysis further highlighted interference drag resulting from nacelle/wing-integrated duct model junction flow, particularly due to the formation of secondary vortical structures such as the HSV and its impact on corner separation. Additionally, corner separation increases pressure drag due to larger separated flow regions and wake formation.

A key finding was the impact of heat exchanger porosity on HSV characteristics, including its circulation strength, size, and vertical extent above the wing. Lower porosity increased the adverse pressure gradient ahead of the duct, leading to a greater boundary layer momentum deficit and higher MDF values, which reinforced the HSV and increased its interaction with the wing surface. It was also observed that a stronger HSV resulted in a greater vertical extent above the wing, aligning with findings from Fleming *et al.* [38] and Simpson [33]. This directly affected lift and drag characteristics. The HSV-induced downwash reduced the local effective angle of attack, decreasing local lift, while drag increased due to multiple contributing factors: pressure drag from corner separation at high angles of attack, induced drag from HSV-induced downwash, and interference drag resulting from these junction flow interactions.

The HSV played a critical role in stabilizing or destabilizing the junction boundary layer, with its vertical extent above the wing directly influencing the onset and severity of corner flow separation. At lower porosity levels, the stronger HSV delayed separation by imparting momentum to the boundary layer. However, at very low porosity, excessive vortex-induced shear introduced local instabilities, leading to slight flow separation. In contrast, at high porosity levels, the HSV weakened and partially entered the duct due to lower flow resistance, reducing its stabilizing influence and making the junction boundary layer more susceptible to separation. A balance was observed at a moderate porosity level, where the HSV remained strong and sufficiently close to the wing surface to energize the boundary layer without excessively amplifying shear effects. Furthermore, the analysis indicated that secondary flow structures in the junction region did not significantly impact the duct mass flow rate, indicating that cooling performance remained largely unaffected by aerodynamic interactions in this area. These results highlight the intricate relationship between vortex strength, boundary layer stability, and aerodynamic interference drag. However, a trade-off exists between different heat exchanger porosity. While higher porosity improves cooling performance and reduces cooling installation drag due to lower flow resistance, it leads to corner flow separation and aerodynamic losses in the junction region. In contrast, lower porosity strengthens the HSV and improves boundary layer stability at the junction but at the cost of increased flow resistance and aerodynamic penalties.

The results of this thesis show that a wing-integrated ram-air duct for TMSs is feasible but presents significant aerodynamic challenges for fuel-cell applications due to high cooling requirements. The increased heat exchanger thickness required for sufficient heat transfer introduces unavoidable aerodynamic penalties. However, for systems with lower cooling demands, such as conventional radiator-based applications, this concept remains viable. Due to the steady-state nature of the RANS simulations, this study does not provide a complete insight into the flow behavior, particularly the unsteady dynamics of secondary flow structures at high angles of attack. Additional research is required to further assess aerodynamic interactions and transient effects before reaching a definitive conclusion.

7

Recommendations

This research provides a foundation for understanding the aerodynamic performance of a wing-integrated ram-air duct system with a heat exchanger modeled as a porous medium, and the complex flow dynamics at the wing-body junction, specifically for propeller-driven aircraft applications. While significant insights have been gained, certain limitations and open questions remain, requiring further research to validate and expand on these findings. The following recommendations were made throughout this research, split into those related to the 2D and 3D aerodynamic analysis.

2D aerodynamic analysis

- This study was conducted at sea-level conditions with a Mach number of 0.22 to establish a validation database for future wind tunnel experiments, given the novelty of this research and the absence of comparable studies in the literature. A chord-based Reynolds number of approximately 5×10^6 was chosen as it is characteristic of low-speed wind tunnel testing, where it is feasible to replicate flow conditions for experimental validation. While real aircraft operate at significantly higher Reynolds numbers, this selection ensures the simulations remain in the incompressible flow regime, avoiding compressibility effects and facilitating direct comparison with future wind tunnel experiments. While the reference airfoil case (MS(1)-0317) was validated against experimental data, the ducted wing configuration has yet to be experimentally validated. Therefore, to assess the accuracy of the CFD results, future work should include validation through wind tunnel testing.

- The ducted wing profile, derived from a DoE approach with discrete factor levels, effectively captured flow physics and parameter influences on aerodynamic performance but omitted continuous design space exploration. Future work should employ Multidisciplinary Design Optimization (MDO) to explore the full design space, potentially yielding more aerodynamically efficient ducted airfoils. Additionally, the current study focused only on aerodynamics and the effect of cold-side pressure drop, without considering the heat transfer performance of the heat exchanger. A full optimization should integrate thermal effects by coupling shape optimization with an extensive heat exchanger database that accounts for both pressure drop and thermal performance across different arrangements and porosities. Higher-fidelity thermal modeling beyond the ε-NTU method should also be considered.

- At climb angles of attack (e.g., 10°), steady RANS simulations introduce increased discretization errors due to the growing influence of unsteady flow phenomena, including flow separation and vortex shedding. To improve the accuracy of aerodynamic force predictions and further refine the ducted airfoil shapes for climb conditions, future work should consider unsteady RANS (URANS) simulations. Capturing transient flow structures through URANS may provide a more accurate estimation of aerodynamic loads and mitigate discretization errors associated with steady-state assumptions.

- Extending the analysis to higher flow speeds and altitudes representative of real cruise conditions is recommended to assess compressibility effects on the aerodynamic performance of the ducted wing and the cooling efficiency of the heat exchanger. Additionally, investigating the contribution of the Meredith effect in this configuration will help quantify its potential to offset the cooling installation drag.

- A 2D actuator disk simulation of the propeller slipstream is recommended to evaluate the impact of the velocity distribution on the cooling performance of the ducted heat exchanger. The increased mass flow rate induced by the propeller is expected to improve cooling efficiency, which may allow for adjustments in the spanwise width of the duct or heat exchanger thickness while maintaining the same thermal performance.

3D AERODYNAMIC ANALYSIS

- The use of RANS in this study, while computationally efficient, has inherent limitations in predicting the strength, size and location of the HSV over the wing, as this phenomenon is highly unsteady. Previous studies, indicate that linear EVMs do not resolve the anisotropy in normal Reynolds stresses [41, 60, 61], leading to inaccurate predictions of secondary flow structures, especially corner flow separation. In RANS turbulence modeling, EVMs assume isotropic turbulence, which restricts their ability to resolve the complex interactions governing vortex formation and evolution. While 3D RANS simulations were employed in this study due to their feasibility compared to the high computational cost of LES, the results serve as a benchmark for potential future LES investigations. LES would provide a more accurate representation of the unsteady dynamics of the junction flow and offer improved predictions of turbulence-driven flow features in this region, especially corner flow separation.

- Investigating the effect of varying incoming boundary layer thickness on secondary flow structures in the nacelle/wing-integrated duct junction would provide deeper insight into how upstream flow conditions influence HSV strength, topology, and corner flow separation in the presence of heat exchanger-induced flow resistance.

- Implementing a leading-edge fillet, as explored by Hinson and Hoffmann [62], at the nacelle/ducted-wing junction could mitigate the formation of the horseshoe vortex by reducing the upstream adverse pressure gradient. Weakening or eliminating the HSV would minimize interference drag, improving the aerodynamic efficiency of the nacelle/ ducted-wing configuration. Additionally, suppressing the HSV and potential corner flow separation is crucial, as uncontrolled separation could propagate outboard over the wing, potentially affecting control surfaces and leading to adverse handling characteristics.

- Full-blade URANS simulations of the propeller slipstream should be conducted to gain deeper insight into its effect on duct performance, including unsteady (pumping) heat transfer, and propeller-inlet interaction. Conducting such a study is recommended to fully assess the impact of axial and swirl velocity distributions on the aerodynamic performance of the wing and the overall integration of the ducted system.

Bibliography

[1] M. Coutinho, D. Bento, A. Souza, R. Cruz, F. Afonso, F. Lau, A. Suleman, F. R. Barbosa, R. Gandolfi, W. Affonso, F. I. Odaguil, M. F. Westin, R. J. dos Reis, and C. R. da Silva, *A review on the recent developments in thermal management systems for hybrid-electric aircraft,* Applied Thermal Engineering **227** (2023), https://doi.org/10.1016/j.applthermaleng.2023.120427.

[2] Clean Sky 2 and Fuel Cells & Hydrogen 2 Joint Undertakings, *Hydrogen-powered aviation: A fact-based study of hydrogen technology, economics, and climate impact by 2050,* Website (2020), https://www.clean-aviation.eu/media/publications/hydrogen-powered-aviation.

[3] C. K. Sain, J. Hänsel, and S. Kazula, *Conceptual design of air and thermal management in a nacelle-integrated fuel cell system for an electric regional aircraft,* AIAA AVIATION 2023 Forum (2023), https://doi.org/10.2514/6.2023-3875.

[4] C. L. Pastra, G. Cinar, and D. N. Mavris, *Feasibility and benefit assessments of hybrid hydrogen fuel cell and battery configurations on a regional turboprop aircraft,* AIAA AVIATION 2022 Forum (2022), https://doi.org/10.2514/6.2022-3290.

[5] Universal Hydrogen, *Universal Hydrogen Successfully Completes First Flight of Hydrogen Regional Airliner,* Website (2023), https://hydrogen.aero/press-releases/universal-hydrogen-successfully-completes-first-flight-of-hydrogen-regional-airliner/.

[6] ZeroAvia, *KLM and ZeroAvia Planning Zero-Emission Demonstration Flight in 2026,* Website (2024), https://zeroavia.com/press/klm-and-zeroavia-planning-zero-emission-demonstration-flight-in-2026/.

[7] A. Scoccimarro, *Preliminary Design Methods for the Thermal Management of Fuel Cell Powered Aeroengines*, Master's thesis, Delft University of Technology (2023), https://resolver.tudelft.nl/uuid:9a16e0f8-722d-4a17-9f79-96cea2de6906.

[8] D. R. Chapman, *Investigation of Slipstream Effects on a Wing-inlet Oil-cooler Ducting System of a Twin-engine Airplane in the Ames 40- by 80-foot Wind Tunnel*, Wartime Report NACA-WR-A-1 (NASA, Langley Research Center, Hampton VA 23681-2199, USA, 1945) https://ntrs.nasa.gov/citations/19930093542.

[9] J. Keith, Arvid L and J. Schiff, *Low-speed wind-tunnel investigation of a triangular sweptback air inlet in the root of a 45 degree sweptback wing*, Research Memorandum NACA/RM-L50I01 (NASA, Langley Research Center, Hampton VA 23681-2199, USA, 1950) https://ntrs.nasa.gov/citations/19930086423.

[10] T. A. Harris and I. G. Recant, *Investigation in the 7-By-10 Foot Wind Tunnel of Ducts for Cooling Radiators Within an Airplane Wing*, Special Report NASA/SR-93 (NASA, Langley Research Center, Hampton VA 23681-2199, USA, 1938) https://ntrs.nasa.gov/citations/20090014718.

[11] E. A. Elsaadawy and C. P. Britcher, *Effect of propeller slipstream on heat-exchanger installations at low reynolds number,* Journal of Aircraft (2003), https://doi.org/10.2514/2.3154.

[12] P. Martin, *Inlet-airfoil design method for heat exchangers of a high altitude rpa,* 36th AIAA Aerospace Sciences Meeting and Exhibit (2012), https://doi.org/10.2514/6.1998-10.

[13] J. Kuhlman, M. Kessinger, T. Chaillou, J. Kuhlman, M. Kessinger, and T. Chaillou, *Performance of the wing integrated heat exchanger of the theseus uav,* 15th Applied Aerodynamics Conference (1994), https://doi.org/10.2514/6.1997-2316.

[14] A. L. Habermann, A. Khot, D. E. Lampl, and C. Perren, *Aerodynamic effects of a wing surface heat exchanger,* Aerospace (2023), https://doi.org/10.3390/aerospace10050407.

[15] S. J. Miley, *Aerodynamics of liquid-cooled aircraft engine installations,* SAE International (1985), https://doi.org/10.4271/850896.

[16] A. van Heerden, D. Judt, S. Jafari, C. Lawson, T. Nikolaidis, and D. Bosak, *Aircraft thermal management: Practices, technology, system architectures, future challenges, and opportunities,* Progress in Aerospace Sciences (2022), https://doi.org/10.1016/j.paerosci.2021.100767.

[17] B. Russ and M. Drela, *Ram air heat exchangers for very high-altitude subsonic aircraft,* SAE International (1993), https://doi.org/10.4271/931145.

[18] D. Küchemann and J. Weber, *Aerodynamics of Propulsion*, McGraw-Hill publications in aeronautical science (McGraw-Hill, 1953).

[19] E. J. Adler, B. J. Brelje, and J. R. R. A. Martins, *Thermal management system optimization for a parallel hybrid aircraft considering mission fuel burn,* Aerospace (2022), https://doi.org/10.3390/aerospace9050243.

[20] D. Biermann and C. H. McLellan, *Wind-tunnel investigation of rectangular air-duct entrances in the leading edge of an NACA 23018 wing*, Special Report NASA/SR-154 (NASA, Langley Research Center, Hampton VA 23681-2199, USA, 1940) https://ntrs.nasa.gov/citations/20090014885.

[21] S. Katzoff, *High-altitude cooling V: cowling and ducting*, Wartime Report NASA/WR-L-775 (NASA, Langley Research Center, Hampton VA 23681-2199, USA, 1944) https://ntrs.nasa.gov/citations/19930093174.

[22] R. E. Dannenberg, *A design study of leading-edge inlets for unswept wings*, Research Memorandum NASA/RM-A9K02b (NASA, Langley Research Center, Hampton VA 23681-2199, USA, 1950) https://ntrs.nasa.gov/citations/19930086018.

[23] P. Martin, B. Crawford, C. Britcher, S. Miley, and T.-K. Wang, *Experiments on an inlet-airfoil designed for heat exchangers of a high altitude rpa,* 16th AIAA Applied Aerodynamics Conference (2012), https://doi.org/10.2514/6.1998-2533.

[24] A. E. V. Doenhoff and E. A. Horton, *Preliminary Investigation in the NACA Low-Turbulence Tunnel of Low-Drag Airfoil Sections Suitable for Admitting Air at the Leading Edge*, Wartime Report NASA/WR-L-694 (NASA, Langley Research Center, Hampton VA 23681-2199, USA, 1942) https://ntrs.nasa.gov/citations/19930092757.

[25] A. M. O. Smith, *High-lift aerodynamics,* Journal of Aircraft (1975), https://doi.org/10.2514/3.59830.

[26] S. F. Racisz, *Development of Wing Inlets*, Wartime Report NASA/WR-L-727 (NASA, Langley Research Center, Hampton VA 23681-2199, USA, 1946) https://ntrs.nasa.gov/citations/19930092761.

[27] D. Bierman and B. W. Corson, *Model Tests of a Wing-Duct System for Auxiliary Air Supply*, Technical Memorandum NASA/TM-X-57675 (NASA, Langley Research Center, Hampton VA 23681-2199, USA, 1941) https://ntrs.nasa.gov/citations/19660085318.

[28] H. Kellermann, M. Lüdemann, M. Pohl, and M. Hornung, *Feasibility and benefit assessments of hybrid hydrogen fuel cell and battery configurations on a regional turboprop aircraft,* Aerospace (2021), https://doi.org/10.3390/aerospace8010003.

[29] H. H. Sweberg and R. C. Dingeldein, *Summary of Measurements in Langley Full-Scale Tunnel of Maximum Lift Coefficients and Stalling Characteristics of Airplanes*, Technical Report NACA-TR-829 (NASA, Langley Research Center, Hampton VA 23681-2199, USA, 1945) https://ntrs.nasa.gov/citations/19930091906.

[30] L. Piancastelli, L. Frizziero, and G. Donnici, *The meredith ramjet: an efficient way to recover the heat wasted in piston engine cooling,* Aerospace (2015), https://api.semanticscholar.org/CorpusID:54909085.

[31] J. Eissele, S. Lafer, C. Mejìa Burbano, J. Schlieflus, T. Wiedmann, J. Mangold, and A. Strohmayer, *Hydrogen-powered aviation-design of a hybrid-electric regional aircraft for entry into service in 2040,* Aerospace (2023), https://doi.org/10.3390/aerospace10030277.

[32] S. Raghunathan Srikumar, *LES of a novel wing/body junction : Anti-fairing*, Master's thesis, Delft University of Technology (2019), https://resolver.tudelft.nl/uuid:86621aa3-90a6-4929-9534-97459ef11f87.

[33] R. L. Simpson, *Junction flows,* Annual Review of Fluid Mechanics , 415 (2001).

[34] J. L. Ziyan Wei and S. Tan, *Numerical investigation of a simplified wingbody junction flow,* International Journal of Computational Fluid Dynamics , 731 (2022).

[35] F. Gand, S. Deck, V. Brunet, and P. Sagaut, *Flow dynamics past a simplified wing body junction,* Physics of Fluids (2010), https://doi.org/10.1063/1.3500697.

[36] Z. Belligoli, A. J. Koers, R. P. Dwight, and G. Eitelberg, *Using an anti-fairing to reduce drag at wing/body junctions,* AIAA Journal (2019), https://doi.org/10.2514/1.J057481.

[37] F. Gand, V. Brunet, and S. Deck, *A combined experimental, rans and les investigation of a wing body junction flow,* AIAA Journal (2010), https://doi.org/10.2514/6.2010-4753.

[38] J. L. Fleming, R. L. Simpson, J. E. Cowling, and W. J. Devenport, *An experimental study of a turbulent wing-body junction and wake flow,* Experiments in Fluids (1993), https://doi.org/10.1007/BF00189496.

[39] T. J. Barber, *An investigation of strut-wall intersection losses,* Journal of Aircraft (1978), https://doi.org/10.2514/3.58427.

[40] R. D. Mehta, *Effect of wing nose shape on the flow in a wing/body junction,* The Aeronautical Journal (1984), https://doi.org/10.1017/S000192400001455X.

[41] S. R. Srikumar, *LES of a novel wing/body junction : Anti-fairing*, Master's thesis, Delft University of Technology (2019), https://resolver.tudelft.nl/uuid:86621aa3-90a6-4929-9534-97459ef11f87.

[42] A. Inc., *ANSYS Fluent Theory Guide*, ANSYS Inc., Canonsburg, PA, release 2023 r2 ed. (2023).

[43] F. R. Menter, *Two-equation eddy-viscosity turbulence models for engineering applications,* AIAA Journal (1994), https://doi.org/10.2514/3.12149.

[44] A. Inc., *ANSYS Fluent User's Guide*, ANSYS Inc., Canonsburg, PA, release 2023 r2 ed. (2023).

[45] D. C. Montgomery, *Design and Analysis of Experiments* (John Wiley & Sons, 2017).

[46] L. Eça and M. Hoekstra, *Discretization uncertainty estimation based on a least squares version of the grid convergence index,* (2006).

[47] L. Eça and M. Hoekstra, *A procedure for the estimation of the numerical uncertainty of cfd calculations based on grid refinement studies,* Journal of Computational Physics , 104 (2014).

[48] T. Stokkermans, *Aerodynamics of Propellers in Interaction Dominated Flowfields: An Application to Novel Aerospace Vehicles*, Ph.D. thesis, Delft University of Technology (2005), https://doi.org/10.4233/uuid:46178824-bb80-4247-83f1-dc8a9ca7d8e3.

[49] R. J. McGhee and W. D. Beasley, *Low-speed aerodynamic characteristics of a 17-percent-thick medium speed airfoil designed for general aviation applications*, Technical Publication NASA-TP-1786 (NASA, Langley Research Center, Hampton VA 23681-2199, USA, 1980) https://ntrs.nasa.gov/citations/19830008019.

[50] F. K. Owen and A. K. Owen, *Measurement and assessment of wind tunnel flow quality,* Progress in Aerospace Sciences , 315 (2008).

[51] S. Kakaç, H. Liu, and A. Pramuanjaroenkij, *Heat Exchangers: Selection, Rating, and Thermal Design, fourth edition* (2020).

[52] R. K. Shah and D. P. Sekulic, *Fundamentals of heat exchanger Design* (John Wiley & Sons, 2003).

[53] C. K. Sain, J. Hänsel, and S. Kazula, *Preliminary design of air and thermal management of a nacelle-integrated fuel cell system for an electric regional aircraft,* IEEE Transportation Electrification Conference & Expo (ITEC) (2023), https://doi.org/10.1109/ITEC55900.2023.10187105.

[54] F. Beltrame, L. J. Van Dongen, P. Colonna, and C. M. De Servi, *Optimal design of a ram air cooling duct housing the condenser of an airborne orc whr unit,* Proceedings (2024), https://doi.org/10.33737/gpps24-tc-107.

[55] D. Missirlis, S. Donnerhack, O. Seite, C. Albanakis, A. Sideridis, K. Yakinthos, and A. Goulas, *Numerical development of a heat transfer and pressure drop porosity model for a heat exchanger for aero engine applications,* Applied Thermal Engineering , 1341 (2010).

[56] M. Musto, N. Bianco, G. Rotondo, F. Toscano, and G. Pezzella, *A simplified methodology to simulate a heat exchanger in an aircraft's oil cooler by means of a porous media model,* Applied Thermal Engineering (2016), https://doi.org/10.1016/j.applthermaleng.2015.10.147.

[57] W. Kays and A. London, *Compact Heat Exchangers* (Krieger Publishing Company, 1998).

[58] P. Korba, S. Al-Rabeei, M. Hovanec, I. Sekelová, and U. Kale, *Structural design and material comparison for aircraft wing box beam panel,* Heliyon (2024), https://doi.org/10.1016/j.heliyon.2024.e27403.

[59] F. W. Meredith, *Cooling of aircraft engines with special reference to ethylene glycol radiators enclosed in ducts*, Technical Report ARC/R&M-1683 (Aeronautical Research Committee Reports & Memoranda, 1935) https://reports.aerade.cranfield.ac.uk/handle/1826.2/1425.

[60] F. Gand, V. Brunet, and S. Deck, *Experimental and numerical investigation of a wing-body junction flow,* AIAA Journal (2012), https://doi.org/10.2514/1.J051462.

[61] S. Ryu, M. Emory, G. Iaccarino, A. Campos, and K. Duraisamy, *Large-eddy simulation of a wingbody junction flow,* AIAA Journal (2016), https://doi.org/10.2514/1.J054212.

[62] B. C. Hinson and K. A. Hoffmann, *Parametric exploration of wingbody junction flow using computational fluid dynamics,* Journal of Aircraft (2015), https://doi.org/10.2514/1.C032985.

Part V

Appendices

A

HEAT EXCHANGER SIZING EXAMPLE USING THE ε-NTU METHOD

This appendix demonstrates the heat exchanger sizing process for a single configuration, considering one porosity value. The assumptions used for the calculations are outlined below. The optimization routine, implemented in MATLAB, outputs the hot fluid mass flow rate, the required total heat transfer area, the cold and hot outlet temperatures and the actual heat rejection rate. The output must satisfy the compactness requirement for the specified porosity, ensuring the heat exchanger design fits within the wing. The methodology follows a step-by-step approach to compute the three non-dimensional parameters associated with the ε-NTU method: effectiveness, number of transfer units (NTU), and heat capacity ratio.

The objective is to ensure that the heat exchanger satisfies the cooling requirements while maintaining outlet temperatures for the hot and cold fluids within imposed constraints to minimize system inefficiencies caused by large temperature gradients. Below, the main steps and results of the heat exchanger sizing are presented.

Inputs and assumptions:

- Overall heat transfer coefficient, $U = 130\,\mathrm{W\,m^{-2}\,K^{-1}}$
- Heat exchanger thickness-to-chord ratio, $\frac{t}{c} = 0.15$
- Heat exchanger volume, V = 0.02175 $\mathrm{m^3}$
- Cold inlet temperature, $T_{c_{\mathrm{in}}} = 27.5$ °C (300.65 K)
- Hot inlet temperature, $T_{h_{\mathrm{in}}} = 80$ °C (353.15 K)
- Specific heat capacity of water-glycol mixture (50% Ethylene Glycol / 50% Water mixture), $c_{p_\mathrm{h}} = 3410\,\mathrm{J\,kg^{-1}\,K^{-1}}$ and of air $c_{p_\mathrm{c}} = 1006.5\,\mathrm{J\,kg^{-1}\,K^{-1}}$
- Mass flow rate (cold side), 4.06 $\mathrm{kg\,s^{-1}}$ (porosity = 0.88)
- Required fuel cell heat rejection rate, $\dot{q} = 40.79\,\mathrm{kW\,m^{-2}}$

- The outlet temperature difference between the hot and cold sides is constrained by the condition:

  $\min\left(\left|T_{h_{\text{out}}} - T_{c_{\text{out}}}\right|\right) \leq \epsilon$, where ϵ denotes a small tolerance value

Outputs:

- Cold outlet temperature, $T_{c_{\text{out}}} = 37.48$ °C (310.63 K)
- Hot outlet temperature, $T_{h_{\text{out}}} = 41.12$ °C (314.27 K)
- Temperature difference (cold side), $\Delta T_c = 9.98$ °C or K
- Temperature difference (hot side), $\Delta T_h = 42.52$ °C or K
- Mass flow rate (hot side), $\dot{m}_{\text{h}} = 0.3076\ \text{kg}\,\text{s}^{-1}$
- Total required heat transfer area, $A = 13.05\ \text{m}^2$
- Heat exchanger compactness, $\beta = 600\,\text{m}^2\,\text{m}^{-3}$ (porosity = 0.88)

The computed results above were derived using the step-by-step approach detailed below. The hot-side mass flow rate $\dot{m}_{\text{h}}$, and total heat transfer area, A, are iteratively adjusted in the MATLAB routine to ensure the heat transfer rate $\dot{q}$, meets the required value, and the outlet temperatures remain within a similar range. Additionally, the total heat transfer area is adjusted to achieve the desired compactness at a porosity of 0.88. To calculate the heat capacity rate ratio, the heat capacity rates of both the cold and hot fluids are determined first. The cold mass flow rate is dependent on the porosity, but is fixed for this exercise. In contrast, the hot mass flow rate is treated as an output variable in this analysis.

$$C_{\text{air}} = C_c = (\dot{m}c_p)_{\text{air}} = 4.060\ \text{kg/s}\ \times 1006.5\ \text{J/kg}\cdot\text{K} = 4086.39\ \text{W/K} \tag{A.1}$$

$$C_{\text{liquid}} = C_h = (\dot{m}c_p)_{\text{liquid}} = 0.3076\ \text{kg/s}\ \times 3410\ \text{J/kg}\cdot\text{K} = 1048.92\ \text{W/K} = C_{\text{min}} \tag{A.2}$$

The heat capacity rate ratio is calculated using the formula:

$$C^* = \frac{C_{\text{min}}}{C_{\text{max}}} = \frac{C_{\text{liquid}}}{C_{\text{air}}} = \frac{1048.92\ \text{W/K}}{4086.39\ \text{W/K}} = 0.257 \tag{A.3}$$

The number of transfer units NTU is determined based on the minimum capacity rate. As shown in the formula below, U and C_{min} are assumed constants, making NTU directly proportional to the heat transfer area A, which serves as an output variable in this analysis. The heat transfer area A, is adjusted until the desired compactness β is achieved.

$$\text{NTU} = \frac{UA}{C_{\text{min}}} = \frac{130 \times 13.05}{1048.92} = 1.617 \tag{A.4}$$

The heat exchanger thermal efficiency ε, is calculated using the ε-NTU relationship for an unmixed-unmixed cross-flow heat exchanger [51], as shown below.

$$\varepsilon = 1 - e^{\left(\frac{1}{C^*}\right)(\mathrm{NTU})^{0.22}\left(e^{-C^*(\mathrm{NTU})^{0.78}}-1\right)} = 1 - e^{\left(\frac{1}{0.257}\right)(1.617)^{0.22}\left(e^{-0.257(1.617)^{0.78}}-1\right)} \approx 0.741 \tag{A.5}$$

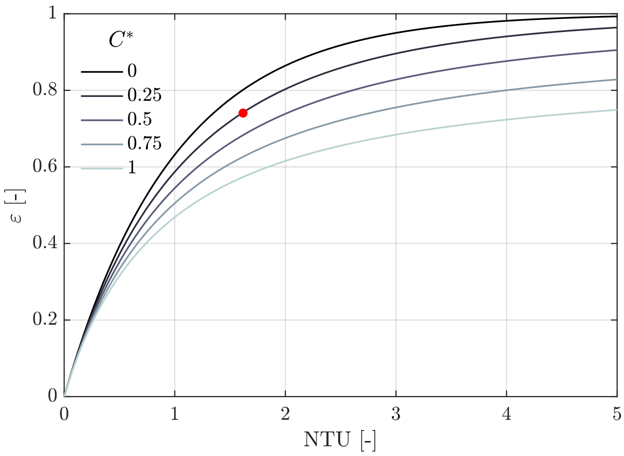

Figure A.1: Effectiveness of the unmixed-unmixed cross-flow heat exchanger.

To compute the actual heat transfer rate $\dot{q}_{\mathrm{actual}}$, the equation below is applied. The maximum possible heat transfer rate $\dot{q}_{\mathrm{max}}$, is calculated using Equation A.7, which depends on the flow rates and inlet fluid temperatures, as outlined by Shah and Sekulic [52], Kays and London [57].

$$\varepsilon = \frac{\dot{q}_{\mathrm{actual}}}{\dot{q}_{\mathrm{max}}} \tag{A.6}$$

$$\dot{q}_{\mathrm{max}} = C_{\mathrm{min}}(T_{h_{in}} - T_{c_{in}}) = 1048.92 \times (353.15 - 300.65) = 55.07 \text{ kW} \tag{A.7}$$

As a result, the iteration variable $\dot{q}_{\mathrm{actual}}$ is calculated and must match the required heat transfer rate to meet the cooling demands of the heat exchanger.

$$\dot{q}_{\mathrm{actual}} = \varepsilon\ \dot{q}_{\mathrm{max}} = 0.741 \times 55.07 = 40.80 \text{ kW} \tag{A.8}$$

Once the heat transfer rate is known, the outlet temperatures for the air and coolant can be calculated as follows:

$$\dot{q}_{\mathrm{actual}} = C_c(T_{c_{\mathrm{out}}} - T_{c_{\mathrm{in}}}) \rightarrow T_{c_{\mathrm{out}}} = T_{c_{\mathrm{in}}} + \frac{\dot{q}_{\mathrm{actual}}}{C_c} = 37.48^{\circ}\mathrm{C}\ (310.63\mathrm{K}) \tag{A.9}$$

$$\dot{q}_{\mathrm{actual}} = C_h(T_{h_{\mathrm{in}}} - T_{h_{\mathrm{out}}}) \rightarrow T_{h_{\mathrm{out}}} = T_{h_{\mathrm{in}}} - \frac{\dot{q}_{\mathrm{actual}}}{C_h} = 41.12^{\circ}\mathrm{C}\ (314.27\mathrm{K}) \tag{A.10}$$

The outlet temperatures $T_{h_{\mathrm{out}}}$ and $T_{c_{\mathrm{out}}}$, differ by $\approx 3.64^{\circ}$, indicating minimal temperature differences. Furthermore, the heat transfer rate per unit volume for this design is added as a variable volumetric heat source term in ANSYS® Fluent. To account for velocity variations inside the duct, a 6th-degree polynomial fit is used to estimate the heat transfer rate, enabling off-design thermal performance analysis while keeping all other parameters fixed. As shown in Figure A.2, the pressure gradient and heat transfer rate are plotted as functions of velocity. The heat transfer rate is normalized per unit span and by the square of the chord length, reflecting the scaling applied in the computational domain. This scaling accounts for the single-cell extrusion in the z-direction (1 m span) and ensures consistency with the wing's geometric parameters while maintaining the dimensional nature of the heat transfer rate (e.g., $\mathrm{kW\,m^{-3}}$).

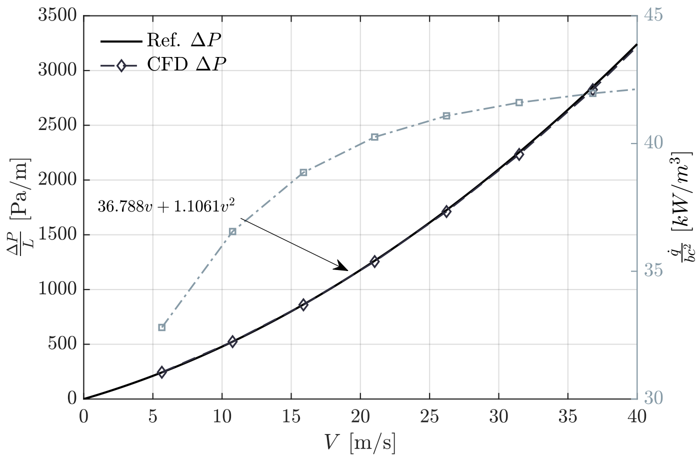

Figure A.2: Heat exchanger ($\varepsilon = 0.88$) pressure gradient and heat transfer rate as a function of velocity, with the heat transfer rate normalized per unit span and the square of the chord length.

Furthermore, applying the heat transfer rate results from Figure A.2 to the ATR-72 root chord ($c_r = 2.62$m) [58] provides heat exchanger dimensions that reflect real-world scaling effects. The parameters derived based on this reference chord, computed using the MATLAB routine, are outlined below:

Inputs

- Mass flow rate (cold side), $10.636\ \mathrm{kg\,s^{-1}}$ (porosity = 0.88)
- Heat exchanger volume, V = $0.1493\ \mathrm{m^3}$

Outputs:

- Cold outlet temperature, $T_{c_{\text{out}}} = 53.66$ °C (326.81 K)
- Hot outlet temperature, $T_{h_{\text{out}}} = 55.67$ °C (328.82 K)
- Temperature difference (cold side), $\Delta T_c = 26.16$ °C or K
- Temperature difference (hot side), $\Delta T_h = 24.33$ °C or K
- Mass flow rate (hot side), $\dot{m}_\text{h} = 3.375\ \mathrm{kg\,s^{-1}}$
- Total required heat transfer area, $A = 89.58\ \mathrm{m^2}$
- Fuel cell heat rejection rate, $\dot{q} = 280$ kW
- Heat exchanger compactness, $\beta = 600\,\mathrm{m^2\,m^{-3}}$ (porosity = 0.88)

B

FIGURES

B.1. MESH

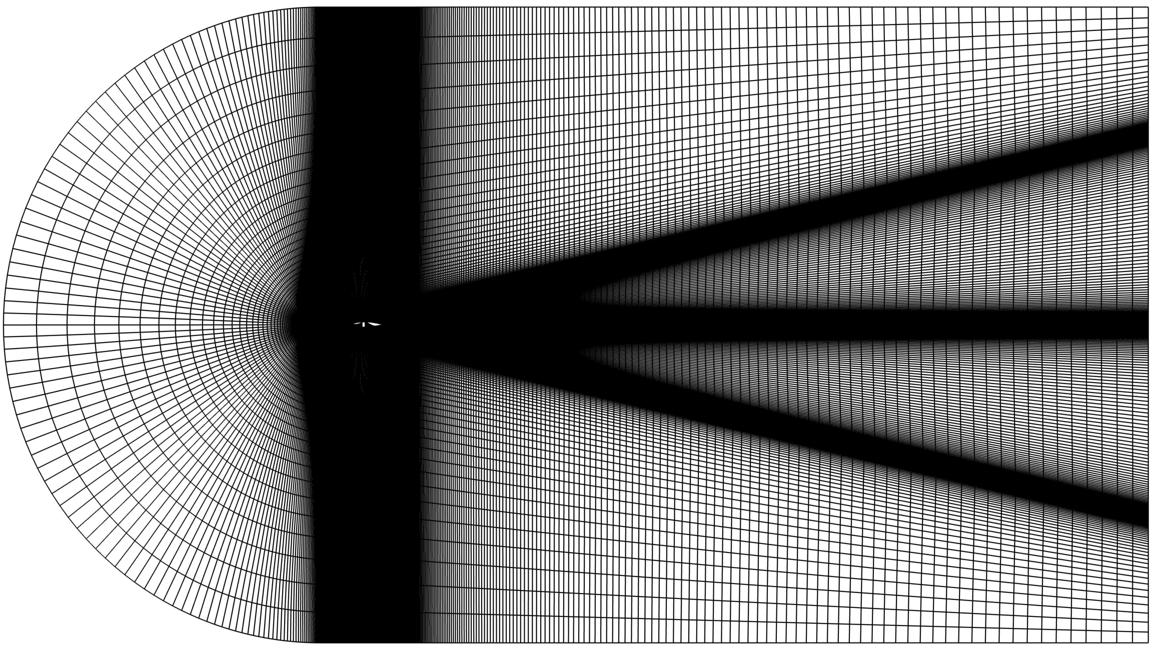

Figure B.1: Mesh of the entire domain.

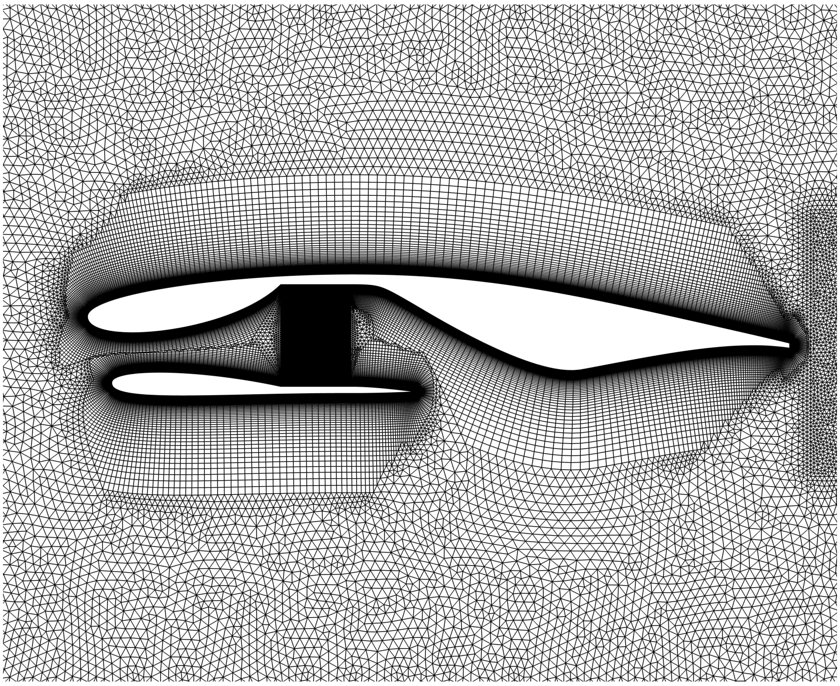

Figure B.2: Mesh around the ducted wing housing heat exchanger modeled as a porous zone, with anisotropic tetrahedral extrusion in the near-wall region.

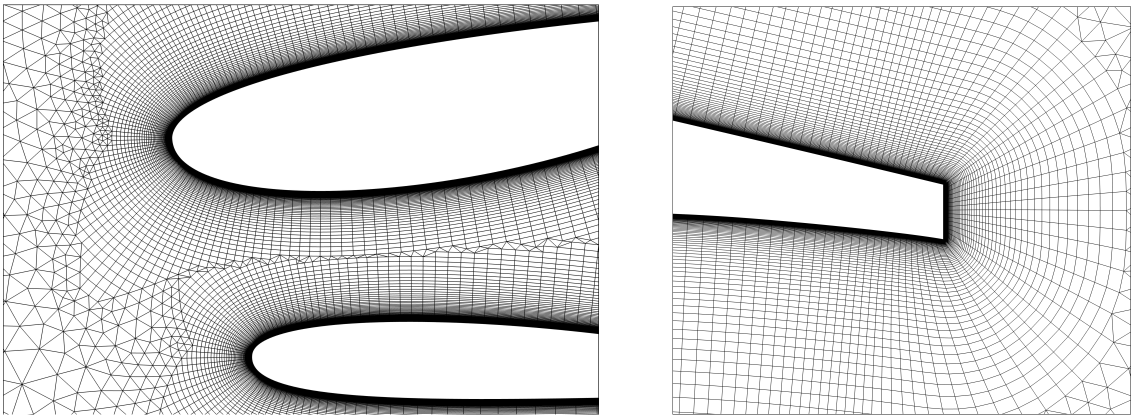

(a) Leading-edge

(b) Trailing-edge

Figure B.3: Detailed mesh visualization at the leading and trailing edges.

B.2. EFFECT OF DOMAIN BOUNDARY CONDITIONS ON AERODYNAMIC FORCES

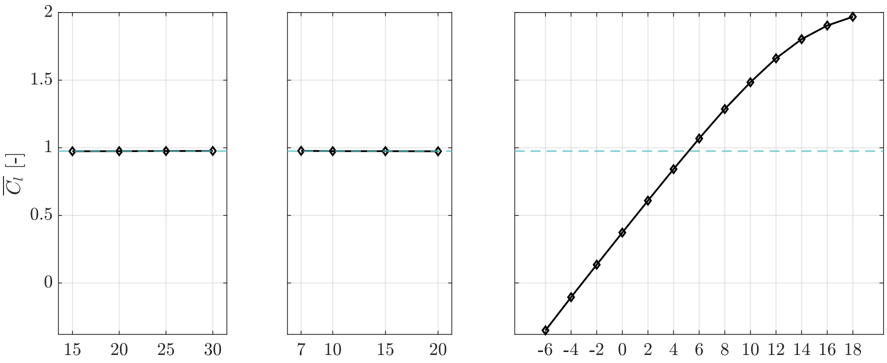

(a) Upstream c (b) Downstream c (c) Angle of attack α [deg]

Figure B.4: Main effects of the upstream and downstream domain placement, normalized by the airfoil chord length (c), on the mean lift coefficient (C_l). Computed at a chord-based Reynolds number of $Re_c \approx 5 \times 10^6$.

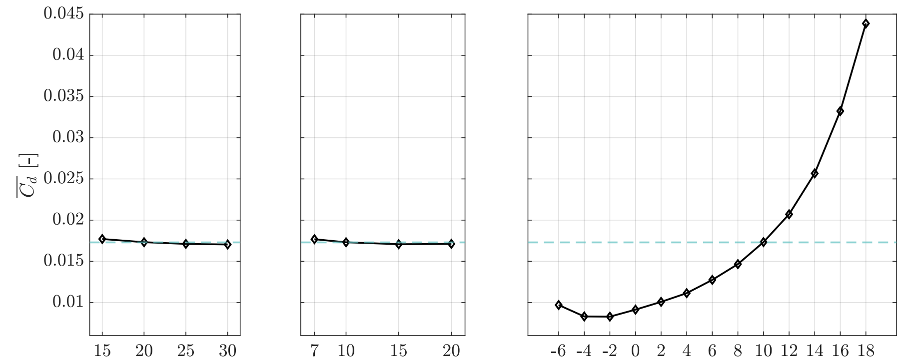

(a) Upstream c (b) Downstream c (c) Angle of attack α [deg]

Figure B.5: Main effects of the upstream and downstream domain placement, normalized by the airfoil chord length (c), on the mean drag coefficient (C_d). Computed at a chord-based Reynolds number of $Re_c \approx 5 \times 10^6$.

B.3. Effect of porosity on the aerodynamic performance of configuration *I-B*

HX porosity 0.72

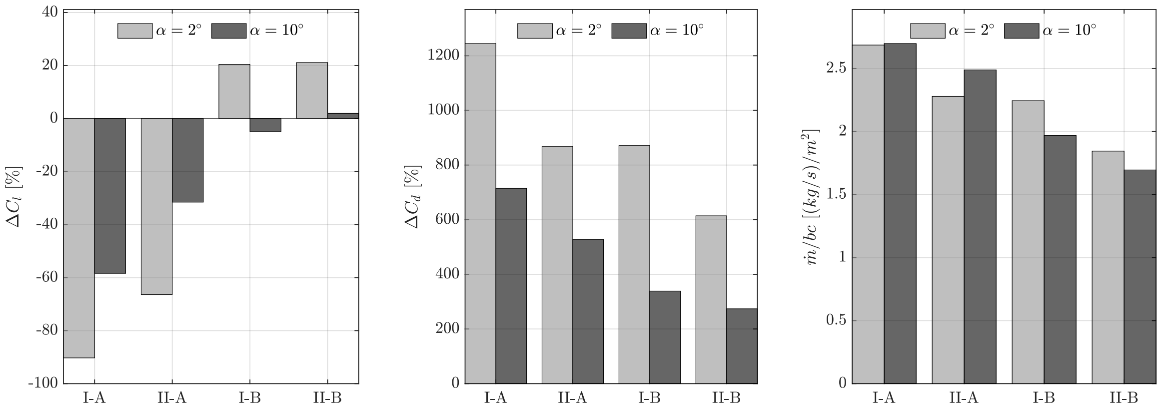

(a) Lift coefficient (b) Drag coefficient (c) Mass flow rate

Figure B.6: Comparison of lift and drag coefficients and duct mass flow rate for best-performing ducted airfoils relative to the clean airfoil, computed for a heat exchanger porosity of 0.72.

Parameter	**Clean AF**	**Config. I-A**	**Config. II-A**	**Config. I-B**	**Config. II-B**
C_l [-]	0.6321	0.0614 (90%)	0.2123 (66%)	0.7612 (20%)	0.7657 (21%)
C_d [-]	0.0080	0.1071 (1245%)	0.0771 (868%)	0.0774 (871%)	0.0569 (614%)
$\dot{m}$ [kgs^{-1}]	-	2.69	2.28	2.25	1.84

Table B.1: Comparison of lift and drag coefficients and duct mass flow rate for best-performing ducted airfoils relative to the clean airfoil, computed at $\alpha = 2°$ and a HX porosity of 0.72.

Parameter	**Clean AF**	**Config. I-A**	**Config. II-A**	**Config. I-B**	**Config. II-B**
C_l [-]	1.5208	0.6324 (58%)	1.0412 (32%)	1.4458 (5%)	1.5507 (2%)
C_d [-]	0.0156	0.1274 (715%)	0.0981 (528%)	0.0686 (339%)	0.0585 (274%)
$\dot{m}$ [kgs^{-1}]	-	2.70	2.49	1.97	1.70

Table B.2: Comparison of lift and drag coefficients and duct mass flow rate for best-performing ducted airfoils relative to the clean airfoil, computed at $\alpha = 10°$ and a HX porosity of 0.72.

HX POROSITY 0.81

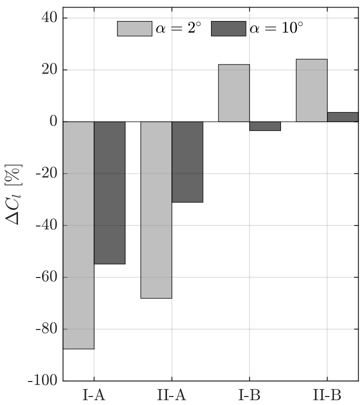

(a) Lift coefficient

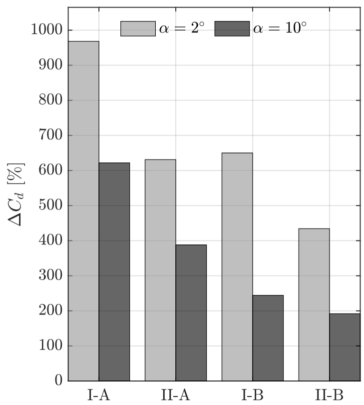

(b) Drag coefficient

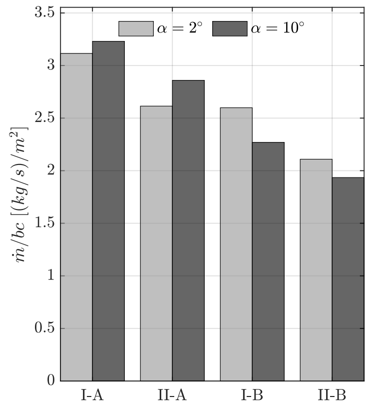

(c) Mass flow rate

Figure B.7: Comparison of lift and drag coefficients and duct mass flow rate for best-performing ducted airfoils relative to the clean airfoil, computed for a heat exchanger porosity of 0.81.

Parameter	**Clean AF**	**Config. I-A**	**Config. II-A**	**Config. I-B**	**Config. II-B**
C_l [-]	0.6321	0.0780 (88%)	0.2016 (68%)	0.7717 (22%)	0.7847 (24%)
C_d [-]	0.0080	0.0851 (968%)	0.0582 (631%)	0.0598 (650%)	0.0426 (434%)
$\dot{m}$ [kgs^{-1}]	-	3.11	2.61	2.60	2.11

Table B.3: Comparison of lift and drag coefficients and duct mass flow rate for best-performing ducted airfoils relative to the clean airfoil, computed at $\alpha = 2°$ and a HX porosity of 0.81.

Parameter	**Clean AF**	**Config. I-A**	**Config. II-A**	**Config. I-B**	**Config. II-B**
C_l [-]	1.5208	0.6862 (55%)	1.0483 (31%)	1.4688 (3%)	1.5759 (4%)
C_d [-]	0.0156	0.1128 (622%)	0.0763 (388%)	0.0538 (244%)	0.0456 (192%)
$\dot{m}$ [kgs^{-1}]	-	3.23	2.86	2.27	1.94

Table B.4: Comparison of lift and drag coefficients and duct mass flow rate for best-performing ducted airfoils relative to the clean airfoil, computed at $\alpha = 10°$ and a HX porosity of 0.81.

HX POROSITY 0.88

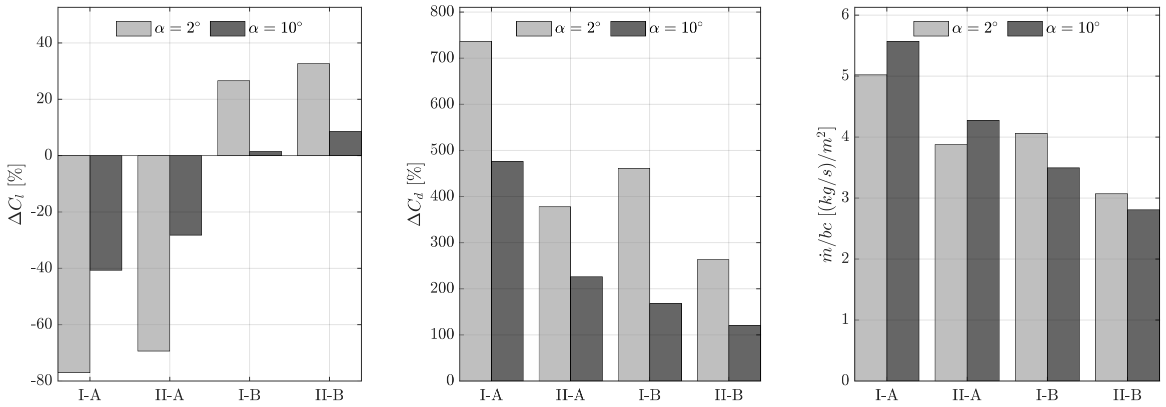

(a) Lift coefficient (b) Drag coefficient (c) Mass flow rate

Figure B.8: Comparison of lift and drag coefficients and duct mass flow rate for the most optimal ducted airfoils relative to the clean airfoil, computed for a heat exchanger porosity of 0.88.

Parameter	**Clean AF**	**Config. I-A**	**Config. II-A**	**Config. I-B**	**Config. II-B**
C_l [-]	0.6321	0.1451 (77%)	0.1936 (69%)	0.8002 (27%)	0.8384 (33%)
C_d [-]	0.0080	0.0667 (737%)	0.0381 (378%)	0.0447 (461%)	0.0289 (263%)
$\dot{m}$ [kg s^{-1}]	-	5.02	3.88	4.06	3.07

Table B.5: Comparison of lift and drag coefficients and duct mass flow rate for best-performing ducted airfoils relative to the clean airfoil, computed at $\alpha = 2°$ and a HX porosity of 0.88.

Parameter	**Clean AF**	**Config. I-A**	**Config. II-A**	**Config. I-B**	**Config. II-B**
C_l [-]	1.5208	0.9021 (41%)	1.0917 (28%)	1.5433 (1%)	1.6516 (9%)
C_d [-]	0.0156	0.0901 (476%)	0.0510 (226%)	0.0419 (168%)	0.0345 (121%)
$\dot{m}$ [kg s^{-1}]	-	5.57	4.27	3.50	2.81

Table B.6: Comparison of lift and drag coefficients and duct mass flow rate for best-performing ducted airfoils relative to the clean airfoil, computed at $\alpha = 10°$ and a HX porosity of 0.88.

B.4. ADDITIONAL 2D AERODYNAMIC RESULTS

INTERACTIONS EFFECTS BETWEEN LDR AND STAGGER ANGLE

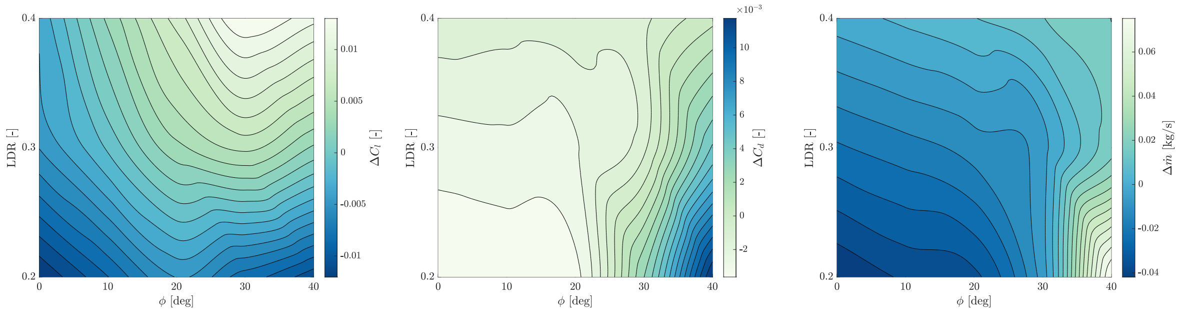

(a) Lift coefficient (b) Drag coefficient (c) Mass flow rate

Figure B.9: Interaction effects between LDR and stagger angle on the deviation of lift coefficient (ΔC_l), drag coefficient (ΔC_d), and duct mass flow rate ($\Delta \dot{m}$) relative to the mean response value, at an angle of attack $\alpha = 2°$ and a chord Reynolds number $Re_c \approx 5 \times 10^6$.

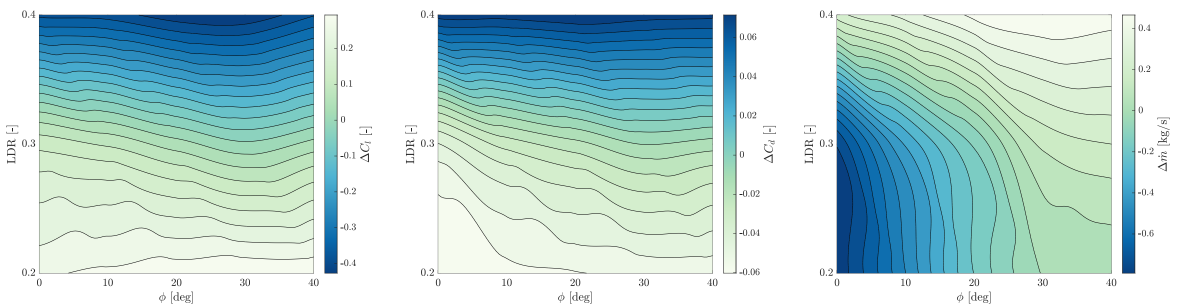

(a) Lift coefficient (b) Drag coefficient (c) Mass flow rate

Figure B.10: Interaction effects between LDR and stagger angle on the deviation of lift coefficient (ΔC_l), drag coefficient (ΔC_d), and duct mass flow rate ($\Delta \dot{m}$) relative to the mean response value, at an angle of attack $\alpha = 10°$ and a chord Reynolds number $Re_c \approx 5 \times 10^6$.

INTERACTIONS EFFECTS BETWEEN LDR AND DUCT GAP

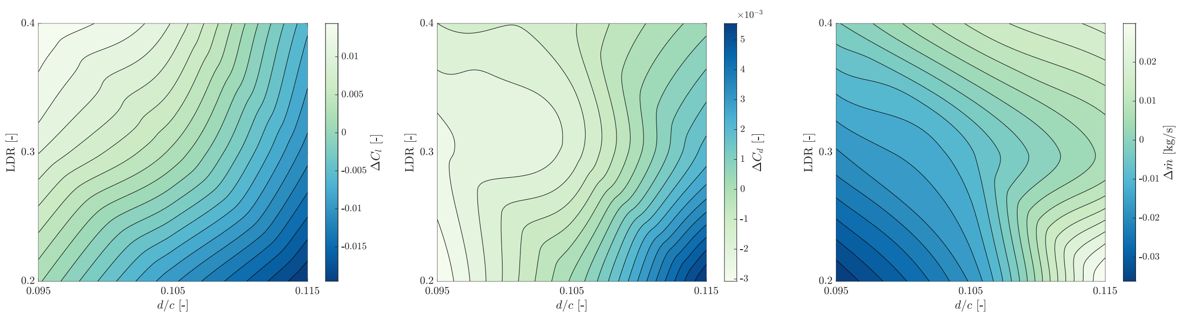

(a) Lift coefficient (b) Drag coefficient (c) Mass flow rate

Figure B.11: Interaction effects between LDR and duct gap on the deviation of lift coefficient (ΔC_l), drag coefficient (ΔC_d), and duct mass flow rate ($\Delta \dot{m}$) relative to the mean response value, at an angle of attack $\alpha = 2°$ and a chord Reynolds number $Re_c \approx 5 \times 10^6$.

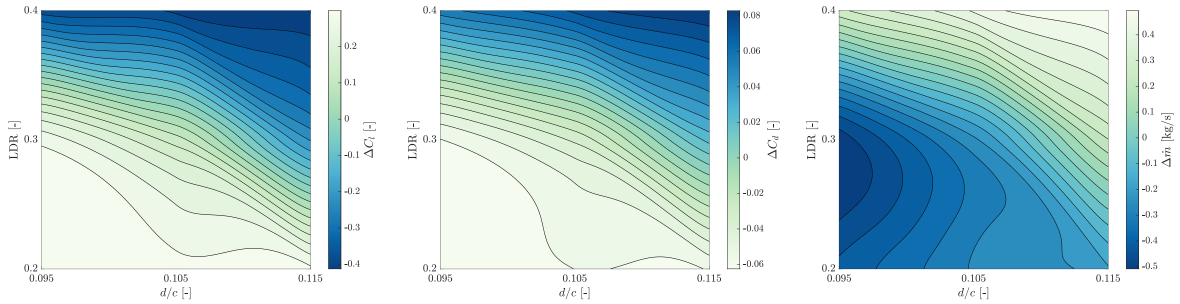

(a) Lift coefficient (b) Drag coefficient (c) Mass flow rate

Figure B.12: Interaction effects between LDR and duct gap on the deviation of lift coefficient (ΔC_l), drag coefficient (ΔC_d), and duct mass flow rate ($\Delta \dot{m}$) relative to the mean response value, at an angle of attack $\alpha = 10°$ and a chord Reynolds number $Re_c \approx 5 \times 10^6$.

INTERACTIONS BETWEEN DUCT GAP AND STAGGER ANGLE

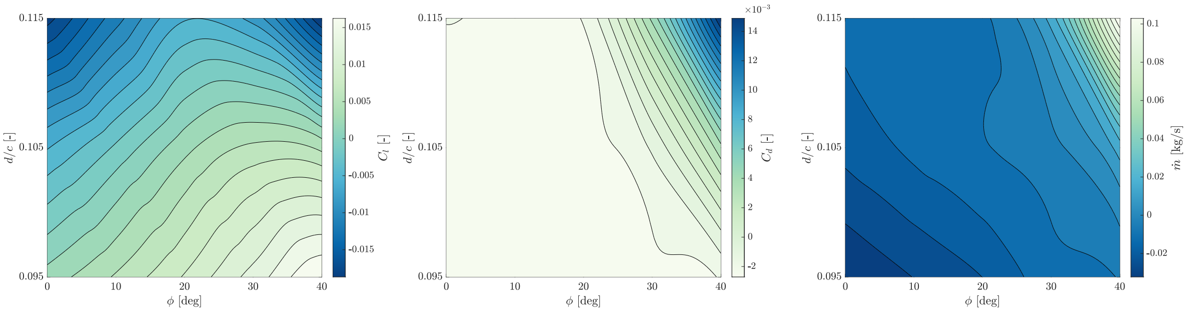

(a) Lift coefficient (b) Drag coefficient (c) Mass flow rate

Figure B.13: Interaction effects between duct gap and stagger angle on the deviation of lift coefficient (ΔC_l), drag coefficient (ΔC_d), and duct mass flow rate ($\Delta \dot{m}$) relative to the mean response value, at an angle of attack $\alpha = 2°$ and a chord Reynolds number $Re_c \approx 5 \times 10^6$.

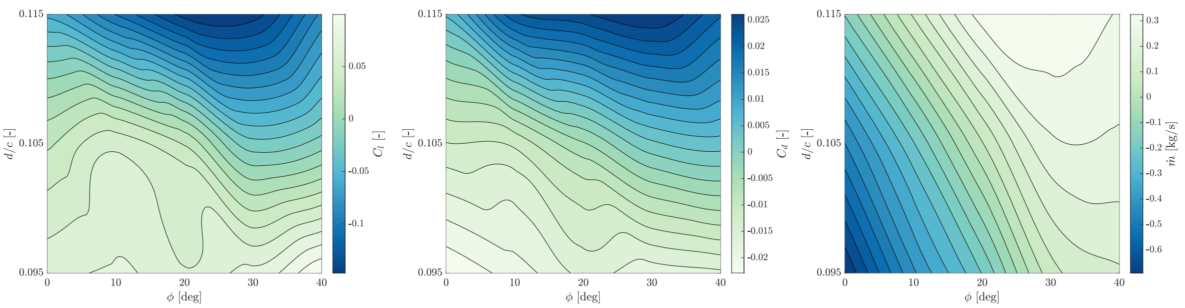

(a) Lift coefficient (b) Drag coefficient (c) Mass flow rate

Figure B.14: Interaction effects between duct gap and stagger angle on the deviation of lift coefficient (ΔC_l), drag coefficient (ΔC_d), and duct mass flow rate ($\Delta \dot{m}$) relative to the mean response value, at an angle of attack $\alpha = 10°$ and a chord Reynolds number $Re_c \approx 5 \times 10^6$.

B.5. ADDITIONAL 3D AERODYNAMIC RESULTS

NON-DIMENSIONAL TURBULENT KINETIC ENERGY

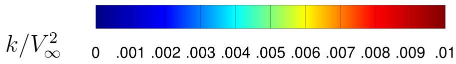

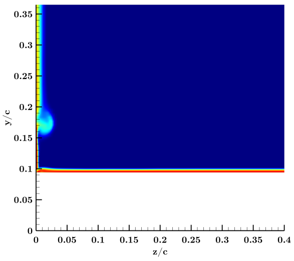

(a) Clean wing

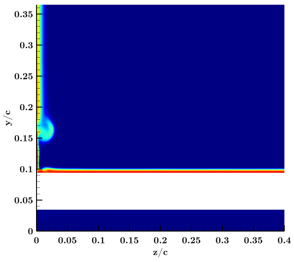

(b) HX porosity $\varepsilon = 0.88$

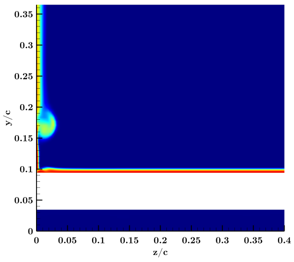

(c) HX porosity $\varepsilon = 0.81$

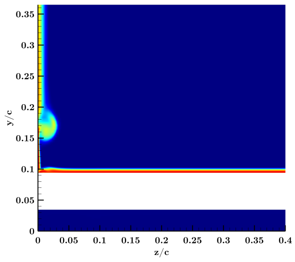

(d) HX porosity $\varepsilon = 0.72$

Figure B.15: Contours of non-dimensional TKE in the plane at $x/c = 0.5$, computed for $\alpha = 2°$.

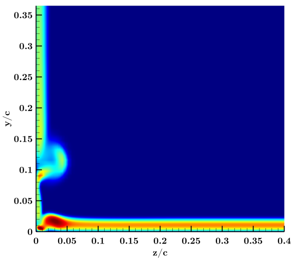

(a) Clean wing

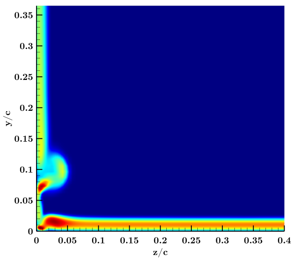

(b) HX porosity $\varepsilon = 0.88$

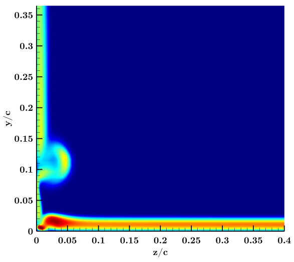

(c) HX porosity $\varepsilon = 0.81$

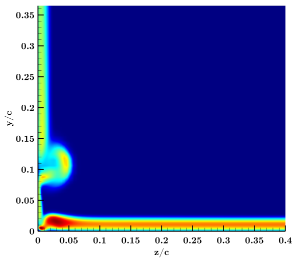

(d) HX porosity $\varepsilon = 0.72$

Figure B.16: Contours of non-dimensional TKE in the plane at $x/c = 1$, computed for $\alpha = 2°$.

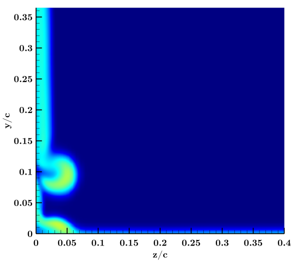

(a) Clean wing

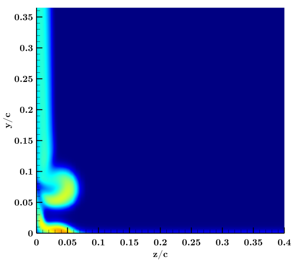

(b) HX porosity $\varepsilon = 0.88$

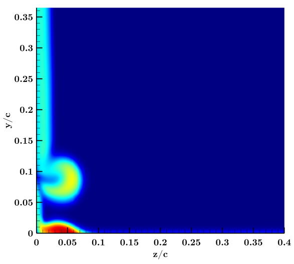

(c) HX porosity $\varepsilon = 0.81$

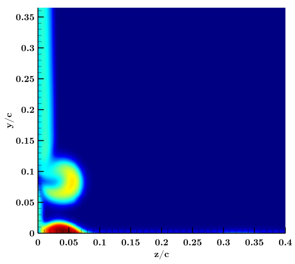

(d) HX porosity $\varepsilon = 0.72$

Figure B.17: Contours of non-dimensional TKE in the plane at $x/c = 1.5$, computed for $\alpha = 2°$.

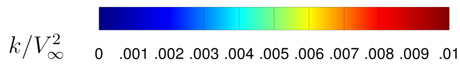

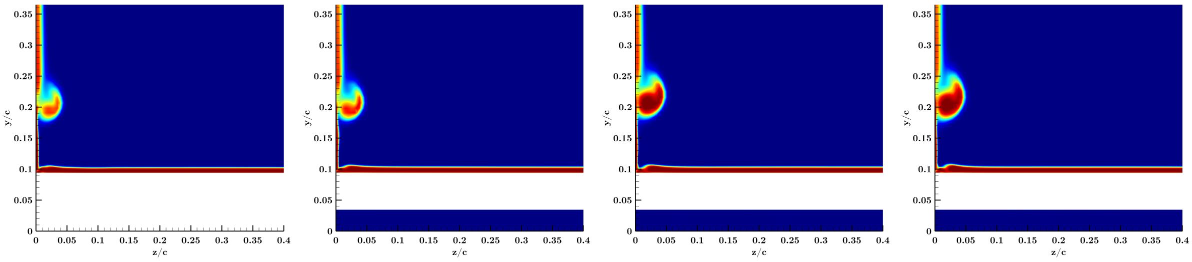

(a) Clean wing (b) HX porosity $\varepsilon = 0.88$ (c) HX porosity $\varepsilon = 0.81$ (d) HX porosity $\varepsilon = 0.72$

Figure B.18: Contours of non-dimensional TKE in the plane at $x/c = 0.5$, computed for $\alpha = 10°$.

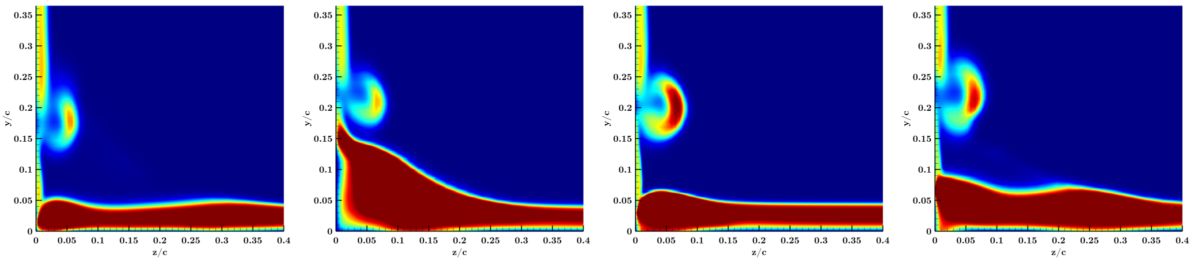

(a) Clean wing (b) HX porosity $\varepsilon = 0.88$ (c) HX porosity $\varepsilon = 0.81$ (d) HX porosity $\varepsilon = 0.72$

Figure B.19: Contours of non-dimensional TKE in the plane at $x/c = 1$, computed for $\alpha = 10°$.

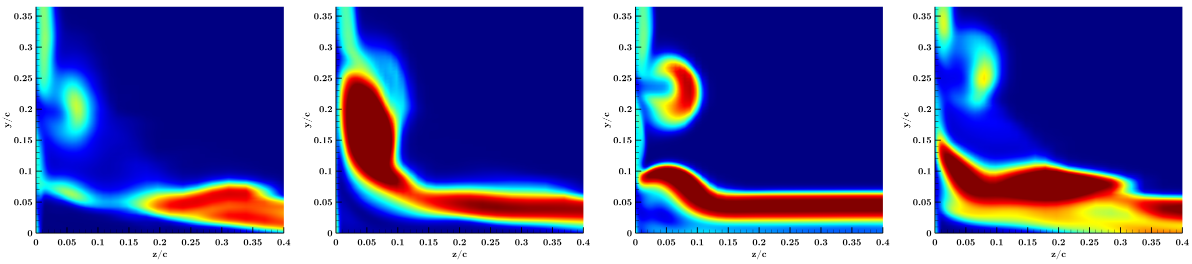

(a) Clean wing (b) HX porosity $\varepsilon = 0.88$ (c) HX porosity $\varepsilon = 0.81$ (d) HX porosity $\varepsilon = 0.72$

Figure B.20: Contours of non-dimensional TKE in the plane at $x/c = 1.5$, computed for $\alpha = 10°$.